

Dissertation
Submitted to the
Combined Faculties for the Natural Science and for Mathematics
of the Ruperto-Carola University of Heidelberg, Germany
for the degree of
Doctor of Natural Sciences

Diplom-Physiker:
Born in:

Maik Kurt Lang
Bad Dürkheim, Germany

Oral examination: 1st December, 2004

The Effect of Pressure on Ion Track Formation in Minerals

Referees:

Prof. Dr. R. Neumann
Prof. Dr. G.A. Wagner

Zusammenfassung

Energieriche Schwerionen erzeugen in vielen Dielektrika längs ihrer Trajektorien dünne zylindrische Schadenszonen. In diesen Ionenspuren mit Durchmessern von einigen Nanometern kann es zu massiven physikalischen und chemischen Materialveränderungen kommen. In irdischen Mineralien entstehen solche Spuren durch spontane Spaltung von ^{238}U -Kernen. Bisher wurden Bestrahlungsexperimente mit Schwerionen immer unter Vakuumbedingungen durchgeführt. Untersuchungen zur Ionenspurbildung in Festkörpern, die hohen Drücken ausgesetzt sind, sollen zu einer Klärung der Erzeugungsbedingungen für Spaltspuren im Erdmantel beitragen. Solche Experimente sind wichtig für die Datierung geologischer Proben mittels der Spaltspuren-Datierungsmethode. Des Weiteren ist die Frage von großem Interesse, ob energieriche Schwerionen durch ihren Energieeintrag bestimmte Phasenübergänge in unter sehr hohen Drücken stehenden Festkörpern auslösen können.

Diese Arbeit beschreibt die ersten Experimente bei GSI bezüglich Ionenspurbildung unter hohen Drücken bis 140 kbar , bei denen relativistische Schwerionen vom SIS-Schwerionensynchrotron durch die Diamantstempel einer Hochdruckzelle injiziert wurden. Es zeigte sich, dass hohe Drücke die Wechselwirkung zwischen Schwerionen und Festkörpern beträchtlich verändern können. Es wurden Effekte beobachtet wie Unterdrückung von Ionenspurbildung, vollständige Amorphisation, Rekristallisation und Bildung neuer Phasen.

Abstract

In many dielectrics, energetic heavy ions produce thin cylindrical damage zones along their trajectories. Massive physical and chemical changes can occur in these ion tracks with diameters of several nm . In terrestrial Minerals, such trails are generated by spontaneous fission of ^{238}U -nuclei. So far, irradiation experiments with heavy ions were always performed under vacuum conditions. Studies of ion-track formation in pressurized solids are expected to contribute to an improved understanding of the creation conditions for fission tracks in the Earth's crust. Such experiments will be important for dating of geological samples using the fission-track technique. In addition, it is a question of great interest whether the energy deposition of swift heavy ions in a solid, being exposed to extreme pressure, can induce specific phase transitions.

This work describes the first experiments on ion track formation under high pressures up to 140 kbar which were performed at GSI by injecting relativistic heavy ions, accelerated with the SIS heavy-ion synchrotron through the diamond anvils of a high-pressure cell. It turned out that high pressures can significantly affect the interaction between heavy ions and solids. The effects observed include the suppression of track formation, the complete amorphization, recrystallization, and the nucleation of new phases.

Contents

1	Introduction	1
2	Background and previous experimental findings	5
2.1	Radiation damage	5
2.2	High-pressure research	8
2.3	Mica	11
2.3.1	General remarks	11
2.3.2	Radiation damage in mica	13
2.3.3	Micas at high pressure and high temperature	16
2.4	Highly oriented pyrolytic graphite (HOPG)	17
2.4.1	General remarks	17
2.4.2	Radiation damage in graphite	20
2.4.3	Graphite at high pressure and high temperature	22
3	Experimental	29
3.1	Diamond anvil cell (DAC)	29
3.2	Irradiation facility	33
3.3	Preexperiments	38
3.3.1	Energy deposition of heavy ions in natural diamond	38
3.3.2	Phlogopite irradiations under ambient pressure	40
3.4	High-pressure irradiations	41
3.4.1	Phlogopite	41
3.4.2	Graphite	45
3.4.3	Apatite, zircon, rutile, and quartz	48
4	Results and discussion	53
4.1	Energy deposition of heavy ions in natural diamond	53
4.2	Irradiation of phlogopite	58
4.2.1	Ambient-pressure irradiations	58
4.2.2	High-pressure irradiations	61
4.3	Irradiation of graphite	74
4.4	Irradiation of apatite, zircon, rutile, and quartz	82
5	Conclusion and outlook	91

Chapter 1

Introduction

In 1953, Coes set – for the first time – quartz, the trigonal low-pressure polymorph of (SiO_2) , which is stable at ambient pressure and temperature conditions, under a pressure of 3 GPa (30 kbar) [Coe53]. This SiO_2 – polymorph, one of the most abundant rock-forming minerals in the Earth's crust, underwent a transformation to a denser, new crystalline phase that has been found years later in high-pressure solids, and nowadays is known as the mineral coesite. This key experiment after the pioneering high-pressure work of Bridgman showed that under high-pressure conditions, materials can change their structure and thus exhibit physical and chemical properties that are different from those at ambient conditions. High-pressure devices combined with heating became an important tool in particular for experimental approaches in geosciences, to simulate the behavior of minerals under extreme P-T conditions relevant for the deep Earth interior and that of terrestrial planets. However, there are still geophysical processes that can not be simulated by experiments up to now. One of them is the radioactive decay and its structural features occurring in many minerals in the Earth's interior. During the geological formation processes of various rock-forming minerals, radioactive nuclides such as ^{238}U , ^{235}U , and ^{232}Th are incorporated while crystallization proceeds. For example, in zircon these radioactive impurities can reach quantities as much as $10^4 \mu\text{g/g}$. During geological time intervals, the nuclides may decay either by spontaneous fission or by alpha emission. In such processes, energy of several MeV is released and transferred to the lattice of the solid phase. This takes place at all locations in the Earth's interior and hence over a wide temperature and pressure range (rough estimation: 3 km depth corresponds to an increase in T of 90°C and P of 0.1 GPa). The question of the influence of both parameters on the process of energy release through the radioactive decay is a matter of debate.

In many minerals, spontaneous fission of ^{238}U – nuclei leads to the creation of so-called fission tracks. These tracks are extensively used for dating of geological samples. For such studies, beside the number of tracks, also the track length (particularly the etchable track length) is a crucial parameter because it provides additional information on the thermal history of the host mineral. Theoretical models, ion-irradiation experiments, and neutron irradiations at ambient conditions are used to test the creation of fission tracks and to deduce the "reference length". To our knowledge, up to now track-formation processes have not been experimentally studied under pressure and temperature conditions that are relevant to the Earth crust. The question, to which extent both thermodynamic

parameters have an influence on the number of fission tracks and the etchable track length, is still open and controversially discussed. Any deviations would imply that all models for fission-track dating require major revision. To date, there are only a few investigations dealing with the effect of pressure on the formation of ion tracks in solids.

Recently, Wendt et al. tested the influence of pressure on annealing of fission tracks in apatite [WVC02]. With increasing pressure (up to 2 GPa), they observed a decrease of the critical track-fading temperature. In contrast, Tagami et al. found no influence of pressure (up to 0.1 GPa) on fission-track annealing in zircon [YTS03]. Soares et al. tested the influence of pressure on the annealing of surface disorder induced by ion implantation of various ions in graphite samples [SBL⁺01]. They found that the critical annealing temperature increases at a pressure of 7.7 GPa . A crucial point is that these experiments expose already existing fission or ion tracks to elevated temperature and pressure, and hence this does not necessarily reflect natural systems, where fission tracks are created in a high-pressure and high-temperature environment. In connection with this problem, Cruz simulated the effect of target pressure on the stopping process of swift heavy ions by applying the effective charge theory and a molecular confinement model [Cru04]. This theoretical approach predicted a significant reduction of energy-loss value and range especially for high ion energies and gigapascal pressures.

There are few more experimental studies dealing with the subjects of radiation damage and pressure in a more general sense. Trautmann et al. irradiated an amorphous iron boron alloy in a limited zone with a large number of ions inducing a compressive in-plane stress of about 2 GPa due to anisotropic growth of the solid [TKT00]. A second irradiation and subsequent etching of these tracks revealed etch pits with decreased diameter in the stressed preirradiated area. Milinchuk et al. tested the influence of pressure on different γ -irradiated plastic foils [MKK83, MKK86]. They found that high pressure (up to 2.7 GPa) can affect the rate and course of the radiolytic process (cross-linking, radicals). Jacobs investigated the effect of pressure on F-center absorption in several alkali halides [Jac54]. He irradiated the ionic crystals with X-rays and subsequently exposed them to pressure (up to 0.5 GPa). With in situ spectrometry he observed a shift of the absorption band maximum as a function of pressure. Kindlein et al. tested the effect of ion implantation on graphite samples used for diamond synthesis [JLBdJ00]. After irradiation, they set the graphite under high temperature and high pressure (5.3 GPa) and found for hydrogen implantations at $1 \times 10^{17}\text{ ions/cm}^2$ a higher yield for diamond production. It should be mentioned that also in these cases the radiation damage was first created under ambient conditions and was afterwards exposed to high pressure.

The aim of this thesis was to irradiate solids at high pressures in the GPa range with heavy ions and to test the formation of tracks or possible ion-induced phase transitions. To apply such a high hydrostatic pressure, we used a diamond anvil cell (DAC), in which a microscopic specimen is mounted between two single-crystal diamond anvils of thickness $2 - 3\text{ mm}$ each. The irradiations were performed at the heavy-ion synchrotron of GSI with ions of kinetic energies in the order of several tens of GeV . Such large

energies are necessary to pass first one of the anvil diamonds and then penetrate the specimen over a thickness of typically $100\mu m$. Selecting the most suitable kinetic energy and energy loss in the sample, the energy loss of the beam in the diamond has to be taken into account. We therefore tested in a preexperiment the energy deposition of kinetic ions in our diamond anvils.

In a first set of experiments, phlogopite samples (a mineral from the mica group) were irradiated under various pressures. These investigations were designed first to test the experimental setup, and second to analyze the track formation process in this mineral as a function of pressure. This mineral was selected because ion tracks can be easily detected after chemical etching. In a series of additional experiments, synthetic, highly oriented pyrolytic graphite (HOPG), natural quartz, rutile, and zircon crystals were irradiated at various pressures. In most of these experiments, the pressure was adjusted in such a way that the respective mineral was outside its thermodynamic stability field. These minerals were selected because of their different high pressure behavior such as the nature of their phase transitions. One irradiation experiment was conducted to test the possibility of heavy ion irradiation of samples exposed simultaneously to high pressure and high temperature. For this purpose, an apatite sample was placed in a heated diamond anvil cell and subsequently exposed to the ion beam. This mineral was chosen, because it is extensively used for fission-track dating. For most of the samples, reference irradiations at ambient conditions were performed.

Irradiated samples were investigated by means of scanning probe microscopy, Raman spectroscopy, and transmission electron microscopy. The phlogopite specimens were etched additionally. For some minerals, irradiation effects have been observed that are clearly related to the pressure applied during the ion bombardment. It seems that in some solids, high pressure can change the track-formation process significantly and phenomena have been observed that are not present at ambient irradiation experiments.

Chapter 2

Background and previous experimental findings

2.1 Radiation damage

Radiation effects in solids were observed for the first time by the coloration of rock salts such as NaCl and CaF₂ [Pea30, Prz56]. The radiation damage of ionising particles was for the first time detected by the chemical etching of uranium fission tracks in various minerals containing radioactive trace elements [WdH92]. Since then, numerous radiation effect studies on various solids have been performed using a broad range of different kinds of radiation such as gammas, X-rays, and UV-light, and also particle beams (electrons, protons, neutrons, ions, and ion-clusters). In this work, samples were irradiated with heavy ions of MeV to GeV energy, and therefore the focus in this chapter will be put on specific radiation damage processes caused by beams of this kind. Recent results in this field can be found in the Proceedings of the Fourth International Conference on Swift Heavy Ions in Matter; Catania 2002 (Nucl. Instr. and Meth. B 209, 2003).

Heavy ions form tracks in most dielectrics, and in some selected semiconductors and metals. Along an ion trajectory, the material undergoes physical and chemical changes within a cylindrical zone of typically several nanometers in diameter. These so-called latent ion tracks may consist of amorphous material [AMDHA⁺⁹⁴, TCM⁺⁹⁷], but also ion-induced crystalline-to-crystalline phase transitions have been observed [HCD⁺⁹⁷, GMCC⁺⁰¹, Ben03b, Ben03a]. The radiation damage is created by the transfer of the energy via Coulomb interactions to the target atoms. This energy deposition is a crucial factor for the damage creation process, and is characterized by the energy loss value dE/dx (also named stopping power) representing the portion of energy deposited per path unit in the solid (common unit: keV/nm). The initial kinetic energy (often expressed as energy per nucleon) determines the kind of Coulomb interaction between impinging particle and target atoms. For ion energies $\geq 1 \text{ MeV/u}$, the energy is predominantly transferred first to the target electrons (electronic energy loss $(dE/dx)_e$). For low-energy ions, elastic scattering at the target nuclei takes place (nuclear energy loss $(dE/dx)_n$). It should be mentioned that during the passage of an ion both mechanisms are present and, especially at intermediate energies (few hundred keV/u), both energy losses give a significant contribution. However, in the irradiation experiments of samples enclosed in a DAC, swift heavy ions were used that penetrated the sample completely and hence the amount of nuclear energy loss was negligible. Figure 2.1.1 displays the energy loss of an ion as a function of its kinetic energy. The two stopping power regimes

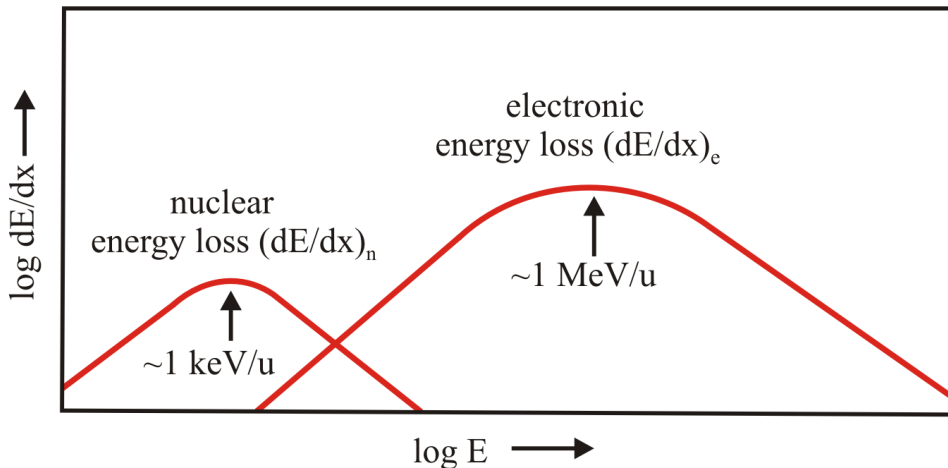


Figure 2.1.1: Qualitative plot of ion energy loss in matter as a function of kinetic energy. The maximum in the electronic energy-loss regime is named Bragg peak.

in this qualitative diagram are indicated by the two peaks.

The electronic energy-loss region that is important for us is located at higher kinetic energies ($E_{kin} \geq 1 \text{ MeV}$ per nucleon). The maximum of dE/dx (Bragg peak) depends on the ion mass and is located around 1-4 MeV/u. The functional evolution beyond this energy-loss maximum (at higher energies) is described by the Bethe-Bloch formula [Jac83]. At this point it should be mentioned that the energy-loss value for a given kinetic energy of an ion can be calculated for various targets by different stopping codes such as the "Stopping and Range of Ions in Matter" code (SRIM) from Ziegler et al. [ZB99a].

The radiation damage created by nuclear-energy-loss ions is understood in terms of knock-on processes and cascades, in which the kinetic energy of an ion is directly transferred to the nucleus of a target atom. These mechanisms have been investigated by numerous ion implantation experiments. The damage trail is characterized by interstitial atoms and vacancies in the target due to elastic collisions. For energetic ions, the situation is more complicated because the kinetic energy is first transferred to the electron subsystem of the target. This leads to multiple ionization processes along the ion path and results in primary electrons with rather high kinetic energies (depending on the ion energy). Through Coulomb interactions, these electrons can release secondary electrons. Part of this excitation energy is directly converted into lattice vibrations (heat) and luminescence. Only a fraction (typically a few %) of the deposited energy results in radiation damage. In contrast to conventional irradiation (UV-light, x-rays, electrons) the situation is more complex for heavy ions due to the very high excitation density (several orders of magnitude). For the interpretation of the extended defects within an ion track and the diversity of radiation damage in different solids, various theoretical considerations have been developed over the years.

In the so-called Coulomb-Explosion model, the damage creation process is described as a

2.1 Radiation damage

repulsion of positively charged target atoms close to the ion trajectory [FPW65b, LD93]. As mentioned above, the ions transfer their kinetic energy to the target electrons. The electron cascade results in a trail of positively charged target atoms. It is obvious that the positive target atoms attract the free electrons and only if the charge neutralization time exceeds about 10^{-14} s [SLXG01] the repulsion of the positive target atoms can take place, creating an ion track consisting of interstitial atoms, vacancies, and other defect features. Clear experimental evidence of the Coulomb-Explosion model is still missing, and it is unlikely that in solids having a high electron mobility (e.g. semi-metals) the charge neutralization time is high enough to allow the Coulomb-Explosion [SLXG01].

A different approach is realized by the so-called Thermal-Spike model [WDPT94, WVE00, TDWP96, TCD⁺96, DBPT99, TDMP00]. In this model, the energy of electronic excitation of the solid after the passage of an ion is transferred to the phonon system (lattice vibration) by electron-phonon interactions. So, the energy is transformed into heat, which results in a strong increase of the temperature in a short time interval close to the ion trajectory. This temperature peak can lead to a melting process, and the defect creation and amorphisation are explained by the rapid cooling of the molten phase. Within the Thermal-Spike model the track diameter is defined by the extension of the cylindrical zone, in which the temperature is high enough for melting. However, a major problem of this model is that equilibrium constants are used to describe non-equilibrium processes due to the short time scale. It is believed that the passage of an energetic ion leads to a local heating, but the amount of the temperature rise and especially the question whether melting occurs are not clarified up to now. Beside the Coulomb-Explosion and Thermal-Spike model, other theoretical considerations have been undertaken in order to understand the mechanisms of the damage creation process initiated by swift-heavy-ion irradiation (e.g. Exciton-Plasma model [IS01] and Lattice-Relaxation model [WT85, SB94, Sta96]). But up to now, the formation process is still not completely understood, and relevant processes are controversially discussed.

Our irradiation experiments were performed on materials that were exposed to a high hydrostatic pressure, in order to study the influence of this parameter on the ion-track formation and examine possible phase transitions. Therefore, it is worth noting that heavy-ion irradiation at ambient pressure can induce a mechanical stress in the solid [STN03]. In some amorphous materials, an enormous irreversible deformation of the solid was observed after ion irradiation [KS83, KHS86, KCL⁺89, HKS90, ABJ⁺93, BLRK92, SWCP95, GBC⁺96, TKT00]. A model was developed which describes the ion tracks as cylindrical thermoelastic inclusions, where the heating and the resulting melting leads to a shear stress relaxation [Tri95, TR95, Tri96, Tri98]. Also the possible existence of ion-induced shockwaves is discussed [TE01]. The authors explain their results in terms of a supersonic pressure wave, which is induced by the rapid heating of the ion-track core.

2.2 High-pressure research

Since the 20s of the last century, numerous high-pressure and high-temperature experiments have been performed to study the physical and chemical properties of various materials. A major aim was to simulate the extreme pressure and temperature conditions of the Earth's interior in order to understand a number of geological and geodynamic processes (e.g. phase transitions and their relevance to seismic-wave discontinuities) [Hem98]. Apart from geoscience, its application and the interest in planetary science [Hem98], also aspects from material's point of view in materials science [HA98] have become an important branch of high-pressure and high-temperature investigations, in particular aiming at innovative materials for technological applications [McM02]. New substances can be synthesized under high pressure in such a way that they exhibit special electric and magnetic properties or enhanced mechanical properties such as hardness. In many cases, they are recoverable to ambient pressure conditions through precisely tuned P-T paths, overcoming thermodynamic boundaries in combination of metastability and kinetical hindrance of re-transformation. For example, tenuous materials can be converted into dense metals (pressure-induced metalization of insulators) under high-pressure conditions [HA98], or new superconductors can be produced from pure elements [ESMH01, SKF⁺01]. High-pressure techniques can also be used in order to control reactions in organic chemistry and biogeochemistry [Hem00, Win02].

There are many review articles and textbooks giving an overview of the different high-pressure techniques and various sample analyzing methods. For the short summary of this chapter, three of them have been used [HH98, MDK00, HM02]. In principle, high pressure can be achieved by three different dynamic and static compression techniques. One is the group of the so-called "large-volume"mechanical presses, where rather large sample volumes can be pressurized (up to tens of cm in industrial synthesis processes). These presses came into use in the 50s of last century, and nowadays different apparatuses such as piston-cylinder and multi-anvil devices are available. In the former, a piston is pushing against a sample embedded in a cylindrical chamber [BE60, Bri63, Ere96, HI97], and pressures up to 6 GPa ($1 \text{ GPa} = 10 \text{ kbar} = 10^9 \text{ N/cm}^2$) can be reached. A significantly higher pressure can be achieved by multi-anvil devices [Ere96, HI97]. The pressure is generated by special anvils having two parallel end surfaces of different sizes. The smaller area is pressed onto the sample or sample chamber, whereas on the other end having a larger area, high loads are applied (up to 50 000 tons). The pressure is increased by this area ratio and nowadays, many different designs of such anvil devices are available (e.g. multi-anvil and opposed-anvil devices), and pressures up to 40-50 GPa can be achieved. The "large volume"apparatuses have the advantage that a larger amount of material can be either synthesized under high pressure, or investigated with analytical tools that rely on large samples, for example, ultrasonic interferometry [CLL96] and neutron scattering [KBB⁺97]. Furthermore, internal heaters can be placed in the sample chamber beside other probes, e.g., for measurements of the electrical conductivity. The disadvantage of this kind of compression technique is the general inaccessibility for optical or X-ray probes. It should be mentioned, however, that high-

energy synchrotron irradiation can now be used to reach samples in multi-anvil devices in sophisticated geometries [WWM98, NMH⁺92].

The second static compression technique is the so-called diamond anvil cell (DAC), which was used in the framework of this thesis. In 1959, this opposed-anvil method was developed by several groups [JLN59, WLVB59]. The principle as displayed in Figure 2.2.1 is the following: A small hole is drilled in a pre-indented metal gasket, which is usually a thin foil. Together with the two culet faces of the opposite diamonds, this hole represents the pressure chamber. In this chamber, the sample is inserted together with a pressure calibrant (e.g. ruby), and afterwards a pressure medium (generally a liquid) is added.

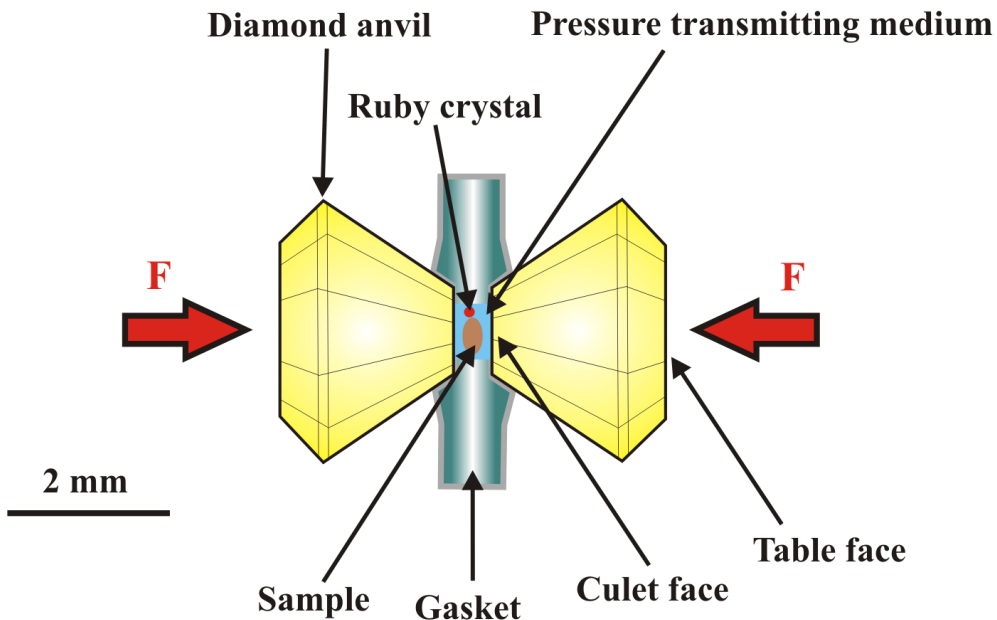


Figure 2.2.1: Scheme of a diamond anvil cell (not to scale). Sample and ruby crystal (pressure calibrant) are enclosed in a chamber filled with a pressure transmitting medium. By squeezing the two diamond anvils against each other, a hydrostatic pressure is created at the sample.

The two diamonds are squeezed together, for example by screws as the force generating mechanism. The force applied to the diamonds is used to pressurize the pressure medium, and as a consequence a hydrostatic pressure is applied to the sample. The diameter of the diamond anvil at the sample site is generally $< 1 \text{ mm}$, and hence at moderate forces very high pressure can be achieved. This culet-face diameter can range down to $50 \mu\text{m}$ for achieving pressures above 100 GPa. There are many review articles and textbooks explaining the pressure generation with this technique in great detail, e.g., [Jay83, HI97, HH98, MDK00, HM02]. By externally heating the diamond anvils with electrical resistance coils [BT65, Sun76, MMB87, BSBC93, FM94], the sample can reach a maximum temperature of about 1500 K. Modifications of the diamonds and mechanical improvements increased the accessible pressure regime over the decades

[MB75, MB76, MB78, VDBR88, MWC⁺90]. Nowadays, many different types of DAC are in use and pressures up to 300-500 GPa can be reached, which corresponds to the pressure at the center of the Earth (364 GPa). The diamond anvils are optically transparent, and therefore different kinds of optical spectroscopy (e.g. Raman spectroscopy) can be applied for *in situ* sample analysis [Sha77, She84, GSMH99, MGM⁺00]. Furthermore, focused lasers can be used to heat up the sample to several thousand K [MB74b, HSM91, Boe93, Boe96, HSBD98, SRWS00, BEM02]. In contrast to that, samples can be cooled to millikelvin temperatures while being held at pressures above 100 GPa [MCS93, GHMS98, HTP98, EGS⁺00]. The diamonds are also transparent to X-rays and synchrotron radiation and therefore allow *in-situ* characterization of the sample structure [Llo64, MB74a, KH77, FK78, Bas80, STF⁺92, NM94, MH96]. A new type of diamond anvils ("designer diamond anvils") can be grown by chemical vapor deposition, where electrodes and other objects can be embedded in the diamonds for electrical and magnetic measurements [WAAR⁺00, PVWJ01, VW02].

The third technique for high-pressure generation is that of dynamic compression. With compressed gas, pulsed lasers, high, pulsed electrical currents, and explosives, shock-waves can be generated due to a high-velocity impact [Nel02]. Pressures up to 50000 GPa can be achieved by a shock compression of the sample within ps. Because this compression is so fast, the process is adiabatic and the temperature increases up to hundred of thousands of degrees. So this technique can provide simultaneous high-P-T conditions, but not high-pressure conditions without heating. In contrast to a laser-heated DAC, the high-pressure and high-temperature conditions of the sample are kept only during a short time interval (μ s to ns, depending on the method of shockwave generation), which limits the *in situ* analytical methods due to limits in time resolution.

With different compression techniques and additional heating, pressure and temperature can be applied to a sample over a wide range. A major aim is to measure the material properties *in situ* at high-P-T conditions, or to study stable phases and other material modifications, which have been created under these conditions, after pressure release. Many different analytical techniques for the characterization of different sample properties are nowadays available for high-pressure science. Electronic states of a material under high-P-T conditions are detectable with optical spectroscopy (absorption, luminescence, and reflectivity) [Jac54]. Vibrational states can be probed with Raman spectroscopy in order to identify potential new phases or to characterize electronic and magnetic excitations under pressure [SGM⁺00]. IR spectroscopy makes it possible to analyze the crystal structure and electronic states of a sample and to detect possible transformations from insulator to semiconductor or metal. Brillouin spectroscopy is used to measure propagation velocities of acoustic waves in high-pressure samples by the scattering with light waves and subsequent Doppler shift measurements [BB63]. Furthermore, refractive indices and phase transitions can also be investigated with this method [BSM⁺81]. Travel time of acoustic waves in matter under high-pressure conditions and elastic moduli can be measured directly by interferometry [JKRB90, CLW98, LLW98, SCN⁺98]. X-rays allows one to investigate both the lattice and structural properties of crystalline samples under high pressure and high temperature. With this technique, crystalline-to-crystalline

[FJ97] and crystalline-to-amorphous [HJM⁺88] phase transitions can be recorded. Early studies have been performed with conventional X-ray sources [Llo64, BTS67]. But since the development of synchrotron facilities has made progresses, this method becomes an important tool for structural investigations [Bas80] due to advantages such as high intensities, tunable energies, and small spot sizes. X-ray studies can be conducted either on polycrystalline powder or on single crystals. Metal probes allow the measurement of electrical conductivity either with large-volume apparatuses [Bri58, BD61, KM71] or with DACs [BB77, MA77]. With similar probes, the magnetic behavior of a sample under high pressure is measurable and possible transitions to superconductivity are detectable [TSH⁺02]. There are several other techniques available to study the properties of a sample under high pressure, for example, nuclear magnetic resonance (NMR), Mössbauer spectroscopy, nuclear forward scattering, and neutron scattering. After pressure release and subsequent dismounting of the sample, additional investigations are assessable, such as etching and transmission electron microscopy (TEM).

2.3 Mica

2.3.1 General remarks

Mica belongs to the group of rock-forming minerals and represents about 4% of the Earth's crust. There are more than 30 individual mineral species belonging to this group which can be found in all rock types such as of igneous, metamorphic, and sedimentary origin. Mica are resistant and durable, and can withstand high temperatures and pressures in metamorphic regimes. Because of its physical properties, in particular excellent heat isolation and high resistivity against disruptive electrical discharge, mica is used for numerous technical applications. Another important characteristic is the high sensitivity to radiation damage, making it appropriate as nuclear track detector material.

As typical for a phyllosilicate, mica has a sheet-like structure with SiO_4 – tetrahedra as a main constituent. It consists of formally negatively charged layers, which contain one octahedral and two tetrahedral sheets (Figure 2.3.1). These layers are bonded by large positively charged interlayer cations such as potassium. This binding is rather weak and, therefore, the good cleavage of the mineral is provided by this interlayer side. For true micas, the negative charge of the 2:1 layer amounts to -1, for brittle micas to -2 due to different degrees of Al substitution on tetrahedral Si positions. The three basal oxygen anions (O_B) of the tetrahedral sheet are connected with the O_B of a neighboring tetrahedron and in this way form the basal oxygen plane (O_B – plane) consisting of a hexagonal pattern of six oxygen anions, as displayed in Figure 2.3.1. The apical oxygen anion O_A of the tetrahedron, which is situated perpendicular to the plane of O_B atoms, forms together with other O_A – anions and hydroxyl anions (OH^-) the apical oxygen plane (O_A – plane) which is sometimes also called the "hydroxyl plane" (see Figure 2.3.1). Two such adjacent planes constitute, together with the layer of

octahedral cations, the octahedral sheet. This structure is realized by the connection of two O_A^- anions with one OH^- of each O_A^- plane, resulting in an octahedron. In the case of trioctahedral micas (e.g. biotite, phlogopite), all octahedrons are occupied with cations such as Mg and Fe, whereas in the case of dioctahedral micas (e.g. muscovite) only 2/3 of the octahedrons are occupied by cations such as Al. Trioctahedral micas are also called dark micas, and dioctahedral micas are identified as white micas. A more detailed description of the structure of different micas can be found in chapters 1, 2, and 4 in "Micas" Reviews in Mineralogy Vol. 13 (S.W. Bailey, editor, 1984) as well as in chapters 1, 3, 4, and 12 in "Micas: Crystal Chemistry & Metamorphic Petrology" Reviews in Mineralogy & Geochemistry Vol. 46 (A. Mottana, F.P. Sassi, J.B. Thompson (JR), S. Guggenheim, editors, 2002).

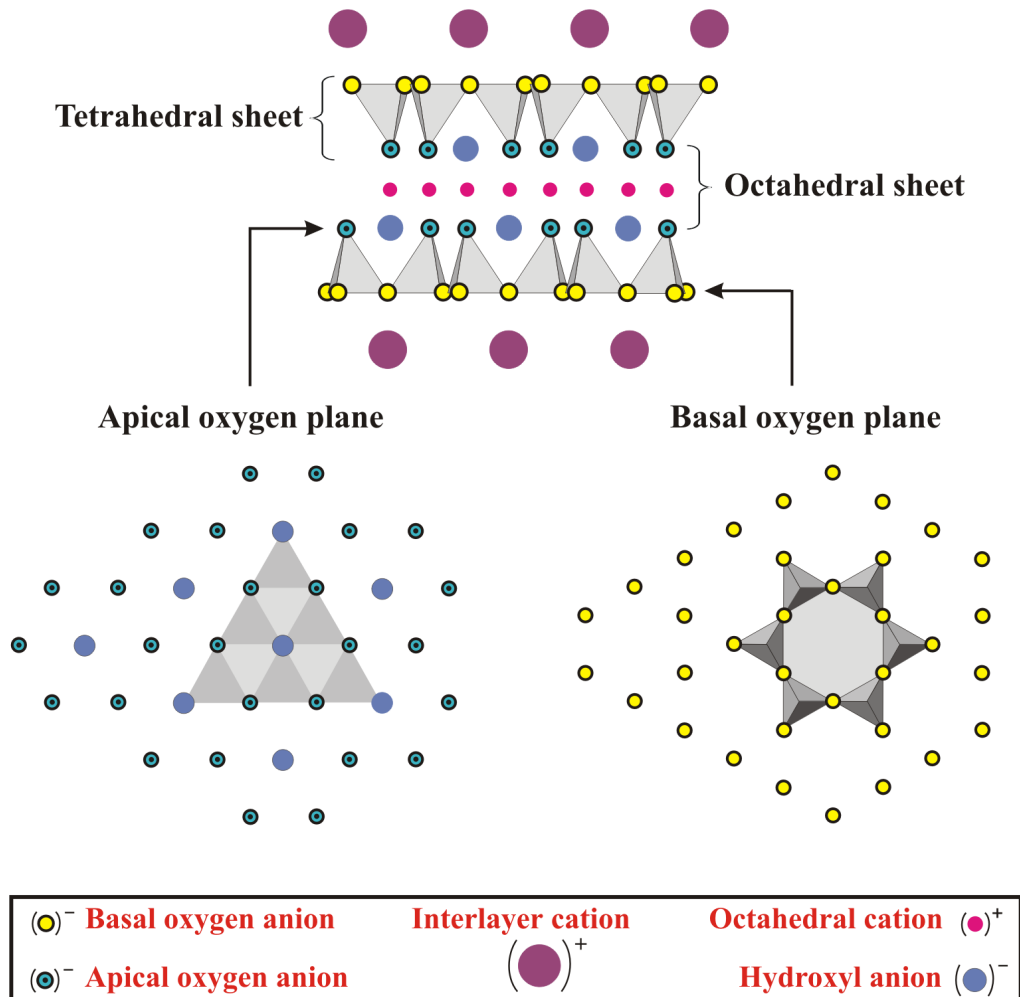


Figure 2.3.1: Schematic of the mica structure. Upper part: cross-section viewed along [110]. The negative charge of the 2:1 layer is compensated with a layer of positively charged interlayer cations. Lower part: apical oxygen plane and basal oxygen plane seen along [001].

In comparison to muscovite, phlogopite is a rarer member of the mica group. It has been mined, however, for its heat and electrical insulating properties, which are considered superior to other micas. Phlogopite in general is the iron poor and magnesium rich trioctahedral form $K(Mg, Fe^{2+})_3[(OH)_2AlSi_3O_{10}]$, whereas biotite represents a quite iron rich and magnesium poor member of trioctahedral mica: $K(Al, Fe^{3+})_2[(OH)_2AlSi_3O_{10}]$. The dark color of this mica can be explained by means of the d-d transition of Fe^{2+} , Fe^{3+} and $Fe^{2+} - Fe^{3+}$ charge transfer bands. Biotite tends to form in a wider range of conditions than phlogopite, which is limited mostly to ultramafic rocks and magnesium rich marbles and pegmatites. Notable occurrences of phlogopite exist in Ontario and Quebec (Canada), Kola Peninsula (Russia), and at many localities in Europe.

2.3.2 Radiation damage in mica

Due to its high sensitivity to radiation damage, mica has played an important role for decades in the research field of nuclear track detector materials. The starting point for these activities was the discovery of natural radiation damage in this mineral. Throughout the geological formation process of mica, radioactive nuclides, such as ^{238}U , ^{235}U , and ^{232}Th , can be incorporated in the crystal. During the alpha decay, e.g., the recoiling nucleus produces the so-called alpha-recoil track (ART). Spontaneous fission of a ^{238}U nuclide leads to tracks of the fission fragments as observed for the first time in 1959 by Silk et al. in muscovite mica using transmission electron microscopy [SB59]. The tracks appeared as long and cylindrical damage zones together with lattice distortions. After this discovery, possible track creation mechanisms were discussed and further transmission electron microscopy on radiation damage in mica was performed [BFA61, PW62]. The experimental determination of track dimensions was problematic due to the fading of the tracks caused by the electron beam of the microscope. So, later on, small-angle X-ray scattering (SAXS) and neutron scattering experiments were carried out. SAXS measurements are typically performed with scattering angles $< 1^\circ$ and the scattered X-rays carry information about the electron distribution (e.g. electron density) in the bulk material. With the help of this method the altered electron density in the track can be investigated and a mean radius can be extracted. It should be noted that this technique is model dependent and requires typically $10^{10} - 10^{11}$ ion tracks per cm^2 . So the deduced track properties are always of statistical nature. However, most investigations provided a typically track radius of a few nm [MLMH70, DM74, DMM76, DDLM81, AAS⁺85, ABS86, SAS89].

After the invention of scanning probe microscopy in the 1980s, this novel technique became a tool for direct investigations of single ion tracks. In 1991, the first tracks in muscovite created after heavy ion irradiation were identified by SFM on the sample surface as amorphous zones with circular cross section [TCBB91]. The mean diameter in the order of a few nm depends on the electronic stopping power of the ions, and there exists a threshold of about 5 keV/nm for the creation of one track per incident ion on the sample surface [TCBB91, TBS94]. SFM studies with a variety of imaging modes on individual ion tracks in muscovite mica were carried out,

and the size as a function of energy loss was measured using different ion species [BCPT93, HGA⁺94, DHH⁺95, DHE⁺95, DRH⁺96, AAN⁺96, NAA⁺96, AMNW98]. It turned out that small-angle scattering experiments with X-rays and neutrons revealed in general smaller diameters in comparison to SFM measurements, especially for higher electronic energy losses. However, it should be noted again, that diffraction experiments are sensitive to tracks in the bulk material, whereas SFM measurements are investigating generally only the track structure on the sample surface.

Wide-angle X-ray scattering experiments on powdered mica led to the conclusion that a track consists of an inner amorphous core and a surrounding zone, in which the lattice is disturbed but not destroyed [CDB⁺94, CDL96]. This might be the explanation for the discrepancies of diameters resulting from the two different techniques mentioned above.

More recently, high-resolution images of heavy-ion-irradiated muscovite were achieved by transmission electron microscopy [VSDN98]. The track cross section appears almost circular and increases with increasing energy loss. The absolute diameter values obtained by this work were in good agreement with earlier SFM measurements [AAN⁺96].

An ion track consists of disordered material with broken chemical bonds and hence exhibits a higher chemical reactivity. Consequently, this part of the crystal can be preferably etched with a proper solution, and muscovite mica has been extensively studied by track etching experiments focusing on both natural and artificial radiation damage [PW63, FPWH64, FPSM64, HW67, FPW65c, KK68, Kat69, HSS80, DDLM81, Kha86, SIC95]. The etching process converts the latent track into an enlarged etched track, and the study of the latter has provided valuable results in various fields, such as nuclear physics and geochronology. The threshold for the creation of an etchable damage was determined to 3.4 keV/nm, and thus the chemical etch threshold is at higher dE/dx values than damage creation. Also possible applications of etched tracks in muscovite, such as the use as microfilter, were the starting point of some experiments [SjBVD88]. It was found that etch pits after ion irradiation have a diamond-shaped form in this mica, which can be changed to some extent by using different etch solutions instead of HF [KKR81]. Most of the information mentioned above can be found in a review article of M. Toulemonde et al., where radiation effects in muscovite mica are summarized through 1994 [TBS94].

Phlogopite used in this work is in nature less abundant than muscovite, and hence the experimental work, in particular applying ion irradiation, is rather limited. However, tracks (natural as well as created by ion irradiation) in this kind of mica were investigated using SFM [vG00, Lan01, LGM⁺02b]. It was found that after ion irradiation small hillocks with diameters of a few tens of nm are created on the surface when the energy loss exceeds a critical threshold of about 20 keV/nm. In contrast to ion irradiated muscovite mica, the hillocks are pronounced features with heights of several nm. The radiation damage was also studied analogously to muscovite by means of track etching, partially with the aim of dating the mineral [PW63, HW67, GLK⁺03, GSMH99, GW00, LGM⁺02a, LGNW03]. As a crystalline material, phlogopite reveals an anisotropic etching behavior. This means

that the etch rate is direction dependent, and hence the etch pit geometry expresses in some way the crystal structure and atomic composition of the solid. It turned out that phlogopite exhibits a special attribute concerning this etch pit geometry. Two different types of hollows were found in both natural as well as artificial radiation damage, depending on the stopping power of the ion. In a set of experiments, it turned out that etch pits of fission tracks are hexagonal and those of ART are triangular [vG00, LGM^{+02a}] as illustrated in Figure 2.3.2. Fission fragments lose their energy in the solid via electronic energy-loss mechanisms, whereas ART nuclides slow down through nuclear collisions (see chapter 2.1). This leads to the conclusion that electronic energy loss leads to hexagonal etch pits, nuclear energy loss to triangular etch pits.

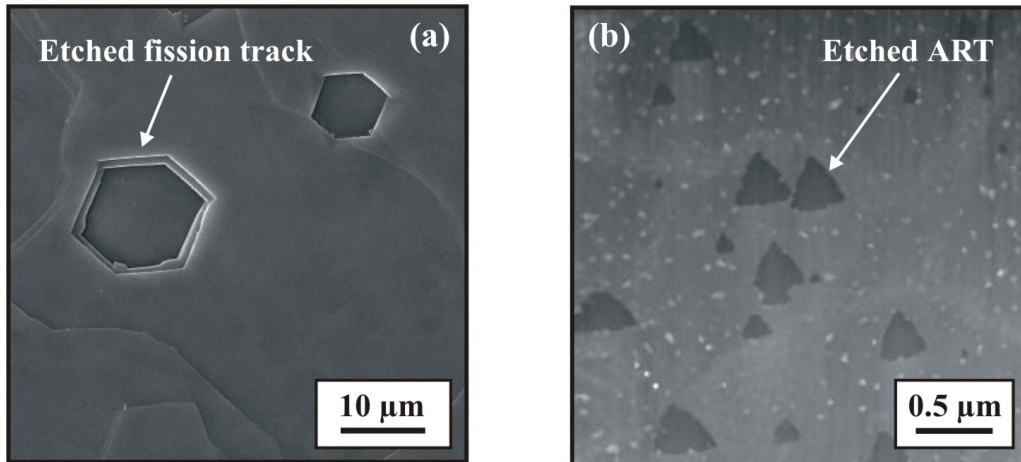


Figure 2.3.2: Natural radiation damage of a phlogopite specimen from the Kola peninsula (Russia) after etching with 4% HF. (a) SEM image of hexagonal etch pits of fission tracks after 3 hours of etching. (b) SFM image of triangular etch pits of ARTs after 10 min of etching.

Several other experiments using artificial ion irradiation for track creation showed a similar behavior after etching with HF. Hashemi-Nezhad [HN98] suggested that an energy loss dE/dx smaller than about 9 keV/nm leads to triangular etch pits. Other investigations found hexagonal etch pits for ions having $dE/dx > 8.8 \text{ keV/nm}$ and triangular ones for ions with $dE/dx < 5.7 \text{ keV/nm}$ [LGM^{+02a}]. This means, the pit geometry is triangular not only at nuclear but also at smaller electronic energy losses. However, at a certain stopping-power threshold there must be some significant change inside the latent track, and this can be concluded from the etch pit morphology. This feature, together with the almost perfect cleavage behavior providing a clean flat surface for SFM and SEM, the high sensitivity to radiation damage and the known etching conditions, found in previous investigations, makes phlogopite a very appropriate target material for irradiation experiments.

2.3.3 Micas at high pressure and high temperature

As mentioned earlier, the silicate group of mica is an important component of rocks in the crust and upper mantle of the Earth. Questions such as the stability and transformation of different rocks can only be answered if the high-temperature and high-pressure behavior of micas is understood. Consequently, this mineral was investigated in a set of experiments using different methods of high-pressure and high-temperature generation. Similar to irradiation experiments of different kinds of mica, the number of investigations on phlogopite is significantly smaller than that on muscovite mica due to the unequal occurrence of both minerals. However, the behavior of dioctahedral and trioctahedral micas in elevated T and P regions seems to be rather similar. Differences are related to the different fillings of octahedrons - in the case of dioctahedral mica, $1/3$ of octahedral sites are free - which leads to different response to high pressure and temperature. In the following, a brief overview of some experiments dealing with the behavior of phlogopite at high pressure and high temperature is presented. A more detailed description of the behavior of micas at high pressure and temperature is presented in a review article in chapter 2 of "Micas: Crystal Chemistry & Metamorphic Petrology" Reviews in Mineralogy & Geochemistry Vol. 46 (A. Mottana, F.P. Sassi, J.B. Thompson (JR), S. Guggenheim, editors, 2002).

First compression experiments on muscovite mica were performed in 1949 by Bridgman and coworkers [Br449]. Almost 30 years later, Hazen and Finger studied for the first time the behavior of trioctahedral mica under compression [HF78]. They recorded data from a natural phlogopite, enclosed in a diamond anvil cell. Using X-ray diffraction, they determined the unit-cell dimensions at four different pressures (up to 4.7 GPa). After a gap of about 20 years, high-pressure and high-temperature investigations were performed on synthetic Cs-annite and Rb-annite (similar to natural K- and Na-rich trioctahedral micas) [CZZ⁺99, CDM⁰¹]. In accordance with the experiments of Hazen and Finger, it turned out that trioctahedral mica, being a layered material, exhibits a large anisotropic axial compressibility in such a way, that the compression within the layers (a and b axes) is restricted by the strengths of the octahedral and tetrahedral sheets, whereas the weaker interlayer $M^+ - O$ bonds (M represents the cation such as K or Cs), provided by the large interlayer cations exhibit relatively large compressibilities. About seventy-five percent of the total volume decrease, caused by the applied pressure in this trioctahedral mica, is due to the compression of the interlayer volume in the c-axis direction. It was found that with increasing pressure the interlayer thickness undergoes a shortening at least ten times as large as that of the tetrahedral and octahedral one. This is also reflected by the findings that the interlayer site reveals a significantly smaller bulk modulus. The compression of the tetrahedral and octahedral sites is thus much smaller, and it seems that the latter have probably a greater compressibility. The tetrahedra of the tetrahedral sheet are almost rigid units, which try to compensate volume reductions mainly by rotation along bridging oxygen atoms. The behavior of phlogopite at high temperature is opposite to the behavior at high pressure. This is reflected by Hazen and Finger with their expression of an "inversion relationship" of micas seen in the structural changes

2.4 Highly oriented pyrolytic graphite (HOPG)

with temperature and pressure. Some heating experiments of trioctahedral micas can be found in [TM75, TCCL78, RG99, CZZ⁺99, TDN00]. Analogous to the dominant compression within an interlayer site under pressure, the thermal expansion is by far the greatest at this site, when heating up the mineral. The octahedra expand only to a minor extent during heating, whereas the tetrahedra mainly respond with rotation. So, cooling down a phlogopite from elevated temperatures is somehow similar to the compression at increasing pressures. If, at sufficiently high pressure or/and temperature, structural changes (e.g. variation of binding lengths or tetrahedron rotation) can no longer provide the energetically favorable linkage and minimize the misfit between different layers, then a transition to another phase in the mica will occur. The stability of phlogopite under upper-mantle conditions was investigated and discussed by several groups [KYA67, JK69, MB72, MB73, WE80, TTS86, ST90, Mit95]. Sato et al. observed and studied a phase transition of phlogopite at 4.5 GPa in a temperature regime of 1200-1500 °C [SKI97]. They report that above about 4.5 GPa phlogopite breaks down into pyrope (formula: $(\text{Mg}, \text{Fe})_3\text{Al}_2\text{Si}_3\text{O}_{12}$), Al_2O_3 – deficient phlogopite, and a fluid which they identified as water. The authors conclude that the fluid release could have influences on magmatic processes within the Earth's mantle.

Finally, it should be mentioned that the behavior of dioctahedral micas at high temperature and high pressure is similar, with the difference that they are thermally less stable, exhibit larger bulk thermal expansion, and have a slightly larger bulk modulus than trioctahedral micas. This behavior can be explained as mentioned earlier with an unequal filling of the octahedra cation sites. However, at about 18 GPa at room temperature muscovite begins to amorphize, a process which is completed at about 27 GPa.

2.4 Highly oriented pyrolytic graphite (HOPG)

2.4.1 General remarks

The element carbon is fundamental for all living organisms, has remarkable chemical and physical properties, and occurs in an immense diversity of compounds. It is widely distributed in nature and holds the sixth place in the list of abundance in the universe. Beside graphite and diamond, many other forms of carbon are known today, such as diamond-like, glassy, and amorphous carbon, nanotubes, fullerenes, and fibers. Carbon has six electrons, which leads to an electronic configuration $1s^22s^22p^2$, with four valence electrons distributed in the s- and p-orbitals. Different forms of carbon are realized by different hybridizations and subsequent bindings of these orbitals. In the following, the structures and properties of graphite and diamond are briefly summarized. Although both forms have opposite physical properties derived from a different crystal structure, the chemical behavior is very similar. In Table 2.4.1 the most important properties of both forms are displayed. Numerous articles and textbooks are dealing with different forms of carbon in detail, such as [DK92, MNB97] and references therein.

Graphite

This allotrope of carbon can be understood on the basis of sp^2 – hybrid orbital formation, where the σ – orbital mixes with two π – orbitals ($2s, 2p_a, 2p_b$) . Three of the four valence electrons occupy these orbitals (σ -bonds), whereas one electron remains in the p_c – orbital (π – bond) . One carbon atom is bonded with three nearest-neighbor carbon atoms within a plane (e.g. a,b-plane) via the σ – bonds , each separated by 120° from its neighbor. These three bonds are strong, due to the location of the charge density between two carbon atoms. The fourth electron in the p_c – orbital (perpendicular to the a,b-plane) provides the weak interplanar bonding. This π -bond is weaker, because the charge density lies between two planes, and the electron can not be attached to a carbon atom and is free to move. Graphite is a layered material and consists of planes of hexagonal carbon networks (honeycomb-like), with an in-plane nearest-neighbor distance of 1.41 \AA . The single planes are bonded by weak van-der-Waals forces having a distance of 3.35 \AA . Two adjacent planes are shifted parallel in such a way that every other layers of atoms superpose each other, expressed by the stacking sequence ABABAB... . Under deformation, a second layer stacking, the rhombohedral ABCABCABC... sequence can be created. The highly anisotropic structure of graphite is reflected by anisotropic properties. The mineral exhibits a metallic behavior in the a,b-plane, whereas along the c-axis the electrical conductivity is poor. So, the electron in the p_c – orbital is responsible that graphite is considered as a semimetal, having a band overlap of about 40 meV . Within the planes, graphite exhibits beside diamond the highest thermal conductivity. Concerning the Mohs' scale, graphite is one of the softest materials, and similar to micas it is easily cleavable, which can be explained by means of the weaker interlayer bonding, providing a flat surface. Due to this property, graphite substrates are especially suitable for SFM and STM measurements. There are numerous industrial applications for graphite, e.g., as electrode or writing material. Most of the natural graphite was produced through the slow metamorphism of organic material in rocks. Single crystals can be found at many locations, for example in Madagascar, Russia, and the United States. But they are only mm-sized and contain twinning planes, high defect concentrations, and a large amount of impurities. So, the production of synthetic single crystals is essential for industrial applications. Kish-graphite crystals for example are formed on the surface of iron melts with high carbon content. Another synthetic graphite, which is commonly used and was also the material of our choice, is the Highly Oriented Pyrolytic Graphite (HOPG), which is made by the pyrolysis of hydrocarbons at temperatures greater than 2000°C . The properties of HOPG such as electrical conductivity are close to those of natural single crystals, with the difference that crystals are much bigger and exhibit a very high degree of c-axis alignment.

Diamond

In contrast to graphite, an sp^3 – hybridization takes place in diamond, where the s-orbital mixes with all three p-orbitals ($2s, 2p_a, 2p_b, 2p_c$) . The four valence electrons occupy these orbitals, and each carbon atom possesses strong covalent bonds (σ -bonds), with four nearest-neighbor carbon atoms in a tetrahedral symmetry having a bond angle

Table 2.4.1: Some properties of graphite and diamond.

Properties	Graphite	Diamond
Band gap	-0.04 eV	5.47 eV
Electr. conductivity	Good conductor	Excellent insulator
Therm. conductivity	$30 \text{ W/cm} \cdot \text{K}^*$	$25 \text{ W/cm} \cdot \text{K}$
Melting point	4200 K	4500 K
Density	$2.2\text{-}2.3 \text{ g/cm}^3$	3.5 g/cm^3
Hardness (Mohs' scale)	1-2 (very soft)	10 (extremely hard)
Optical properties	opaque	transparent

* within the plane

of 109.47° and a distance of 1.54 \AA . The tetrahedra are linked together and build a regular, very stable lattice, which is responsible for the unique properties of diamond. Like in graphite, there exist two different stacking sequences. The ABABAB... order leads to so-called metastable hexagonal diamond, and the sequence ABCABCABC... leads to the well-known stable cubic diamond. In comparison to graphite, the atomic stacking is closer, and therefore the density is about 56% higher than in graphite. In the diamond lattice, impurities can be incorporated, which are the basis of a classification of natural diamond, due to changed optical absorption properties (type Ia, Ib, IIa, and IIb diamonds). Diamond is, from a scientific point of view, a very interesting material because of its exceptional and extreme properties. As well as being the hardest known material (see also 2.4.3), it is also the stiffest material, the best thermal conductor, and chemically inert to most acids and bases. Due to localization of the valence electrons between the carbon atoms and the lack of free charge carriers, diamond is an insulator with a band gap of 5.5 eV, making it transparent from the deep uv through the visible to the far infrared. Natural diamond is formed in the Earth mantle at depths of about 200 km at temperatures of $1500 - 2000 \text{ }^\circ\text{C}$ and pressures of about 6 GPa. The high temperature and pressure conditions prevailing there lead to a crystallization of carbon in a diamond structure [Ley01]. Once cubic diamond is formed, it is metastable also at lower pressures and temperatures (see also 2.4.3). Natural diamond is then transported within kimberlitic melt through pipes into the upper Earth crust close to the surface. So, diamond is mined from kimberlites in South Africa, Australia, Russia, Canada, and Brazil. Due to intense technical application based on the unique properties, synthetic diamond was needed. In the fifties of the 20th century, graphite was transformed into diamond for the first time in the labs of General Electric. To date, synthetic diamond is produced in large amounts (200 tons each year) using different methods. In large pressure cells, diamond can be synthesized under high-temperature and high-pressure conditions, which can be reduced to a certain extent when metal catalyst particles such as iron, nickel, and cobalt are present. Another method is based on chemical vapor deposition, where diamond can be directly created without graphite from a plasma containing for example methane and hydrogen [Ley01]. These CVD diamond films, grown e.g. on silicon substrates, are used as cutting tools, heat dissipation units, and

other devices. Even though synthetic diamonds can be produced in sufficient amounts, the different techniques are complicated and expensive, and not well understood in detail. In conclusion, natural diamond plays still an important role in science and industry, and each year about 110 tons are mined all over the world. Finally, it should be mentioned that the value of diamond crystals can be characterized by the 4 C's: Clarity, color, carat, and cut. One carat corresponds to 0.2 g.

2.4.2 Radiation damage in graphite

As a semimetal with free charge carriers within the sheets, graphite should react to energetic ion irradiation in a different way than the insulator phlogopite. Schiwietz et al. investigated the radiation damage process in various materials by electron spectroscopy [SLXG01]. They detected Auger electrons, which are released around the ion trajectory promptly after the passage of an ion. These electrons are probes for the early stages of the track formation process and in the case of graphite, they indicate that the lifetime of the highly ionized atoms in the track region is very short ($\approx 10^{-16}$ s). The charge-neutralization time is therefore significantly shorter than that required for Coulomb explosion (see chapter 2.1), which is about 10^{-14} s. Schiwietz et al. found high electron temperatures inside the ion track of up to 80 000 K for high electronic energy losses. They propose that radiation damage in graphite in the electronic energy-loss regime is created by the transfer of this energy to the lattice either by electron-phonon coupling (thermal spike model) [Des23, KLT57, RC82, WDPT94, Sze96, VB96] or via modified inter-atomic forces (lattice-relaxation model) [WT85, SB94, Sta96]. However, many groups investigated the radiation damage created in HOPG after ion irradiation. Most irradiations were conducted in the eV to keV energy regime, where the stopping process of the ions is dominated by elastic collisions with the target atoms. The motivation for ion irradiation studies in graphite arises from the use of this material in nuclear reactors. Most investigations on ion irradiated graphite were performed by means of STM measurements. In the following, a short overview of different radiation-damage experiments of graphite will be presented. First, low-energy experiments will be considered and, at the end, irradiations with energetic heavy ions are presented, which are comparable to our experiments.

Auger-electron spectroscopy on HOPG irradiated with Ar ions indicated that the threshold for Ar ion penetration into the graphite surface is between 42 and 44 eV [MBLR93]. This value was confirmed by classical trajectory simulations of Choi et al. [CKK93]. Marton et al. reported on dome-like features on HOPG-surfaces found with STM after irradiation with 50 eV Ar ions [MBB⁺95]. Auger spectroscopy indicated that the Ar ions are implanted between the topmost 1-2 layers and, as interstitials, induce a lattice strain, responsible for the defects. The authors report a displacement energy of the carbon atoms in graphite of 34.5 eV. Hahn et al. conducted Ar and Kr irradiations of energies 40 - 100 eV and found small hillocks with STM and UHV-STM [HK96, HK99]. They concluded that the surface defects are created from both carbon vacancies and rare gas interstitials in the graphite lattice. Many groups investigated

the radiation damage in graphite with various ion species in the keV energy regime [PPdV⁺89, CCAB90, PdVP91, CCC⁺92, RBGL95, BRGL96, MSF⁺96, HBL98]. Almost all investigations were performed with STM, and the defects on the surface exposed to the ion beam were identified as small hillocks with typical lateral dimensions of a few nm and heights in the Å-regime [CCAB90, PdVP91, CCC⁺92, RBGL95, BRGL96, HBL98]. The number of hillocks was found to be equal to the number of ions. Only Reimann et al. and Bolse et al. reported that at grazing incidence irregular chains were observed with a higher number of hillocks than ions [RBGL95, BRGL96]. Most of the authors explained the hillock formation process as a result of a volume expansion due to formation of carbon interstitials and interstitial agglomerations [RBGL95, BRGL96, HBL98]. Such expansions along the c-axis have been found also in earlier neutron-irradiation experiments [MIO75]. In some cases, also craters were found after ion irradiation [PPdV⁺89, MSF⁺96], and it was suggested that interstitials and vacancies can create such features. Seki et al. performed an Ar cluster irradiation (150 keV) of HOPG and found donut-shaped craters on the surface after imaging with STM [SKT⁺97]. Several groups conducted Raman studies on ion-implanted graphite which are summarized in [EDD⁺81]. A major observation was the occurrence of the disorder-induced $1360\text{-}cm^{-1}$ Raman line, which exhibits a rapid increase in linewidth as a function of fluence and ion species [ESD⁺82]. Before reporting on irradiation experiments using ions of pure electronic energy loss, it should be mentioned that there are several textbooks and review articles dealing with ion implantation in the low-energy regime [Sim65, DK92, LKM⁺94].

Kemmer et al. investigated HOPG samples after irradiation by means of STM [KGN⁺92]. After the irradiation with 3 GeV Au ions, the authors found little hills on the surface having a diameter of 1 to 2.5 nm and heights up to 0.5 nm. Two years later, Bouffard et al. studied HOPG irradiated with U ions of about 670 MeV [BCPT93]. The irradiated surfaces were inspected with STM and SFM. Both techniques revealed hillocks on the irradiated surface, indicating that they are of topographic nature. The small hillocks were widely dispersed in diameter (from 0 to 2.5 nm) and in height (up to 1.5 nm), which was explained by a discontinuous track structure although each ion created a hillock. Yan et al. found beside the hillocks small bumps, as they called them, on the graphite surface after irradiation with Au ions of energies up to 4.5 MeV [YLB⁺94]. They explained these findings as sputtered particles, released from the ion track after ion bombardment and subsequent return to the surface. A 215 MeV Ne irradiation of graphite was performed by Biro et al., and they found three different features on the surface by STM [BGH95]. They explain the radiation damage in terms of knocked-on C-atoms. Singh et al. irradiated a HOPG sample with 200 MeV Au ions and investigated the irradiated surface with an UHV-STM [STK00]. They detected an increase of metallicity in the graphite sample after irradiation. More recently, a detailed radiation damage study on HOPG irradiated by different species of swift heavy ions was performed by Liu et al. [LNTM01]. The defects created by the energetic ions (100 MeV to 2.6 GeV) were inspected with STM on the surface exposed to the ion beam as well as in the bulk after cleavage. Tiny tracks were observed with average heights between 0.3 and 0.9 nm and mean diameters between 2 and 3.5 nm almost independently of the energy loss and the ion species. These

hillocks were observed on two adjacent lattice planes, indicating that ion tracks induce an interplanar stress in the bulk, which is released after cleavage. Liu et al. emphasize that the track dimensions are significantly smaller than in many other materials, which could be explained by means of recrystallization processes. This interpretation is supported by the fact that the probability of track formation is significantly reduced in deeper bulk layers, where recrystallization processes should be more efficient than on the original surface due to breaking of bond symmetry and sputter processes. The authors found that tracks are created on the original surface, when the electronic energy loss value exceeds 7.3 keV/nm. Only for energy losses above 18 keV/nm the density of observed tracks was equal to the ion fluence. Liu et al. conclude that an ion track in graphite consists of a discontinuous sequence of perturbed zones. Beside the numerous STM investigations, only a few HRTEM experiments were performed on HOPG irradiated with swift heavy ions [CFG⁺94, DJC98]. In contrast to the small hillocks found on STM images, no radiation damage could be found with this technique. To summarize this chapter, the damage creation process is not yet fully understood, especially for swift heavy ions in the electronic energy-loss regime. However, tracks can be identified particularly by STM as disordered areas of a few nm in size. Radiation damage created in the nuclear energy loss regime can be understood in terms of interstitials and vacancies in the graphite lattice induced by knock-on processes of the projectiles.

2.4.3 Graphite at high pressure and high temperature

The phase diagram of carbon has been the subject of experimental work for many years, and the behavior of graphite was studied in great detail over a wide temperature and pressure range using static as well as dynamic high-pressure techniques. Much efforts was dedicated to investigations of the graphite-diamond transformation in order to understand the thermodynamical process underlying this phase transition and make use of it for diamond production. So, phase boundaries could be established, and new phases and forms of carbon could be found [BBW⁺96]. However, the behavior of graphite under high temperature and pressure is not yet fully understood. Beside high-pressure experiments, diamond was also created through the irradiation of graphite with various particles at ambient conditions. It is obvious that also heavy-ion irradiation under high pressure could transform graphite into diamond. Therefore, in the following, the phase diagram of carbon is shortly presented with focus on the graphite-diamond transformation. The content of this brief overview is taken mainly from a review article of Bundy et al. [BBW⁺96], but also some more recent findings are added. The chapter will be closed by describing some experiments where a graphite-diamond phase transition was observed after particle irradiations under ambient conditions.

The binding energy difference of graphite and diamond is only 3000 J/mol, which corresponds to about 30 meV/atom [BYM89, BVEG90, Ley01]. This is comparable to the thermal energy of atoms at room temperature, and hence this small gap should be easily overcome, and a transformation of graphite into diamond and vice versa should be easy. But obviously, diamond is metastable at ambient conditions (however, in principle dia-

mond transforms extremely slowly back to graphite) and can only at high temperatures be converted into the stable graphite phase. On the other hand, very high temperature and pressure are needed for the transformation of graphite into diamond. The reason for that is a very high activation barrier of about 7 eV, which separates both phases. Figure 2.4.1 (according to [ZZC94]) shows an energy diagram of metastable graphite at temperature and pressure conditions, where the transformation into diamond should take place, because the Gibbs free energy of the diamond phase is smaller and hence should be preferable, but to trigger this transformation, first the activation energy has to be overcome.

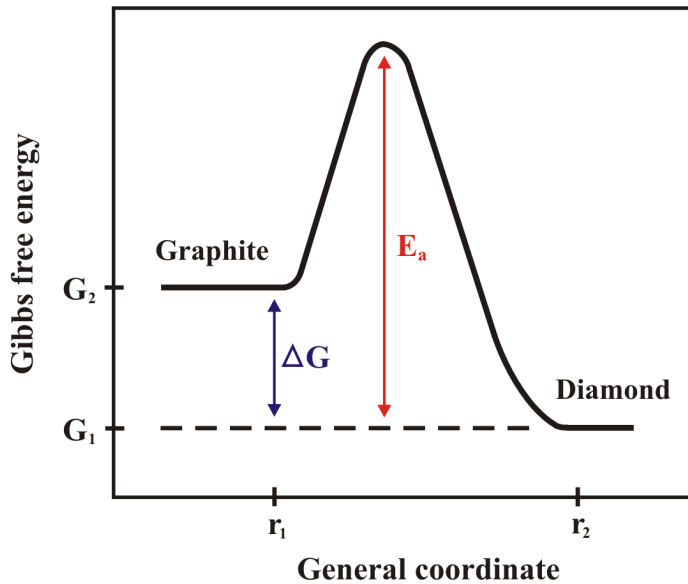


Figure 2.4.1: Energetic situation for the transformation of graphite to diamond after [ZZC94]. Even though diamond would be the stable phase at elevated temperature and pressure, graphite remains as metastable graphite until the activation barrier of 7 eV is overcome.

So, graphite can exist as metastable phase far into the stability field of diamond. Figure 2.4.2 displays the phase diagram of carbon, taken from [BBW⁺96]. Three main regions are separated by solid lines, representing the equilibrium phase boundaries (the phase diagram does not consider any of the fullerene carbon structures). The three phases of graphite, diamond, and liquid carbon meet at the triple point at about 5000 K and 12 GPa. The phase boundary of graphite and diamond which is the important one for our experiments, runs from 1.7 GPa at 0 K to this triple point. At room temperature, the corresponding pressure values lie at about 2 GPa. The position of this curve has been established by thermodynamic calculations and many different experiments such as testing the growth or graphitization of diamond [BBSW61, KK76, Bun63b, Bun63a, SFY90]. Another important line (dashed line) is shown in Figure 2.4.2 within the diamond stability field. This line starts from the triple point and runs with increasing pressure to smaller temperatures. At about 2000 K and between 15 and 20 GPa, an abrupt change in slope takes place so that afterwards this line goes more or less parallel to the y-

axis. Bundy et al. explain this line as a possible activation energy threshold for the fast transformation of compressed graphite, or hexagonal diamond into the thermodynamically stable cubic diamond. That means if pressure and temperature conditions are within this region, and hence the activation energy threshold is overcome, a complete solid-solid transformation into cubic diamond should take place on a very short time scale (e.g. $\mu\text{s-ms}$). The authors report some unpublished experiments of Bassett and Weathers that confirm this threshold line together with earlier investigations [Bun63a], and some theoretical calculations [ZZC94]. Additionally to the phase boundary lines and the graphite-diamond direct conversion line, also some important regions are marked in the phase diagram.

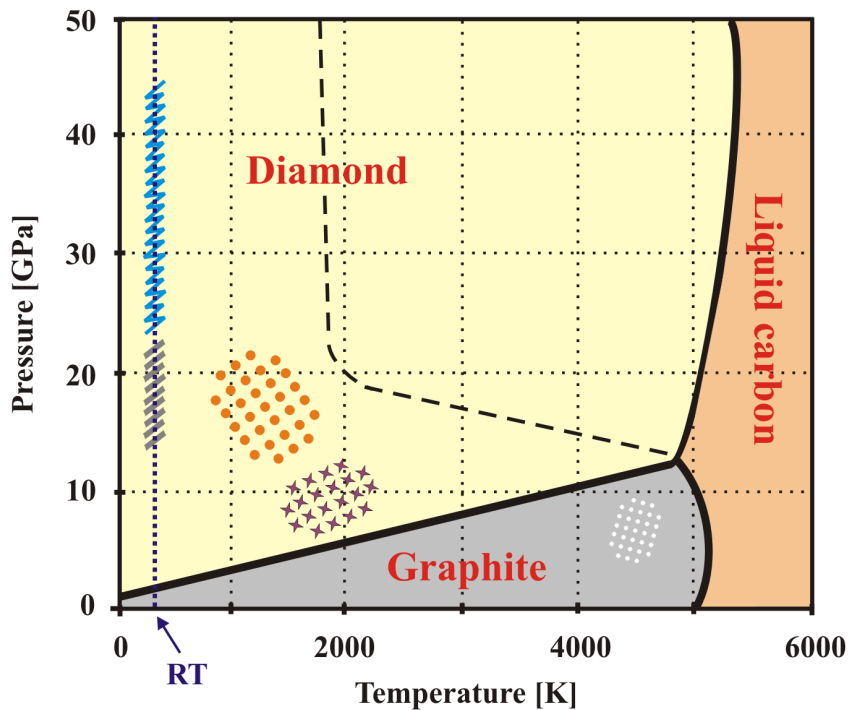


Figure 2.4.2: Pressure and temperature phase diagram of carbon after [BBW⁺96]. The solid lines represent equilibrium phase boundaries. The dashed line symbolizes a border, at which stable cubic diamond can be achieved (high-temperature side). The region within the stability field of graphite, marked with small circles, represents the P-T conditions, where diamond can be transformed completely into graphite. The area identified with stars represents the area for commercial diamond synthesis, whereas in the region marked with large circles hexagonal, graphite can be transformed into hexagonal diamond. Along the room temperature line, two sections are displayed, where graphite loses some of its properties, e.g. conductivity. For further comments see the text.

The area located around 8 GPa and 1800 K (stars) represents the region of commercial synthesis of diamond from graphite, when a catalyst such as metal iron, nickel or cobalt is

2.4 Highly oriented pyrolytic graphite (HOPG)

present. The region between 800 and 2000 K at pressures higher than 12 GPa (larger circles) was considered by Bundy et al. as the area in the phase diagram, in which graphite can be transformed into hexagonal diamond. The high temperature is necessary to shift the altering sp^2 -bonded honeycomb-like sheets in order to create hexagonal diamond [YUY⁹², Sun00]. The region, where a complete transformation of diamond to graphite takes place, lies within the stability field of graphite around 4500 K and 5-10 GPa (small circles). There are two further interesting sections in the phase diagram, along the room temperature line. When quenching graphite in a diamond anvil cell at ambient temperature to pressures greater than about 14 GPa (stripes), graphite loses some of its properties, such as reflectivity and conductivity [AD63, BK67, GMS89, HS89], and there are also changes in the X-ray diffraction pattern [ZS89, YUY⁹²]. Mao et al. performed synchrotron X-ray inelastic scattering of "cold-compressed"graphite (up to 23 GPa) and found that half of the π -bonds convert to σ -bond, whereas the other half remain as π -bonds in the high-pressure form [MME⁰³]. This is in accordance with the drop of conductivity, because more and more conducting electrons are removed. The authors propose a new distinct phase of carbon that seems to be what they call "superhard", because after pressure release they found indentation in the cubic diamond anvils. However, after pressure release graphite was again retrieved at room temperature. At pressures greater than 23 GPa (zigzag line), the graphite sample loses its typical Raman spectrum, which is replaced by a spectrum similar to that of amorphous carbon [GMS89]. When a graphite sample quenched at room temperature is heated to almost 2000 K, a fast and complete transition to stable cubic diamond takes place. Heating the sample only to about 1200 rather 2000 K leads to the creation of hexagonal diamond, which can be quenched to ambient conditions. In contrast to that, when the pressure on such a sample is released to ambient pressure without heating, the original graphite sample is retrieved [BK67, UY91, MME⁰³]. Beside this high-pressure and high-temperature experiments mentioned above, high pressure phases of carbon were also found in shocked rocks from several terrestrial impact craters [KAR97, DEB⁹⁶, LSM98]. More recently, a possibly novel cubic, transparent, and "superhard"polymorph of carbon found in the Ries crater (Germany) was reported [GDG⁰³]. To conclude with the description of the phase diagram of carbon, it should be mentioned, that the low-pressure region of graphite was not subject of this small compilation. Therefore, this part - including another triple point at about 0.2 GPa and 5000 K (graphite, liquid carbon, and vapor phase) - is not displayed in Figure 2.4.2. The existence of distinct other high-pressure and high-temperature phases of graphite, beside the stable cubic diamond, such as hexagonal diamond or other, so-called "superhard"phases is still under controversial discussion. For example, a "superhard"polymorph of carbon could be also explained by means of an imperfect cubic diamond, where lattice distortions could lead to an enhancement of the hardness, as observed for other materials.

The idea that a particle irradiation could transform graphite into diamond came from the discovery of submicron-sized diamond aggregates in uranium-rich Precambrian carbonaceous deposits. Since they were never exposed to high-temperature and pressure conditions, it was suggested that the radioactive decay might be responsible for the di-

amond creation [DO71, DLRK99]. In order to test these assumptions by simulating the radioactive decay, Daulton et al. irradiated sheets of fine-grain polycrystalline graphite at room temperature and ambient pressure conditions with 350 MeV Kr ions $6 \times 10^{12} \text{ cm}^{-2}$ of an energy loss 9 keV/nm, [DKLR01]. The irradiated sample and an unirradiated reference graphite sample was dissolved using a proper acid mixture. The residues were investigated with electron transmission microscopy. High-resolution lattice images and electron diffraction patterns led to the conclusion that irradiation created nanocrystals of cubic diamond (mean diameter 7.5 nm) with a yield of $\approx 0.01 \text{ crystals/ion}$. The absence of external pressure and heating of the sample together with a possible diamond creation time of picoseconds brought the authors to the suggestion that the small difference in energy between graphite and diamond coupled with surface properties could be the reason for the diamond creation via ion irradiation. Earlier in two other irradiation experiments, an irradiation-induced transformation of graphite to diamond was observed.

Banhart and coworkers created diamonds through an electron irradiation of graphitic onions ("bucky onions") [BA96, Ban97]. Online electron irradiation of small graphitic particles inside an electron microscope at temperatures higher than 600 K leads to the creation of perfectly spherical onions with almost undistorted shells [Uga92, CRD95, ZBS96]. Further irradiations of these onions under higher temperatures such as 900 K leads to the creation of vacancies in the onion shells. As a result of a new ordering, they shrink accompanied by a decrease in distance between the shells from the graphite value of 3.35 Å at the surface down to 2.20 Å in the core [BFRA97, RBLA98]. This shrinking leads to cross-linking and to the creation of sp^3 -bonds, and furthermore a very high pressure is formed in the core of the shells (up to 100 GPa). Further irradiations with electrons of a minimum energy 200 keV on a timescale of hours (flux: $\approx 10^6 \text{ A/m}^2$) leads to the formation of cubic diamond in the core, and the growth continues until the whole onion is converted into diamond. In the outer part of the bucky onions, the pressure is decreased to ambient values, so the authors pointed out that the growth of diamond under ambient pressure is unique. They give a possible explanation in terms of self-organization in dissipative systems and expressed the importance of vacancy creation in the graphitic structure [ZB97, ZLB00].

Wesolowski et al. [WLB⁺97] used Ne ions of an energy 3 MeV ($4 \times 10^{19} \text{ cm}^{-2}$) at temperatures between 1000 and 1400 K to convert graphitic carbon soot into nanometer-sized diamonds via an intermediate step of graphitic onions. Heera et al. created small diamond grains by the implantation of 60 keV carbon ions into SiC at 900 K (dose: 10^{18} cm^{-2}) and subsequent irradiation at 1200 K [HSPD00]. Orwa et al. implanted 1 MeV carbon ions (dose: $5 \times 10^{17} \text{ cm}^{-2}$) into fused silica at room temperature [OPJ⁺01]. Subsequent annealing in a forming gas mixture, e.g. H and Ar, at 1100 and 1400 K led to the creation of cubic diamond nanocrystals with sizes from 5 to 40 nm. Kindlein et al. implanted various ions on graphite samples and set them afterwards under 1240 °C and 5.4 GPa together with a catalyst [JLBdJ00]. They found that for hydrogen implantations at $1 \times 10^{17} \text{ ions/cm}^2$ the yield for diamond synthesis is up to 46% higher. More recently, a possible formation of nanodiamonds after irradiation of HOPG with highly

2.4 Highly oriented pyrolytic graphite (HOPG)

charged ions and subsequent treatment with electron or laser radiation was observed [KMH⁺03, MHK⁺03]. It should be mentioned, that the opposite way, the transformation from diamond into graphite is also possible under ion implantation [DK92, GKDK03].

Chapter 3

Experimental

3.1 Diamond anvil cell (DAC)

Within the framework of this thesis, two different DAC types have been used. Three DACs were modifications of Merrill-Bassett-type cells [MB74a], and two were hydrothermal DACs of type Bassett et al. [BSB93] as displayed in Figure 3.1.1. All of them were prepared in the Institute of Mineralogy of the University of Tübingen.

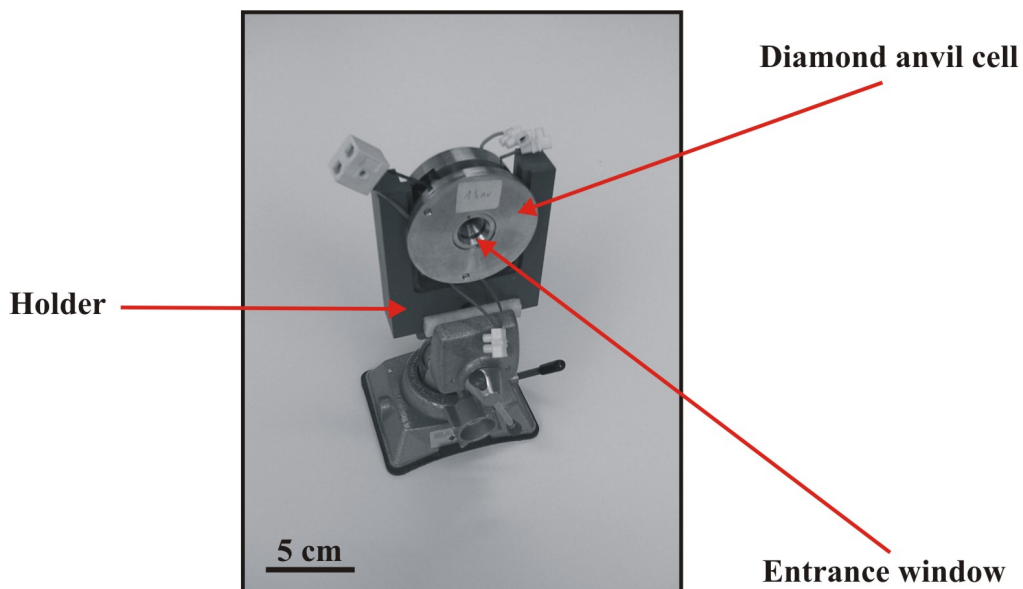


Figure 3.1.1: Photograph of a hydrothermal diamond anvil cell (DAC) of type Bassett et al. [BSB93] used for heavy-ion irradiation at GSI. During irradiation, the ions were passed through the entrance window to one of the diamond anvils and subsequent to the sample.

Before filling the cell, the two diamonds were carefully cleaned in order to avoid any damage or breakage of the diamonds during the alignment process. We used ordinary diamonds of type I, which means that they contain nitrogen impurities in rather large amounts ($> 0.1\%$). The shape of the diamonds was either 8-sided or 16-sided Drukker standards cut (see Figure 3.1.3) of different sizes. The typical dimensions of the diamond were the following: length 2.27 mm, table face 4 mm, and culet face 0.7 mm (definition

of table and culet face see Figure 2.2.1). Depending on the desired pressure in the cell, these values could vary slightly.

The alignment of the two diamond anvils is a crucial step of the filling procedure and is necessary in order to reach and maintain high pressure in the cell. A misalignment may lead to pressure losses and subsequently to diamond failure. For this purpose, the DAC was closed (without gasket and sample) by approaching the two diamonds against each other until the two culet faces came into contact. It should be mentioned, that two diamonds in contact represent a large risk of diamond damage, and therefore this procedure requires care. The alignment was checked with an optical microscope (Leica MZ8) by looking through one of the diamonds. In case of a misalignment, the DAC was dismounted and the two culet faces of the opposite diamonds were moved with respect to each other (both anvils could be moved separately). This procedure was done in several steps of dismounting and mounting the DAC, until the two culet faces matched. After that, with the help of interference fringes (Newton fringes), the parallelism of the two culet faces was checked. This alignment was also performed when the two diamonds were in contact, and the fringes caused by an air wedge between the nonparallel culet faces were observable by looking through one of the diamonds. Optimum alignment was obtained when the Newton fringes disappeared.

As a next step, the sample chamber was generated by preparing a rhenium gasket ($1 \times 1 \text{ cm}^2$, thickness $250 \mu\text{m}$). With some plastic modeling material, this plate was fixed to the lower half of the dismounted DAC on top of the diamond culet face. After that, the DAC was put together, and the two diamonds were squeezed against the metal plate by means of screws. The rhenium plate of a primary thickness of $250 \mu\text{m}$ was indented with the two diamonds on each side. During this pre-indentation procedure, the thickness of the metal foil was significantly reduced to a desired value depending on the pressure that was applied afterwards to the sample embedded in the gasket. To give an example: for a pressure of about 3 GPa , the thickness was reduced to $180 \mu\text{m}$, whereas for about 8 GPa a thickness of $130 \mu\text{m}$ was used. For checking the thickness, the DAC had to be dismounted and the gasket was taken out and investigated with a vernier gauge. This procedure was done in several steps until the desired thickness was reached. After that, the orientation of the gasket was marked on the lower half of the DAC. It should be mentioned that the process of pre-indentation increases the achievable pressure for a certain gasket thickness, because during this procedure the gasket material extrudes outward and builds up a supporting ring surrounding the pre-indented area. During the pressurization of the sample later on, this ring supports the stability of the gasket.

The preparation of the gasket was finished by drilling a hole through the center of the pre-indented area using a microdrill. The diameter depended also on the desired pressure value in such a way that the higher the pressure the smaller was the hole. For a pressure of about 3 GPa we used a hole diameter of $300 \mu\text{m}$, whereas $200 \mu\text{m}$ were used for about 8 GPa . Figure 3.1.2 displays the top view of a rhenium gasket after preparation. The thickness of the pre-indented area amounts to $130 \mu\text{m}$ and the hole diameter has a value of $200 \mu\text{m}$. The "finger print" of the diamond anvil can be clearly seen on the faceted

3.1 Diamond anvil cell (DAC)

walls of the pre-indented region. After the diamond alignment procedure and the gasket preparation, the actual loading of the DAC with a sample was performed. In order to remove some residues from the pre-indentation process, the two diamonds were carefully cleaned using ethanol and cotton buds. The same was done with the gasket. Especially the particles inside the hole from the drilling process had to be removed completely.

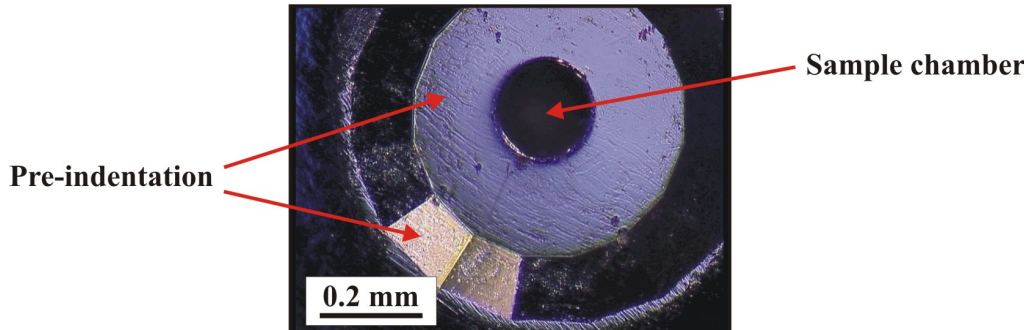


Figure 3.1.2: Photograph of a rhenium gasket after pre-indentation. The "finger prints" of the diamonds are visible as faceted vaults. By drilling a centered hole in the pre-indented gasket area, the sample chamber was created.

The preparation of samples of very small dimensions depends on the different materials. Layered solids such as phlogopite mica were cut under an optical microscope (Leica MZ8) with a sharp scalpel. Other materials such as zircon or quartz were crushed into small pieces by using a mortar. The sample size, received either by cutting or by crushing, depended strongly on the desired pressure value. For pressure values up to about 3 GPa, the sample size was around $250 \mu\text{m}$ in diameter. For higher pressures, for example more than 8 GPa, samples had to be significantly smaller (diameter: 100 to $150 \mu\text{m}$) because the hole in the gasket shrinks during the intensive squeezing of the two diamond anvils.

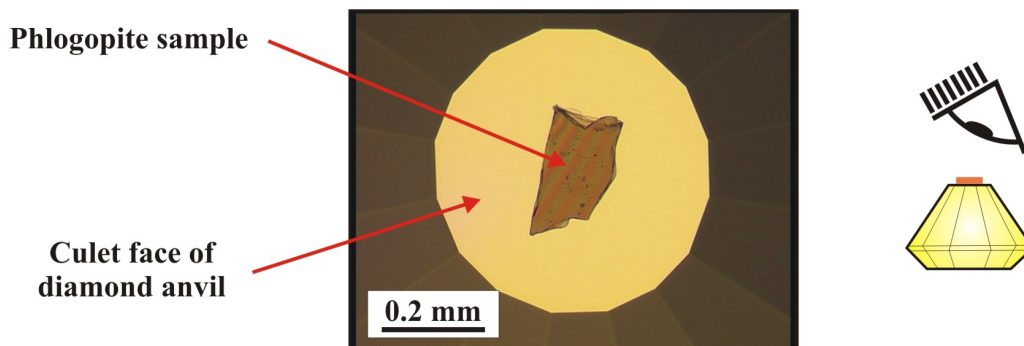


Figure 3.1.3: Photograph of diamond anvil together with phlogopite sample seen from the top, as indicated by the scheme on the right side. The shape of the diamond is a 16-sided Drukker standard cut with culet diameter of 0.7 mm.

Using a needle tip, a suitable sample was selected and transferred to one of the diamond anvils and placed in the center of the culet face as displayed for a phlogopite sample in Figure 3.1.3. After that, the gasket was placed on top of the diamond with the sample.

The alignment of the metal plate was performed with the help of the markings created during the process of pre-indentation. Subsequently, ruby (Cr^{3+} doped Al_2O_3) serving as a pressure calibrant was added to the pressure chamber either by strewing fine grains on top of the sample (see Figure 3.4.1, a) or by placing a small ruby crystal of a few μm beside the sample (see Figure 3.4.5). Afterwards, a droplet of the pressure medium, in our case methanol-ethanol mixture (4:1), was filled into the hole with a microsquirt. Then, the pressure chamber was closed by squeezing the two diamonds against each other and fixing the screws. In this way, the pressure medium was encapsulated, and evaporation was avoided. Using Raman spectrometry, the pressure was calibrated by focusing the laser beam on the ruby crystal inside the pressure chamber and measuring the fluorescence. In Figure 3.1.4, two such spectra are displayed, the left spectrum originating from a ruby at ambient conditions. In case of pressure, the spectrum shifts towards larger wave numbers as indicated by the right spectrum.

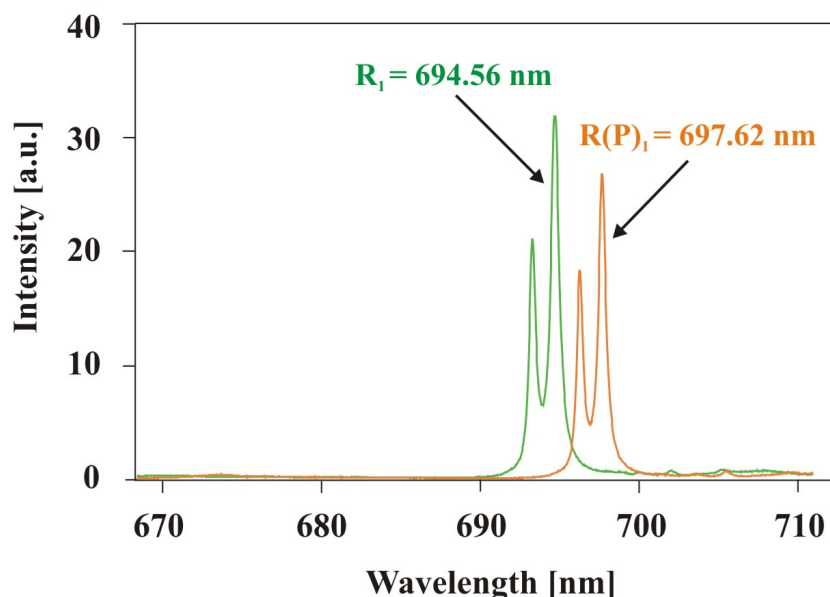


Figure 3.1.4: Raman fluorescence spectrum of ruby in DAC of sample G03. The left spectrum represents the fluorescence at ambient pressure conditions. While squeezing the two diamonds against each other, a pressure is generated in the sample chamber and a shift of the spectrum to a higher wavelength occurs. A shift of 3.1 nm corresponds to a pressure of 8.4 GPa using equation 3.1.

This shift has been examined in great detail by many groups [EGS89a, EGS89b, EME⁺⁸⁹], and was calibrated with other pressure calibration materials [BBP73, PBB75, MBSS78, MXB86, BXM86]. The pressure P inside the pressure chamber can be calculated from this wavelength shift $\Delta\lambda$ by the following equation:

$$P[\text{GPa}] = 2.746 \cdot \Delta\lambda[\text{nm}] \quad (3.1)$$

The precision of this calibration is in the order of 0.01 GPa. The procedure of screw

3.2 Irradiation facility

tightening and Raman measurement was repeated until the desired pressure value was reached. After this pressure adjustment, the DAC was ready for the irradiation with heavy ions at the GSI.

After irradiation, the DACs were brought back to Tübingen, and the pressure was checked again by Raman spectrometry. Subsequently, the screws were released, and the upper part of the DAC including one diamond was dismounted. In less than a minute the pressure medium evaporated from the pressure chamber. The gasket was carefully removed from the lower diamond without touching the sample on the diamond anvil. An adhesive tape was pressed against the culet face of the lower diamond and afterwards pulled away slowly. By doing so, the sample was attached to the glue tape. As a last step, this tape with the sample was fixed on a glass holder and kept in safe conditions for transportation and sample analysis.

Finally, it should be mentioned that all experiments were performed at room temperature except in one case, where a Bassett-type DAC filled with apatite was heated during the exposure to the ion beam. In this hydrothermal pressure experiment water was used as a pressure medium. The temperature was tuned by resistive heating with molybdenum wires, wrapped around the two diamonds. Due to excellent heat conduction, the diamonds transfer the heat rapidly to the sample. During the heating of sample and water, the pressure increases in the cell. If the density of the pressure medium is known (density changes by tightening the screws), the pressure can be determined for a certain temperature from the phase diagram of the pressure medium. The temperature was monitored and controlled using two thermocouples, fixed close to the culet face of the diamonds. This high-temperature experiment was mainly a test run for future studies. The principles and more technical details of hydrothermal experiments including the calibration of pressure and temperature can be found in [SBC92, BSBC93, BSB93].

3.2 Irradiation facility

The heavy-ion irradiation facility of GSI in Darmstadt (Germany) consists of two major accelerator units (Figure 3.2.1): (1) The universal linear accelerator UNILAC and (2) the heavy-ion synchrotron (SIS). All ion species from hydrogen to uranium, delivered from three different ion sources, can be accelerated. Two of these sources, located at the beginning of the UNILAC, inject ions with energies in the order of a few hundred keV. The third ion source produces highly-charged ions of primary energy 1.4 MeV/u [TRE+96]. At the end of the UNILAC, the ions have typically an energy of 11.4 MeV/u corresponding to about 15% of the speed of light. In the UNILAC experimental hall, several beamlines are available for irradiation experiments. In addition, about 1% of the ions are injected into the heavy-ion synchrotron (SIS), where in 10^5 revolutions per second in a ring with circumference 216 m the ions can be accelerated to a maximum energy of about 1.3 GeV/u corresponding to about 90% of the speed of light. The irradiations whose results are discussed in this thesis have been conducted at three different beamlines, corresponding to low, medium, and high energies:

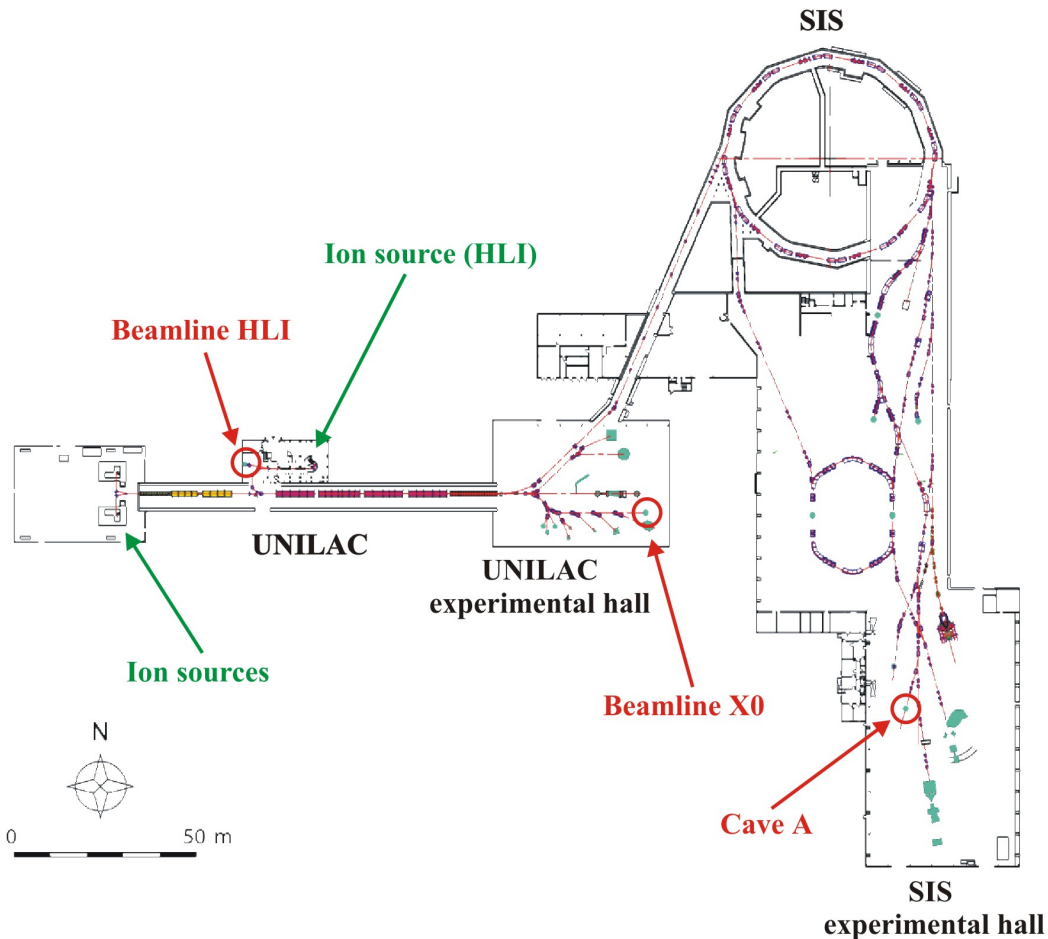


Figure 3.2.1: Scheme of GSI irradiation facility. The two major units are the universal linear accelerator (UNILAC) and the heavy-ion synchrotron (SIS). After acceleration, the ion energy can reach up to 11.4 MeV/u ($\approx 15\%$ of the speed of light) and 1.3 GeV/u ($\approx 90\%$ of the speed of light) when leaving UNILAC and SIS, respectively. Three beamlines indicated by circles were used for irradiations. All DAC-irradiations were conducted at cave A.

High-charge injector (HLI) beamline

At this beamline, the samples for the phlogopite preexperiments were irradiated using nickel ions of 1.4 MeV/u specific energy. The samples were inserted into an high-vacuum chamber. The ion flux was monitored via the ratio of beam current on a copper aperture mounted in front of the sample. Before irradiation, the current on this aperture was calibrated by means of a Faraday cup.

X0 beamline

This beamline is located at the end of the experimental hall of the UNILAC. The energy is typically 11.4 MeV/u , unless degrader foils are mounted in front of the samples. The ion flux is monitored with the help of a on-line secondary electron detector consisting

3.2 Irradiation facility

of three aluminum foils and calibrated with a Faraday cup. Due to the Al-foils (total thickness $\approx 3\mu m$), the final energy on the sample is reduced to 11.1 MeV/u . Irradiations are typically performed with a defocused beam of size $5 \times 5\text{ cm}^2$. The samples are inserted into a high-vacuum chamber using a remote-control sample inlet system driven by three step motors [Spo80].

Cave A

This high-energy irradiation beamline is located in the SIS experimental hall as displayed in Figure 3.2.1. Due to the larger ion range, all irradiations of samples inserted into a diamond anvil cell were performed at this beamline. The samples were positioned behind a $100\mu m$ aluminum exit window of the beamline, the irradiation therefore took place in air. The ion flux is, similar to the beamline of X0, observed by a secondary-electron transmission monitor (SEETRAM) consisting of three titanium foils, each $10\mu m$ thick. Due to the filling and acceleration cycles of the SIS, which are in the order of 1 s , the flux is in general smaller than in the case of the HLI or X0. We typically used a maximum flux of about $1 \times 10^8 \text{ ions s}^{-1}\text{cm}^{-2}$. The ion beam was focused to a spot of diameter between 3 and 10 mm . Smaller spot sizes (e.g. 0.2 cm^2) were helpful to reach high fluences within feasibly short exposure times. Alternatively to a spot irradiation, the ion beam was in some cases scanned over an area of about $20 \times 20\text{ cm}^2$. In this mode, the distribution of the fluence (ions/cm^2) is more homogeneous within the scanned area. The SIS extraction time of the ion pulse was in the order of several nanoseconds.

Table 3.2.1: Comparison of specific energies available at three different beamlines. With the SRIM00 code the corresponding range of uranium ions in diamond was calculated. It is obvious that only at cave A a DAC-irradiation using 2-3 mm thick diamonds is possible.

Beamlines	Specific energy [MeV/u]	Energy of ^{238}U ions [GeV]	Range of ^{238}U in Diamond
HLI	1.4	0.3	$13\mu m$
X0	11.4	2.7	$66\mu m$
Cave A	50-1300	11.9-309	0.36-30 mm

Table 3.2.1 displays the ion energies used at the different beamlines and lists the range of uranium ions in diamond calculated with the SRIM00 code [ZB99a]. Given by the limited range of the UNILAC beam, it is obvious that the high-energy beamline of cave A has to be used for samples mounted in the DAC. The results of the range measurements for diamond (presented in chapter 4.1) demonstrated that, depending on ion species and diamond length, energies in the order of 200 MeV/u are required in order to reach the sample under investigation.

In the following, the procedure of a DAC heavy-ion irradiation will be described and further equipment of cave A will be discussed. Figure 3.2.2 displays a scheme of a DAC irradiation in cave A. The DAC was placed 45cm behind the exit window of the beamline. To guarantee beam exposure of the sample, a careful alignment of the DAC is essential,

especially when using the focused beam mode. The alignment of the DAC was performed in the following way: First, a fluorescent screen was put at the later position of the DAC 45 cm behind the exit window. At each ion pulse, the fluorescence of the beam was observed with the help of a camera. By means of steering magnets, the focused beam was shifted into the center of a reticule on the fluorescent screen. Subsequently, this reticule was monitored with an align telescope placed about 3 m behind the beamline, and a second reticule inserted the telescope was brought into match with the first one. After this procedure, the screen was replaced by the DAC, which was inserted into a holder and placed on a conveyor belt. Due to the magnification of the align telescope it was possible to observe, counter to the ion beam direction, the second diamond anvil opposite to the entrance diamond. Finally, the DAC was aligned with respect to the reticule of the align telescope.

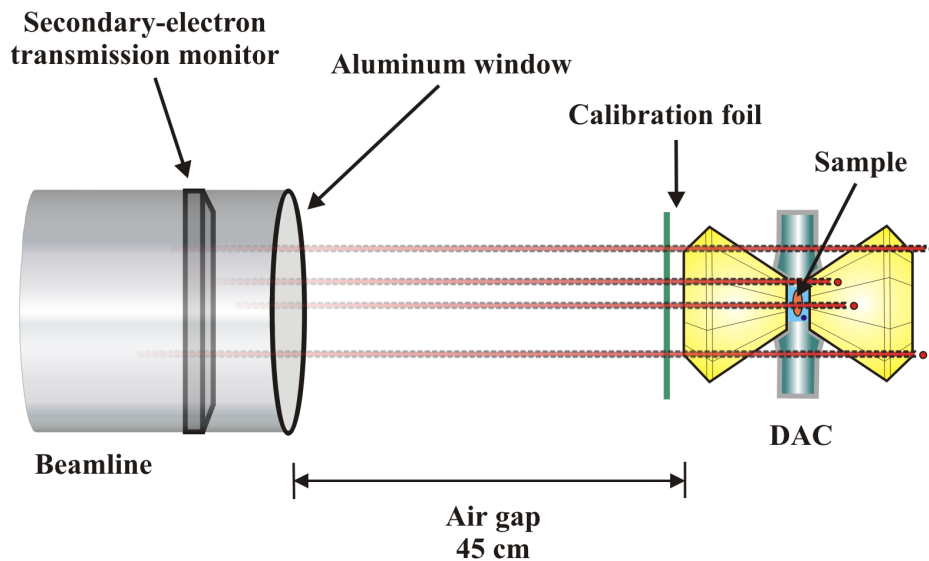


Figure 3.2.2: Scheme of DAC irradiation in cave A (not to scale). The ions passed through a secondary-electron transmission monitor, an aluminum window, and 45-cm air before reaching the diamond anvil cell. After traveling through one of the anvils of about 2 mm length, the ions completely penetrated the sample and came to a complete stop within the second anvil.

The beam energy was selected in such a way that the ions traveled completely through the SEETRAM detector, Al exit window of the beamline, 45 cm air, first diamond anvil, and finally through the sample. The ions came to a complete stop within the second diamond anvil.

During the beam exposure, the correct alignment of the DAC could be cross-checked, because each ion pulse produced a bright luminescence signal in both diamonds. The irradiation was stopped when the desired fluence was reached according to the in-situ SEETRAM detector. The duration of a DAC irradiation lasted generally between 5 and 60 minutes, depending on the available flux from the accelerator and the desired fluence value. To have a second independent fluence cross-check, thin samples ($10 \mu\text{m}$)

3.2 Irradiation facility

of polycarbonate or/and muscovite mica were mounted in front of the diamond anvil on the ion entrance side as displayed in Figure 3.2.3.

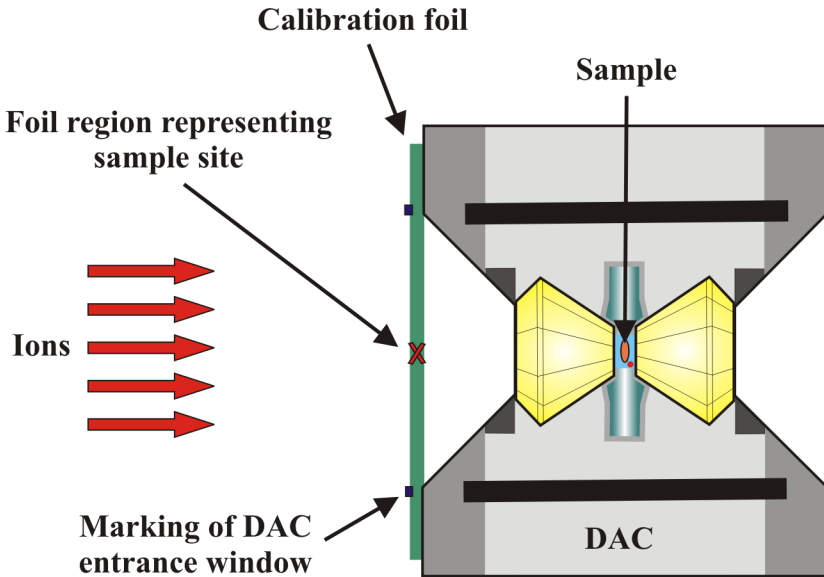


Figure 3.2.3: Schematic of a DAC displaying the steel chase, diamond anvils, and the sample. After fixing the calibration foil, the entrance window position of the chase was marked. Due to the symmetrical construction of the DAC, the center within the marked region corresponds to the sample location (cross) with respect to the direction of the ion beam.

These samples, having a low threshold for track creation, served as track detectors by analyzing the number of ions either by chemical etching (polycarbonate) or by SFM on latent ion tracks (muscovite). Special markings on the calibration foils were needed in order to identify the area that corresponds to the sample position.

Last, it should be mentioned that the experimental work connected with the DAC irradiation was successively improved at each beamtime. But for future irradiations, some further development will be necessary. A crucial point is the correct alignment of the DAC especially when a focused ion beam mode is used. Even though the alignment could be done with the help of a telescope, a small inclination of the longitudinal DAC axis against the beam axis was not avoidable and could lead to deviations of the ion fluence at the sample site. A special DAC holder has to be constructed, which can be positioned on the conveyor belt in such a way that an automatical alignment of the DAC axis with respect to the beam axis is guaranteed. Furthermore, the alignment of the DAC with respect to the reticule of the telescope was performed by moving the DAC either with the conveyor belt or by the holder itself. For the fine tuning with sub-mm precision this was not an easy task. The movement of the DAC together with the sample into the ion beam should be done afterwards with a fine-tuned step motor. These improvements are in progress.

3.3 Preexperiments

3.3.1 Energy deposition of heavy ions in natural diamond

As mentioned above, we apply high hydrostatic pressure in the GPa range with the help of a DAC, in which a microscopic specimen is mounted between two diamond crystals of thickness 2-3 mm each (see chapter 3.1). To irradiate the sample with heavy ions, these projectiles require kinetic energies in the order of several ten GeV to pass first one of the diamonds and then the specimen with a thickness of typically 50-100 μm . In order to realize for a given purpose certain values of kinetic energy and energy loss in the sample, one must take into account the energy loss in the diamond. Since there are no experimental data available describing the range and stopping power of GeV heavy ions in natural diamond with a length of a few millimeters, a preexperiment was performed with a 2.27 mm thick diamond sample. This anvil was irradiated with heavy ions of given kinetic energy. The residual energy of the projectiles, when exiting the diamond, was determined in a stack of thin polymer foils mounted behind the diamond.

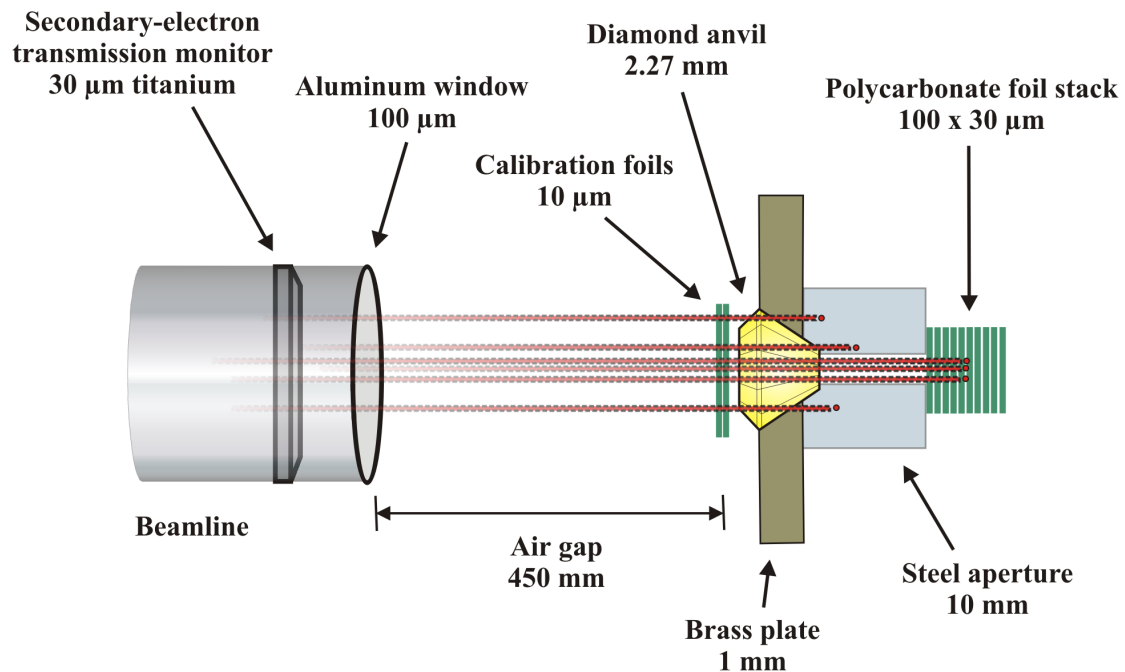


Figure 3.3.1: Schematic of the experimental setup (not to scale). Before reaching the 2.27-mm thick diamond, the uranium ions pass through the 30- μm thick titanium beam monitor, exit the beam line via a 100- μm aluminium window, and travel 45 cm in air. After the diamond, they come to a complete stop deep inside the polycarbonate foil stack.

By means of chemical etching, the tracks were converted into microscopic pores. Analyzing the pore density at different positions within the stack allowed us to determine the range in the polymer. Based on this range value, the energy loss in the polymer stack

3.3 Preexperiments

and thus the energy of the ions immediately behind the diamond could be determined. Together with the given initial energy, the amount of energy deposited in the diamond could be extracted. This value was afterwards compared with calculations of different codes. As a "side product" the energy-straggling of the ions could be investigated.

Figure 3.3.1 depicts the experimental setup in cave A. The irradiation was performed with ^{238}U ions of primary energy 50.3 GeV at a fluence of $\approx 6 \times 10^8 \text{ ions/cm}^2$. The beam intensity was controlled by a secondary-electron transmission monitor (SEETRAM) consisting of three Ti-foils, each $10\text{ }\mu\text{m}$ thick. For our studies, we used a natural faceted diamond from Scimed (Isselburg, Germany) with a table face (directly exposed to the ions) of diameter 4 mm , and a culet face of diameter 0.7 mm . This crystal was mounted in a circular aperture of a 1-mm thick brass plate. Behind the diamond, a 10-mm thick steel plate with a round aperture of diameter 0.5 mm was aligned axially with the diamond center by optical microscopy. This mask guaranteed that only the central part of the ion beam traveling through the thickest region of the crystal reached the following foil stack. The beam fraction that passed through the faceted outer zones of reduced thickness was thus absorbed in the steel plate. In front of the diamond, we mounted two $10\text{-}\mu\text{m}$ thick foils of polycarbonate (PC, Makrofol from Bayer). Directly behind the steel aperture, a stack of 100 PC foils, each $30\text{ }\mu\text{m}$ thick, served as range detector. The entire assembly was positioned in air, 45 cm behind the $100\text{-}\mu\text{m}$ Al exit window of the beamtube. In summary, the ions passed $30\text{-}\mu\text{m}$ Ti, $100\text{-}\mu\text{m}$ Al, and 45-cm air before reaching the diamond.

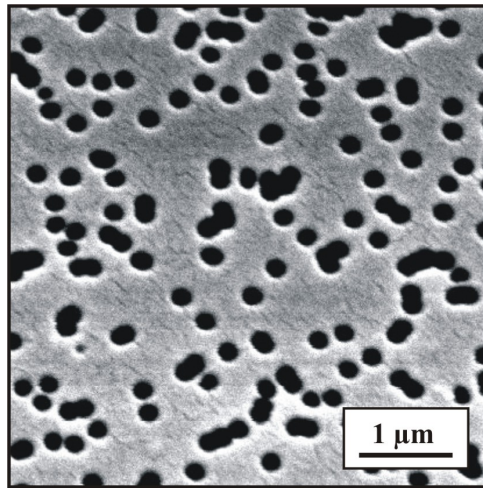


Figure 3.3.2: SEM micrograph of the seventh polycarbonate foil of the stack ($180\text{ }\mu\text{m}$ behind the diamond). 8 min of etching in 6N NaOH at 50°C transformed the ion tracks into circular pores with diameter $\approx 2\text{ }\mu\text{m}$.

Chemical etching of the irradiated polymer foils converted the individual tracks into microscopic pores that were identified by SEM. The etching was performed in aqueous 6 N NaOH solution for 8 min at 50°C . Figure 3.3.2 shows a SEM image of a foil surface section. The mean areal track density of each foil was determined by averaging the pore density of five such micrographs recorded at different locations. The pore density of

the foils in front of the diamond provided a second control of the applied ion fluence, independent of the online beam monitor.

3.3.2 Phlogopite irradiations under ambient pressure

Phlogopite is a material suitable for first high-pressure irradiations, because of its interest for geochronology. To date it is not clear to which extent fission tracks that were created within the Earth's crust are influenced by conditions of elevated pressure and temperature. Phlogopite samples cleave easily along the sheets and the conditions for chemical track etching are well known. Moreover, etched tracks in phlogopite exhibit a stopping power threshold where the etch pit geometry changes from hexagonal to triangular. This transformation is possibly caused by a transition from a continuous to a discontinuous damage morphology [HN98, LGM^{+02a}]. In our experiments, this transition is a probe for possible changes of the track damage, caused by hydrostatic pressure applied during irradiation. The etch pit geometry was inspected by scanning probe microscopy.

In order to investigate details of this transition such as sharpness and critical energy loss value, several dedicated irradiations were performed at ambient conditions using a nickel ion beam at the HLI. The phlogopite originated from the Kerguelen islands (Indian Ocean, French territory) and was prospected by B. Moine of the Département de Géologie-Pétrologie-Géochimie, Université Jean Monnet in St. Étienne (France). This natural phlogopite has the following chemical composition, the numbers giving wt.%: SiO₂ – 35.91(32) , TiO₂ – 6.97(7) , Al₂O₃ – 15.17(12) , Cr₂O₃ – 0.04(2) , Fe₂O₃ – 1.92(2) , FeO – 9.78(11) , MnO – 0.07(2) , MgO – 15.30(9) , Ba – 0.28(5) , Na₂O – 0.71(4) , K₂O – 8.80(8) , H₂O – 4.06(2) . The age of this mineral is between 8 and 10 Ma [GLK⁺⁰³]. In order to exclude natural tracks from fission fragments or ARTs, all specimens were annealed at about 500°C for 3.5 hours [Gög99].

Table 3.3.1: Irradiation parameters for the phlogopite samples. The ⁵⁸Ni ions had an initial energy of $\approx 81 \text{ MeV}$, the energy loss was calculated with the SRIM00 code.

Sample N°	PET Degrader foil [μm]	Ion energy [MeV]	Energy loss [keV/nm]
1	0	81.2	10.4
2	5	52.5	10.1
3	8	31.3	8.7
4	10	20.7	7.3
5	11	16.1	6.6
6	12	11.7	5.6
7	13	8.1	4.5
8	15	3.2	2.4

For the irradiation, the phlogopite was cut into slices of $\approx 0.5 \text{ cm}^2$ area and 1 to 2 mm thickness. With a HF-resistant nail lacquer, each small sample was fixed on a plastic

foil holder and additionally sealed sideward against the acid. Subsequently, a part of the samples were covered with PET foils of different thicknesses, to reduce the initial ion energy and thus the energy loss at the sample surface.

^{58}Ni was used as a projectile because its energy loss covered the region where the shape transition occurs. The initial ion energy was 1.4 MeV/u corresponding to 81.2 MeV . Table 3.3.1 summarizes the irradiation parameters for the different samples. Two sets of samples were irradiated, one with 4×10^6 , the other with $1 \times 10^8 \text{ ions/cm}^2$. The energy of the ions after passing the degrader foil and the energy loss at the sample were calculated with the SRIM00 code [ZB99a].

After irradiation, all samples were etched with 4% HF at room temperature, by immersing the higher- and lower-fluence samples for 3 and 10 min, respectively, into the etchant. The low-fluence samples were covered after etching with a thin gold layer and then inspected with scanning electron microscopy. The other samples were investigated with SFM to determine diameters and depths of the etch pits.

3.4 High-pressure irradiations

3.4.1 Phlogopite

In three beamtimes, all together 8 phlogopite samples (P01 to P08) were irradiated at the SIS beamline of cave A (see Table 3.4.1). Five of the specimens were exposed to the ion beam at high pressures between 1.9 and 8.4 GPa . In addition three irradiations were performed with control samples at ambient pressure but otherwise similar conditions. Six samples were investigated after etching with scanning probe microscopy (SFM, SEM), and two specimens were analyzed with transmission electron microscopy (TEM). The ion fluence was chosen with respect to these techniques.

The two parameters of interest are first of all the pressure applied on the sample, but also the ion energy loss value, which is responsible for the extent of radiation damage. For this reason, irradiations were performed (1) with ions having different dE/dx , while the phlogopite samples were exposed to the same pressure, and (2) with ions having the same dE/dx value and phlogopite samples at different pressures.

Close to the energy-loss threshold, the damage along the tracks is typically discontinuous [MHAS⁺93]. Not each impinging ion creates an etchable track in the surface region, and the number of etched pores is smaller than the applied fluence. Each sample was therefore irradiated through polycarbonate foils (mounted in front of the DAC). The density of etched tracks of the calibration foils was compared with the track density on the phlogopite sample itself.

Sample preparation and irradiation of DAC

The phlogopite specimens used for heavy-ion irradiations under high pressure were of the same origin as the one used for the preexperiment. After annealing, miniature samples were prepared by repeated cutting of the phlogopite under an optical microscope (Leica MZ8). The best samples were chosen with respect to clean and flat cleavage planes. After that, DACs were loaded, and the pressure was adjusted to the desired values as described in chapter 3.1. The control samples irradiated under ambient conditions were loaded in the DAC, but without pressure medium and the two diamonds were not squeezing against each other. Figure 3.4.1 displays the same phlogopite sample (a) inside a DAC under pressure, together with ruby grains used for pressure calibration, and (b) dismounted with a human hair for comparison.

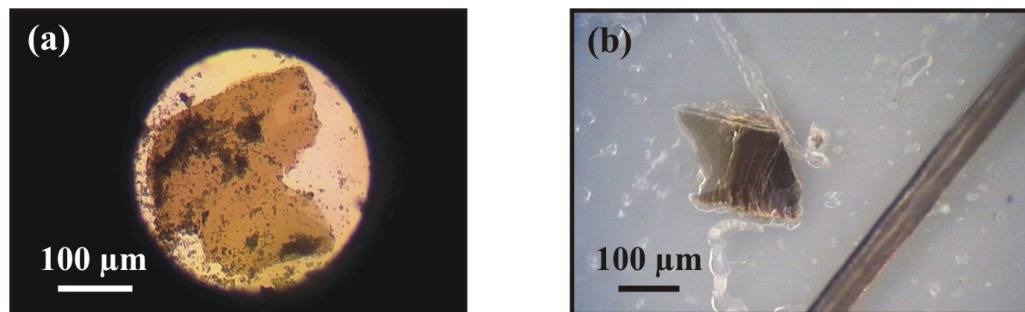


Figure 3.4.1: Optical micrographs of a miniature phlogopite specimen for high-pressure irradiations. Image (a) gives a view through one of the diamond anvils displaying the phlogopite sample inside a DAC together with grains of the pressure calibration medium under 2.2 GPa. Image (b) shows the dismounted irradiated sample together with a human hair for comparison.

For irradiations, three heavy-ion species (^{238}U , ^{197}Au , and ^{124}Xe) were used. The energy loss vs. energy diagrams, calculated with the SRIM00 code are displayed in Figure 3.4.2. With the help of such diagrams, the kinetic energy at the sample site (E_{sam}) could be determined for a desired energy loss value (dE/dx). Using E_{sam} and taking into account the diamond thickness, SEETRAM detector, Al exit window, and 45 cm air gap, also the beam energy (E_{acc}) delivered from the accelerator could be calculated (see also 4.1). The numbers are given in Table 3.4.1. The fluence applied for these irradiations was between 3×10^7 and $2 \times 10^{10} \text{ ions/cm}^2$. In the case of high-fluence irradiations, the DACs were kept for a few days within a steel treasury until the activation had dropped. Before dismounting the phlogopite samples, the pressure was checked again in order to detect a possible pressure release.

Table 3.4.1 gives an overview of all phlogopite samples irradiated under high pressure as well as of the corresponding control samples irradiated under ambient conditions. The important irradiation parameters and the sample analysis techniques are also displayed.

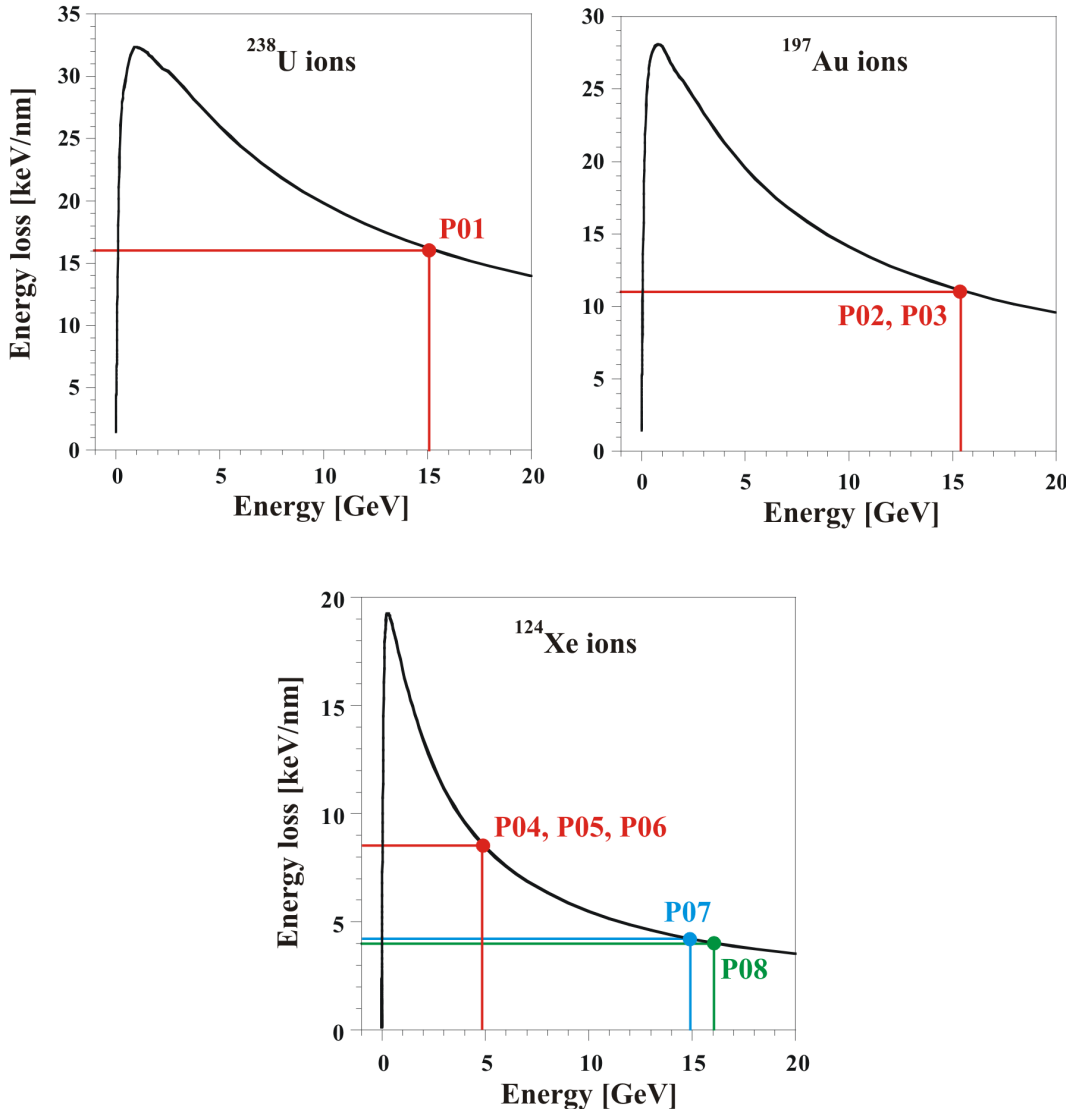


Figure 3.4.2: Energy loss vs. total energy graphs for the irradiations of phlogopite with U, Au, and Xe ions, as calculated with the SRIM00 code. The energy losses for the samples were selected, and the corresponding energy at the sample E_{sam} could be extracted. All numbers are given in Table 3.4.1.

Investigation of calibration foils

In the case of phlogopite, the ion fluence applied to the samples was, except for P02 and P03, small enough to use etched tracks in polycarbonate foils for a second independent fluence cross-check. After irradiation, the foils were dismounted and subsequently etched in 6 N NaOH at 50°C for a certain time interval (from 3 to 35 min) depending on the fluence. After etching, the foils were fixed on a holder and covered with a thin gold layer. In the marked region of the calibration foil, corresponding to the location of the sample, several images were taken by means of SEM, and a mean etch pit density was

Table 3.4.1: Overview of all phlogopite irradiation parameters such as accelerator energy (E_{acc}), energy at the sample site (E_{sam}), energy loss (dE/dx) and fluence.

Sample Nº	Ion	Pressure [GPa]	E_{acc} [GeV]	E_{sam} [GeV]	dE/dx [keV/nm]	Fluence [cm $^{-2}$]
P01	^{238}U	2.2	47.6	15.1	16.0	1×10^9
P02	^{197}Au	ambient	59.1	15.4	11.0	2×10^{10}
P03	^{197}Au	1.9	59.1	15.4	11.0	5×10^{10}
P04	^{124}Xe	ambient	20.7	4.8	8.5	4×10^7
P05	^{124}Xe	2.6	20.7	4.8	8.5	4×10^7
P06	^{124}Xe	8.4	20.7	4.8	8.5	3×10^7
P07	^{124}Xe	ambient	16.2	14.9	4.2	1×10^8
P08	^{124}Xe	3.2	25.7	16.0	4.0	5×10^8

determined.

One foil was inspected with SFM in order to get more information about the fluence distribution within the beam spot. A pattern was recorded by measuring the etch pit density at 25 locations on the foil, distributed in a square of 3 mm length of a side, having the sample region in the center. For this purpose, the transparent foil was put after etching on a SFM-holder, which was covered with millimeter graph paper. With the help of an optical microscope (Leica MZ6) with integrated video camera (Kappa CF7), the SFM tip was adjusted with a precision of about 100 μm to each of the points. Subsequently an image of a size of $3 \times 3 \mu\text{m}^2$ was taken, and the etch pit density was determined.

Etching of phlogopite samples and inspection with scanning probe microscopy

After transportation, the adhesive tape with the sample was removed from the glass holder and was fixed upside down on a SFM holder with another double-side adhesive tape. All samples that were inspected with SFM and SEM were etched with 4% HF at room temperature. In the preexperiment, larger phlogopite samples were fixed with lacquer on a plastic foil holder and were inserted into a bath of 4% HF, using a stirrer to carry away the etch products. Due to the time limitation of DAC irradiations at the SIS, a rather small number of irradiated samples was available, and a possible loss during the etching process was not acceptable. Therefore, a modified etching technique was used that avoids large amounts of etchant and a stirrer. The holder with the sample was put into a small plastic vessel. Then, the etch solution was carefully released with a squirt by giving a single droplet every 20 seconds onto the sample. The phlogopite specimens were etched in the same way for a time interval of 1 to 5 minutes depending on the fluence and energy loss. After the etching process, the SFM holder with the samples was dipped successively into two glass vessels filled with distilled water to remove the etchant and possible residues. Usually, the samples were kept over night at controlled room temperature conditions in order to guarantee a complete drying.

3.4 High-pressure irradiations

All etched samples were investigated with a commercial SFM (NT-MDT Co. Russia) under a controlled atmosphere of about 48% humidity and 21°C. Due to the miniature of the phlogopite specimens inserted in a DAC, an optical microscope (Leica MZ6), having a long working distance with integrated video camera (Kappa CF7), was used to monitor the tip position with respect to the sample surface. After the approach, the phlogopite specimens were investigated using topography images of the contact mode, and the mean etch pit density as well as the average diameter and depth of the etch pits were determined.

After etching and SFM analysis, the samples P04, P05, and P06 were additionally inspected with SEM (Philips, XL30). For this purpose, the adhesive tapes together with the samples were carefully removed from the SFM holder and placed on a SEM holder. Afterwards, the samples were covered with a thin gold layer, and several SEM micrographs were recorded. Samples P02 and P03 were inspected by means of transmission electron microscopy (without etching) in Bayreuth. Some details of this technique are given in the next chapter.

3.4.2 Graphite

Three miniature HOPG (provided by Advanced Ceramics Co.) specimens (G02, G03, and G04) were prepared for DAC, analogous to the phlogopite, by successive cutting. The DAC-filling procedure including gasket and pressure medium was exactly the same as for phlogopite, and a detailed description can be found in chapter 3.1. A certain pressure value was chosen for each sample (see Table 3.4.2) and was adjusted at the DAC. Figure 3.4.3 displays a HOPG sample enclosed in a DAC (at 8.4 GPa) shortly after filling and pressure adjustment. The image was taken through one of the diamond anvils.

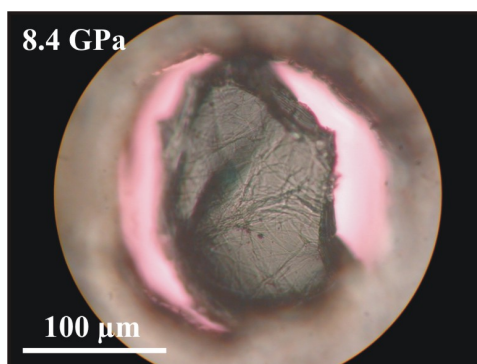


Figure 3.4.3: Optical micrographs of a miniature HOPG specimen for high pressure irradiations. The image gives a view through one of the diamond anvils displaying the graphite sample inside a DAC under 8.4 GPa.

The three DACs were irradiated with ^{238}U and ^{197}Au ions during three different beam times. The graphite specimens enclosed in a DAC were irradiated in the same way as

the phlogopite samples with GeV ions through one of the two diamond anvils. Figure 3.4.4 displays the energy loss vs. energy diagrams, calculated with the SRIM00 code. It should be mentioned that some of the HOPG irradiations were performed together with phlogopite irradiations. In both cases, DACs of unequal diamond thickness were used, and also different energy loss values on both kinds of sample were planned. Therefore, a compromise in the accelerator energy had to be found, and for this reason the dE/dx values in the case of the HOPG irradiations under pressure are not exactly the same but only of similar size. The HOPG samples enclosed in a DAC were irradiated with an ion fluence of 1.0×10^{11} and $1.9 \times 10^{11} \text{ ions/cm}^2$. Such high fluences were selected with regard to sample analysis with Raman spectroscopy and transmission electron microscopy (TEM). All irradiation parameters are displayed in Table 3.4.2.

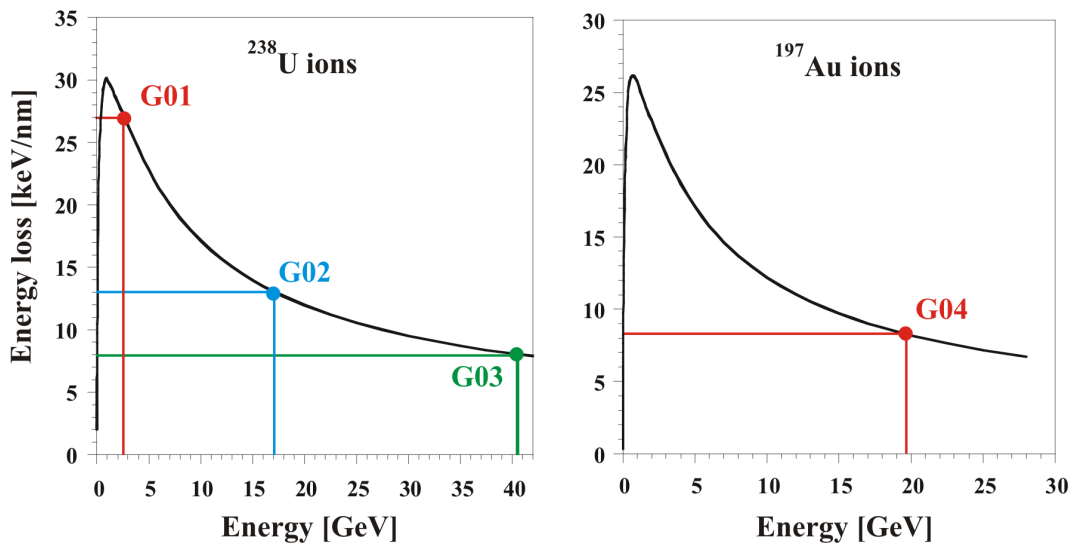


Figure 3.4.4: Energy loss vs. energy graphs for graphite irradiations calculated with the SRIM00 code. The energy losses for the samples were selected, and the corresponding energy at the sample E_{sam} could be extracted. All numbers are given in Table 3.4.2.

The use of polycarbonate foils for fluence calibration is limited to values of about $10^{10} \text{ ions/cm}^2$. For that reason we choose muscovite mica as a calibration standard for the graphite irradiations. The $10\text{-}\mu\text{m}$ thick sheets were after irradiation investigated by means of SFM without etching, and the areal density of the latent ion tracks was determined.

In the case of HOPG, one control sample (G01) was irradiated at ambient pressure. This irradiation was conducted at the UNILAC-beamline of X0, which means that the sample was not inserted in a DAC (without pressure) but directly exposed to a ^{238}U beam of 2.6 GeV . In contrast to the SIS-beamline of Cave A, where all irradiations are conducted in air, at X0 all samples have to be inserted in a vacuum chamber. So the "ambient" irradiation condition of sample G01 means actually about 10^{-5} mbar . However, in the further discussions this sample is treated as control sample representing ambient

3.4 High-pressure irradiations

irradiation conditions. All irradiation parameters are summarized in Table 3.4.2, kinetic energy and energy loss are additionally displayed in Figure 3.4.4.

After irradiation and activation release, the pressure in the DACs of G02, G03, and G04 was checked in order to detect possible pressure reduction caused by high fluences (in the order of $10^{11} \text{ ions/cm}^2$). Subsequent to that, the samples were dismounted and prepared for further analysis.

Table 3.4.2: Overview of all HOPG irradiations. Important ion parameters are given such as accelerator energy (E_{acc}), energy at the sample site (E_{sam}), energy loss (dE/dx) and fluence.

Sample Nº	Ion	Pressure [GPa]	E_{acc} [GeV]	E_{sam} [GeV]	dE/dx [keV/nm]	Fluence [cm $^{-2}$]
G01	^{238}U	ambient	2.6	2.6	27.0	1×10^{11}
G02	^{238}U	0.5	76.2	17.1	13.0	1.9×10^{11}
G03	^{238}U	8.4	71.4	40.5	8.0	1×10^{11}
G04	^{197}Au	12.1	59.1	19.7	8.3	1×10^{11}

All samples were investigated with Raman spectroscopy by H. Keppler, B. Binder, and A. Dorn at the Institute of Mineralogy of University of Tübingen . A Raman spectrometer from Dilor (LabRam) was used with a Labspec 208 software package. The light source was a water-cooled Ar-laser of wavelengths 488 (blue) and 514.5 nm (green). Further measurements have been performed at the Institute of Mineralogy of University of Frankfurt/Main. There, a Raman spectrometer from Renishaw was available with a HeNe-laser of 633 nm (red) and a Nd:YAG-laser of 532 nm (green).

Additionally to the Raman measurements, also TEM investigations were performed by F. Langenhorst at the Bayerisches Forschungsinstitut für Experimentelle Geochemie und Geophysik, University of Bayreuth . A 200 keV Philips CM20 FEG (field emission gun) microscope equipped with a Gatan PEELS 666 detector for electron energy loss measurements was used. The resolution of the microscope is between 0.2 and 1 nm. All TEM investigations were performed on the wedge-shaped sample boundary region, where the thickness of the samples was in the order of about 50-100 nm to allow the penetration of the electron beam. This method was preferred, e.g., to ion beam thinning because of its danger of further material modifications. Beside TEM images also EELS spectra and electron diffraction patterns have been recorded.

The reference sample G01 was additionally inspected by means of scanning tunneling microscopy (STM). For this investigation the same microscope was used as for the SFM measurements of the phlogopite samples. As mentioned earlier, the reference sample was irradiated at the beamline of X0 without being inserted into a DAC. For this reason a significant larger sample ($5 \times 5 \text{ cm}^2$) was used, which allowed the inspection with STM.

3.4.3 Apatite, zircon, rutile, and quartz

In order to test further solids whether they are suitable for future high-pressure irradiation experiments, several other minerals were irradiated under hydrostatic pressure conditions during one beam time. A detailed theoretical description and a summary of previous findings, concerning experiments of these materials at high pressure and high temperature, and also including exposure to irradiation at ambient conditions will not be presented in this thesis. For this reason, they are very shortly introduced in the following.

Apatite ($\text{Ca}_5\text{F}(\text{PO}_4)_3$, density 3.15 g/cm^3) is a calcium phosphate with a hexagonal structure. This mineral is widely distributed in igneous, sedimentary, and metamorphic rock types. Radioactive nuclei can be incorporated in the crystal and, therefore, it is also used for dating. Apatite has industrial importance for the production of fertilizers.

Zircon (ZrSiO_4 , density 4.70 g/cm^3) is a silicate with tetragonal crystal structure, occurring in granitic pegmatites, but also in metamorphic environments. It is found also in upper mantle conditions. It is one of the most important host minerals for U and Th, and is therefore also used for dating. Zircon is a very popular gemstone. Gems of all different colors are available, and colorless crystals are used as diamond fake. There are many localities for this mineral in the world. Famous European places are the Eifel Mountains in Germany and the Ural Mountains in Russia.

Rutile (TiO_2 , density 4.25 g/cm^3) exhibits a tetragonal structure, where the crystalline forms can easily twin at a 60-degree angle and form "elbow twins" and cyclic twins of six or eight components. Rutile is a primary mineral formed over a wide range of pressures and temperatures in igneous rocks. Rutile is a major ore of titanium, a metal used for high tech alloys because of its light weight, high strength and resistance to corrosion.

The mineral quartz (SiO_2 , density 2.65 g/cm^3) consists of an ordered lattice of SiO_4 -tetrahedra. It is one of the most abundant mineral in the Earth's crust. It can be found in nearly every geological environment, and many varieties of quartz occur in nearly all types of igneous, metamorphic and sedimentary rocks. Because of this, quartz has been extensively studied, taking into account also the intensive technological use.

All samples used for irradiation were natural minerals. The apatite sample came from Mexico (Durango), the zircon from France, the rutile from Brazil (Minas Gerais), and the quartz from Germany (Alps). Samples of zircon, rutile, and quartz were annealed for 24 hours at 700°C , and the two apatite samples were annealed for 24 hours at 500°C . Afterwards, miniature specimens were prepared with the help of a mortar. This means that for these crystals a different preparation technique was used than in the case of the layered samples phlogopite and graphite. However, the DAC filling procedure for zircon, rutile, and quartz was exactly the same as for phlogopite and HOPG. Figure 3.4.5 displays a micrograph of the samples after the filling procedure and pressure adjustment. The images were taken through one of the two diamond anvils.

As already mentioned in chapter 3.1, the irradiation of one of the two apatite samples

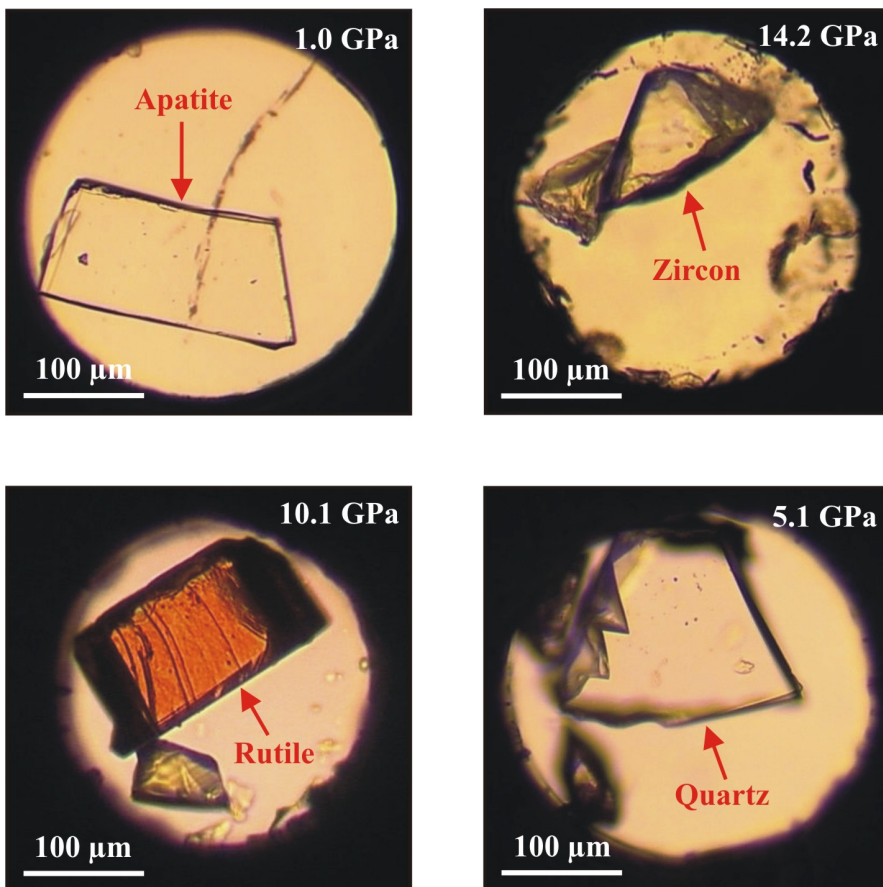


Figure 3.4.5: Optical micrographs of various minerals for high pressure irradiations. The image gives a view through one of the diamond anvils displaying the samples indicated by arrows. In the case of zircon, rutile, and quartz a ruby crystal is visible in the vicinity of the sample. In the hydrothermal experiment of apatite, the ruby is missing.

(A02) was unique insofar as the sample was simultaneously heated and exposed to a hydrostatic pressure. The temperature was adjusted to about 300°C , which was monitored with thermocouples placed near the ends of the diamonds (culet face). We kept the pressure medium (water) density roughly at about 1 g/cm^3 , which means that at a temperature of 300°C a pressure of about 1 GPa was reached. In this hydrothermal experiment, we did not use a pressure calibrant (e.g. ruby), because the heating was performed while irradiating the DAC, and therefore Raman measurements were not possible. It should be mentioned, that we observed an temperature increase to about 430°C after irradiation. For that reason, we assume that this was the actual temperature during the entire heating time of about 15 min . Figure 3.4.5, displaying the apatite sample, shows that the ruby crystal is missing. Another apatite sample (A01) was also inserted in a DAC, but kept at ambient temperature and pressure. It was used as a control sample for A02.

All five DACs were irradiated in exactly the same way as for phlogopite and graphite,

Table 3.4.3: Overview of high pressure irradiations conducted with apatite, zircon, rutile, and quartz. During irradiation of A02, the sample was additionally heated to about 430°C . Important ion parameters are given such as accelerator energy (E_{acc}), energy at the sample site (E_{sam}), energy loss (dE/dx) and fluence.

Sample Nº	Ion	Pressure [GPa]	E_{acc} [GeV]	E_{sam} [GeV]	dE/dx [keV/nm]	Fluence [cm $^{-2}$]
A01	^{238}U	ambient	47.0	15.5	17.5	2×10^9
A02	^{238}U	≈ 1	47.0	15.5	17.5	2×10^9
Z01	^{238}U	14,2	50.3	13.8	24.5	2×10^9
R01	^{238}U	10.1	50.3	13.8	23.5	2×10^9
Q01	^{238}U	5.1	47.0	15.5	15.0	2×10^9

except that the DAC of sample A02 was heated during the irradiation. Figure 3.4.6 shows the energy-loss vs. energy diagrams - calculated with the SRIM00 code. All irradiation parameters are summarized in Table 3.4.3. The irradiated samples were returned to Tübingen, the pressure was checked again for zircon, rutile, and quartz, and then all samples were dismounted. They were all investigated by means of Raman spectroscopy in Tübingen and TEM at the BGI in Bayreuth.

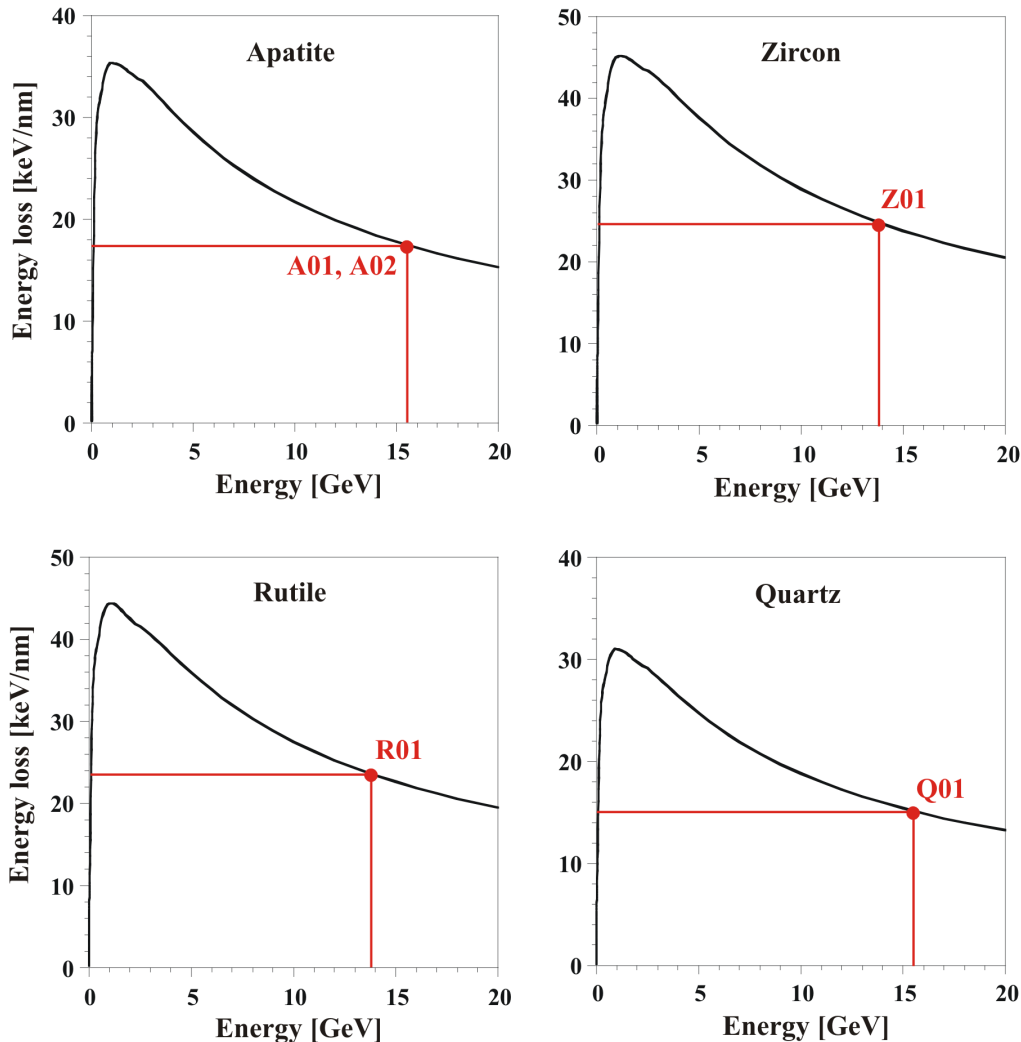


Figure 3.4.6: Energy loss vs. energy graphs for zircon, rutile, quartz, and apatite irradiations calculated with the SRIM00 code. The energy losses for the samples were selected, and the corresponding energy at the sample E_{sam} could be extracted. All numbers are given in Table 3.4.3.

Chapter 4

Results and discussion

4.1 Energy deposition of heavy ions in natural diamond

Before the ions reached the diamond, the initial SIS beam energy of 50.3 GeV was reduced by the detector foils, the beamline exit window, and the air gap (Figure 3.3.1). In chapter 2.1, there was already mentioned that the SRIM code allows us to calculate the energy loss value dE/dx for a given target at a certain ion energy E . If the thickness of this target is known, the remaining ion energy after the complete passage can also be deduced. These calculations of energy loss and range were performed separately for each segment of the setup, the results being summarized in Table 4.1.1.

There are several different codes available for such calculations; we compared two versions of the SRIM code (SRIM00 [ZB99a], SRIM03 [ZB99b]), and the ATIMA [Sch94, Wei01] code , and found agreement within less than 5%. In the following, we consider a reduction of the primary beam energy of 2.7 GeV by the Ti foils of the SEETRAM detector, the Al-exit window, and the air gap . Based on our experience from previous studies, we assume an uncertainty of the SRIM code in the order of 15%. Taking this into account for each of the segments, the error sums up to 0.4 GeV . Hence, the energy of the beam before entering the diamond anvil is $(47.6 \pm 0.4)\text{ GeV}$.

After etching, one of the $10\text{-}\mu\text{m}$ thick calibration foils in front of the diamond had a pore density of $(6.2 \pm 0.3) \times 10^8\text{ cm}^{-2}$. The same value was found in the (randomly chosen) third detector foil of the stack behind the diamond. From this agreement, we conclude that the sample alignment was sufficiently precise. Obviously, the beam penetrated the diamond and passed through the mask aperture without noticeable loss of projectiles.

Table 4.1.1: Entrance energy E_{in} and exit energy E_{out} of the ^{238}U ions for the different media (kinds of matter) of the experimental setup, as calculated with the SRIM00, SRIM03, and ATIMA codes. The energy values are given in GeV.

	Thickness [mm]	SRIM00		SRIM03		ATIMA	
		E_{in}	E_{out}	E_{in}	E_{out}	E_{in}	E_{out}
Detector (Ti)	0.03	50.3	50.0	50.3	50.0	50.3	50.0
Window (Al)	0.1	50.0	49.2	50.0	49.3	50.0	49.2
Air gap	450	49.2	47.6	49.3	47.7	49.2	47.4

For the range measurement, more than 20 PC foils selected from different positions in the stack were evaluated by track etching. The track density and thus the ion fluence was determined as a function of penetration depth in the stack. The evolution of this dependency is represented by a number-distance curve, as qualitatively displayed in Figure 4.1.1.

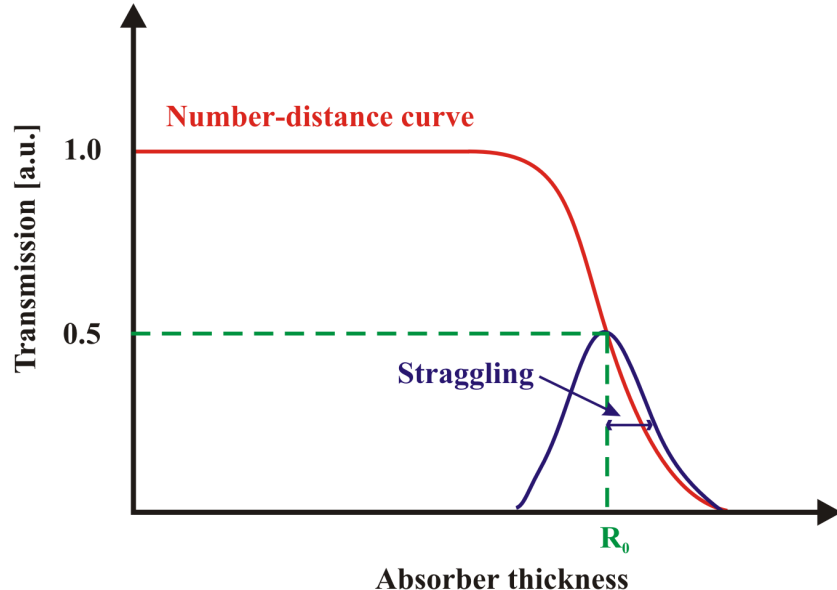


Figure 4.1.1: Qualitative evolution of number-distance curve. Due to stochastic fluctuations of the energy-loss process, the ion range exhibits a Gaussian distribution (straggling). This results in a sigmoidal decrease of the number-distance curve. The mean ion range R_0 is defined as the penetration depth into an absorber where the ion fluence drops to 50%, corresponding to the point of inflection.

Due to stochastic fluctuations of the energy-loss process, the ion range exhibited a Gaussian distribution. This results in a sigmoidal decrease of the ion fluence as a function of penetration depth. Figure 4.1.2 shows the experimentally determined number-distance curve of the ions penetrating the foil stack after the complete passage of the diamond sample. The point of inflection of the sigmoidal decrease of track density (located at 50% of initial density), gives a mean ion range of $R_0 = (1072 \pm 5) \mu m$. According to SRIM00, such a range in Makrofol (density $1.20 g/cm^3$) corresponds to a total energy deposition of $(12.4 \pm 1.9) GeV$. We regard the SRIM00 calculation for the PC target as reliable within 10-15% because the code is, beside previous studies by us, also based on a large polymer data set [GBH⁺87, SS95]. In contrast to this, no energy-loss or range measurements have been performed to our knowledge in thick diamond targets. Subtracting the energy loss in the polymer stack from $(47.6 \pm 0.4) GeV$ results in a total energy deposition in the diamond of $(35.2 \pm 1.9) GeV$.

We now calculated the energy loss of uranium ions of primary energy $47.6 GeV$ in natural diamond (density $3.52 g/cm^3$) of thickness $2.27 mm$ again with SRIM00, SRIM03, and ATIMA. These numbers together with the value deduced with the help of the foil stack

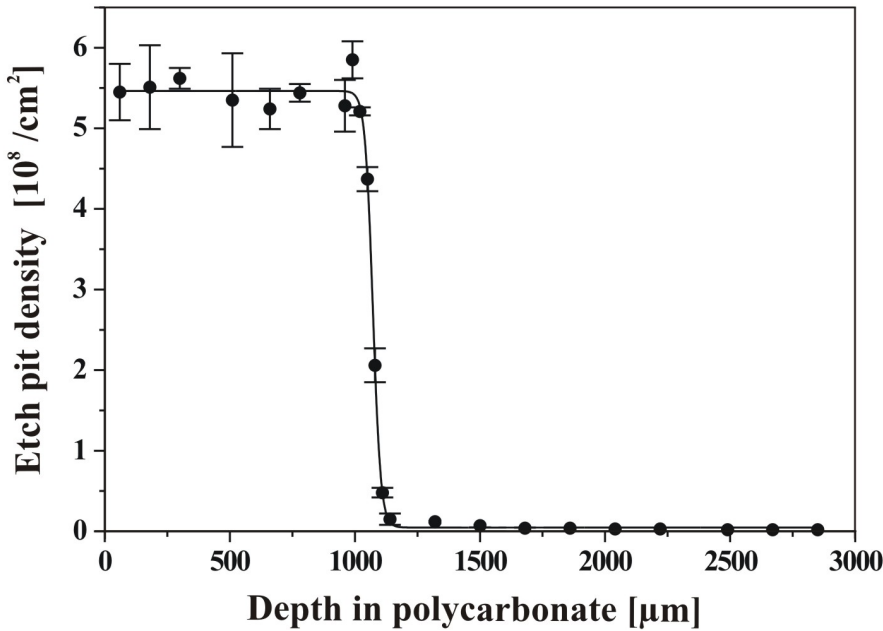


Figure 4.1.2: Areal density of etched tracks in PC foils as a function of penetration depth in the foil stack. The error bars represent 1σ of the mean areal density. The line corresponds to a sigmoidal fit through the data points. The average ion range, being defined by the point of inflection, amounts to $R_0 = 1072(5) \mu m$ (see also Figure 4.1.3).

are summarized in Table. 4.1.2. The uncertainty in localizing the ion range within the foil stack is negligible in comparison to the 15% error attributed to the SRIM code. Since the values are in reasonable mutual agreement, we consider each of these codes to be suitable for high-pressure irradiation experiments. We conclude that the energy loss within the sample, pressurized between the two diamond anvils, can be adjusted reliably. This is particularly important if highest energy-loss values are required and, for this purpose, the maximum of the energy-loss curve (Bragg peak, see Figure 2.1.1) should be positioned inside the sample.

Table 4.1.2: Energy deposition in a 2.27-mm thick diamond: Experimental data from etched foil stack and values deduced from SRIM and ATIMA calculations. All values are given in GeV.

	Foil stack	SRIM00	SRIM03	ATIMA
E_{in}	47.6	47.6	47.7	47.4
E_{out}	12.4	13.5	15.9	15.6
$E = E_{in} - E_{out}$	35.2	33.8	31.8	31.8
ΔE	1.9	5.1	4.8	4.8

The experimental range straggling is deduced from the smooth sigmoidal transition from

100 to a few percent of the initial ion fluence (Figure 4.1.3).

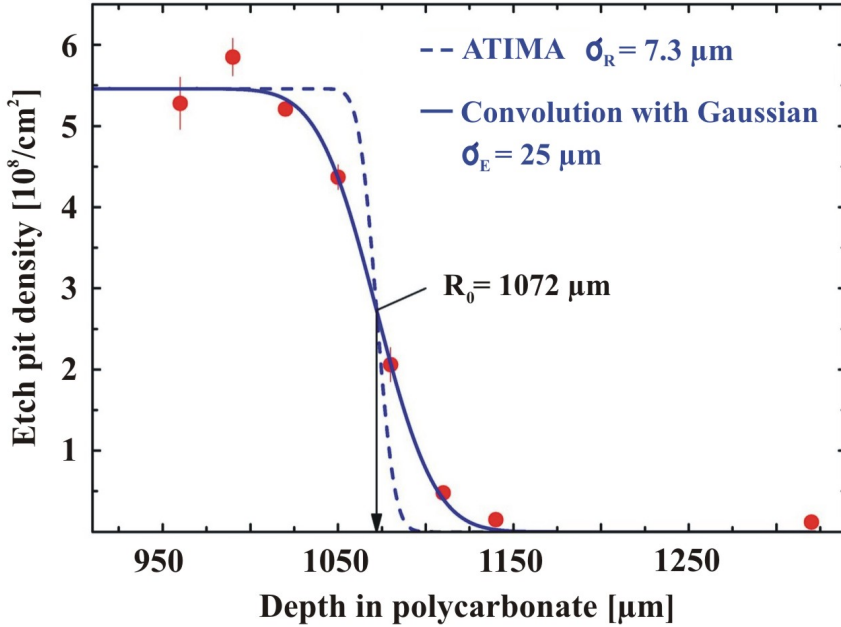


Figure 4.1.3: Etch pit density close to the depth where U ions of 50.3 GeV came to rest in the stack of polycarbonate foils. The measured width $\sigma \approx 27 \mu\text{m}$ of the range distribution can be well reproduced by a convolution (solid line) of the calculated straggling width (dashed line) with a Gaussian (not shown here) corresponding to an energy uncertainty $\Delta E/E = 2 \times 10^{-3}$ of the primary ion beam.

The data points are well described by a complementary error function, $\text{erfc}(x)$, being the integral of a Gauss curve [AS72]:

$$\Phi(x) = \frac{1}{2} \text{erfc} \left(\frac{x - x_0}{\sqrt{2} \cdot \sigma} \right) \quad \text{with} \quad \text{erfc}(x) = \frac{2}{\sqrt{\pi}} \int_{\pi}^{\infty} e^{-t^2} dt, \quad (4.1)$$

where $\Phi(x)$ denotes the ion fluence at a depth x in the foil stack, x_0 represents the projected ion range, and σ is the width of the track-density decrease (range straggling). Fitting equation 4.1 to our 47.6-GeV uranium data yields a range straggling of $\sigma \approx 27 \mu\text{m}$. In contrast to this result, calculations with the ATIMA code, assuming a monoenergetic primary ion beam, give a straggling of $\sigma_R = 7.3 \mu\text{m}$, almost a factor of four smaller than the experimental value. Additionally, we simulated the straggling process of 2500 ions with the Monte-Carlo mode of the SRIM00 code, resulting in a mean $\sigma_R = 10.5 \mu\text{m}$.

We tested a possible influence of the 30- μm thickness of the polycarbonate foils as shortest experimental ion path units, by binning the ATIMA values into 30- μm intervals. However, this procedure increased the straggling only insignificantly to $\sigma_R \approx 8 \mu\text{m}$. We conclude that the main contribution to the large experimental straggling is the energy spread ΔE of the initial ion beam after leaving the SIS, being typically $\Delta E/E = 2 \times 10^{-3}$,

resulting in a range spread of $\sigma_{\Delta E} = 25 \mu m$, thus explaining the discrepancy between the ATIMA curve and the experiment. As illustrated in Figure 4.1.3, convoluting the ATIMA curve (dashed line) with a Gaussian of $\sigma_E = 25 \mu m$ (not shown) results in a curve (solid line) that reproduces well the measured data points.

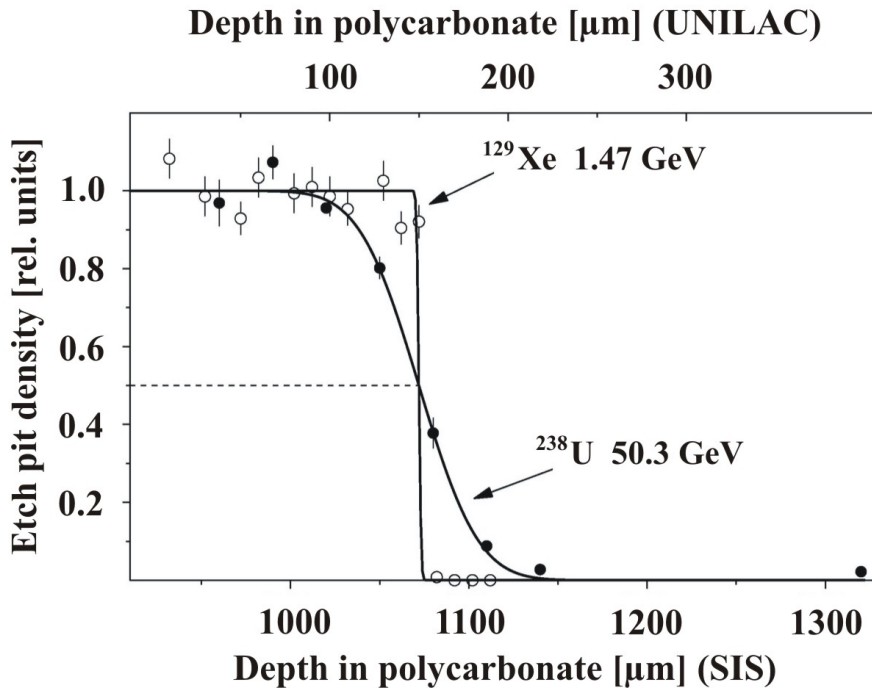


Figure 4.1.4: Etched-track density in PC foil stack vs. penetration depth. The SIS irradiation is compared with an irradiation performed at the UNILAC. The energy uncertainty of the SIS beam is reflected in a broader decrease of the etch pit density.

As an additional cross-check, we performed a similar ion-range study at the UNILAC by exposing a PC foil stack to xenon ions of only 1.47 GeV total energy at the beamline of X0, corresponding to a range of $156 \mu\text{m}$ (SRIM00). Since energy and energy spread of the beam were both much lower, the range straggling is in fact significantly smaller than at SIS energies (Figure 4.1.4).

Finally, we have to discuss fragmentation processes. In fact, fragmentation of heavy ions plays a minor role for energies up to about 200 MeV/u. An estimate of the total reaction cross section was performed with the Kox program, by taking into account the fragmentation cross section of 47.6-GeV uranium ions in 2.27 mm of diamond. About 87% of the initial ions reach the foil stack behind the diamond, hence, only a small amount of lighter particles is produced through fragmentation. We noticed a small number of etch pits even at large penetration depth originating from such light fragments with larger ranges (see non-zero tail in Figure 4.1.2)

4.2 Irradiation of phlogopite

4.2.1 Ambient-pressure irradiations

Figure 4.2.1 displays four SEM micrographs of ion-irradiated phlogopite samples after etching (sample 1, 5, 6 and 7), ordered according to decreasing energy loss.

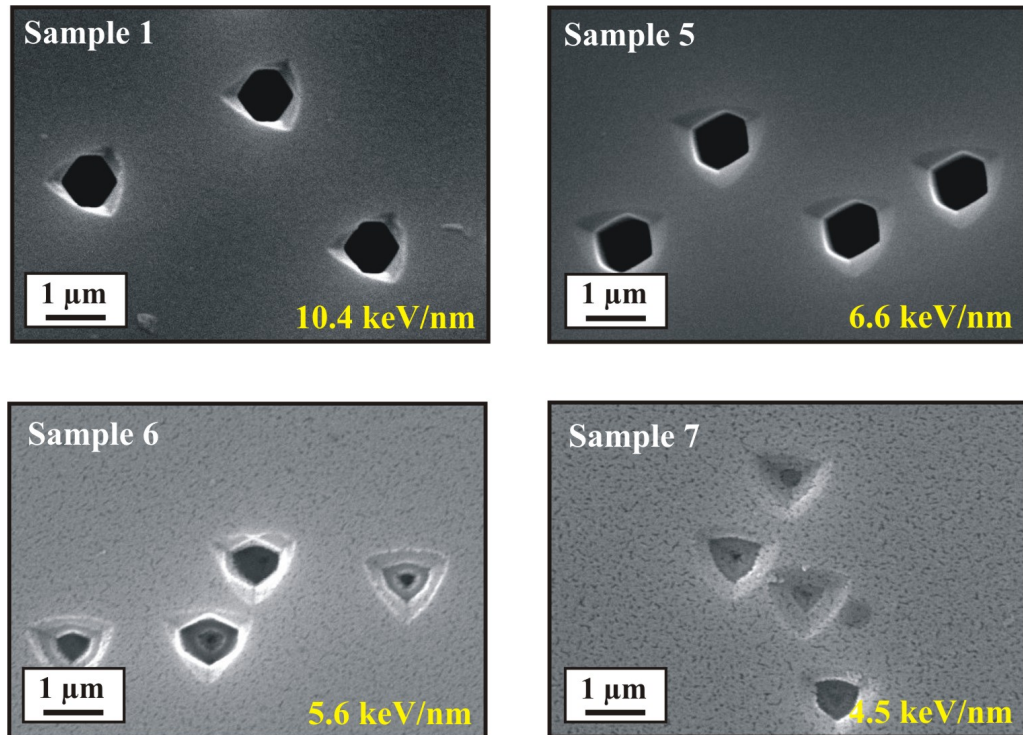


Figure 4.2.1: SEM micrographs of phlogopite samples 1, 5, 6, and 7 after 10 min etching in 4% HF (irradiation parameter see Table 3.3.1). Between energy losses of 6.6 and 5.6 keV/nm, a transition of etch-pit shape occurs.

Samples 1 and 5 show hexagonal etch pits with an outer shallow triangular geometry, whereas the etch pits of samples 6 and 7 are dominated by the triangular shape. The change in etch-pit shape takes place between the energy loss of 6.6 keV/nm and 5.6 keV/nm. This critical dE/dx of the shape transition is in good agreement with previous findings [HN98, LGM⁺02a], and a more precised value of (6.1 ± 0.5) keV/nm can now been given.

Beside this transition, another structural change of etch pits of different samples can be identified in Figure 4.2.1. The pits of samples 6 and 7 show a terraced shape, sample 7 with less steps within a given pit. We conclude from these findings that the ion tracks become increasingly discontinuous with decreasing energy loss. This result is strengthened with the help of Figure 4.2.2 showing SFM micrographs of the samples 5 and 6 with only slightly different dE/dx after 3 min of etching in 4% HF.

The hexagonal etch pits of sample 5 (Figure 4.2.2, b) are homogeneous in depth, as

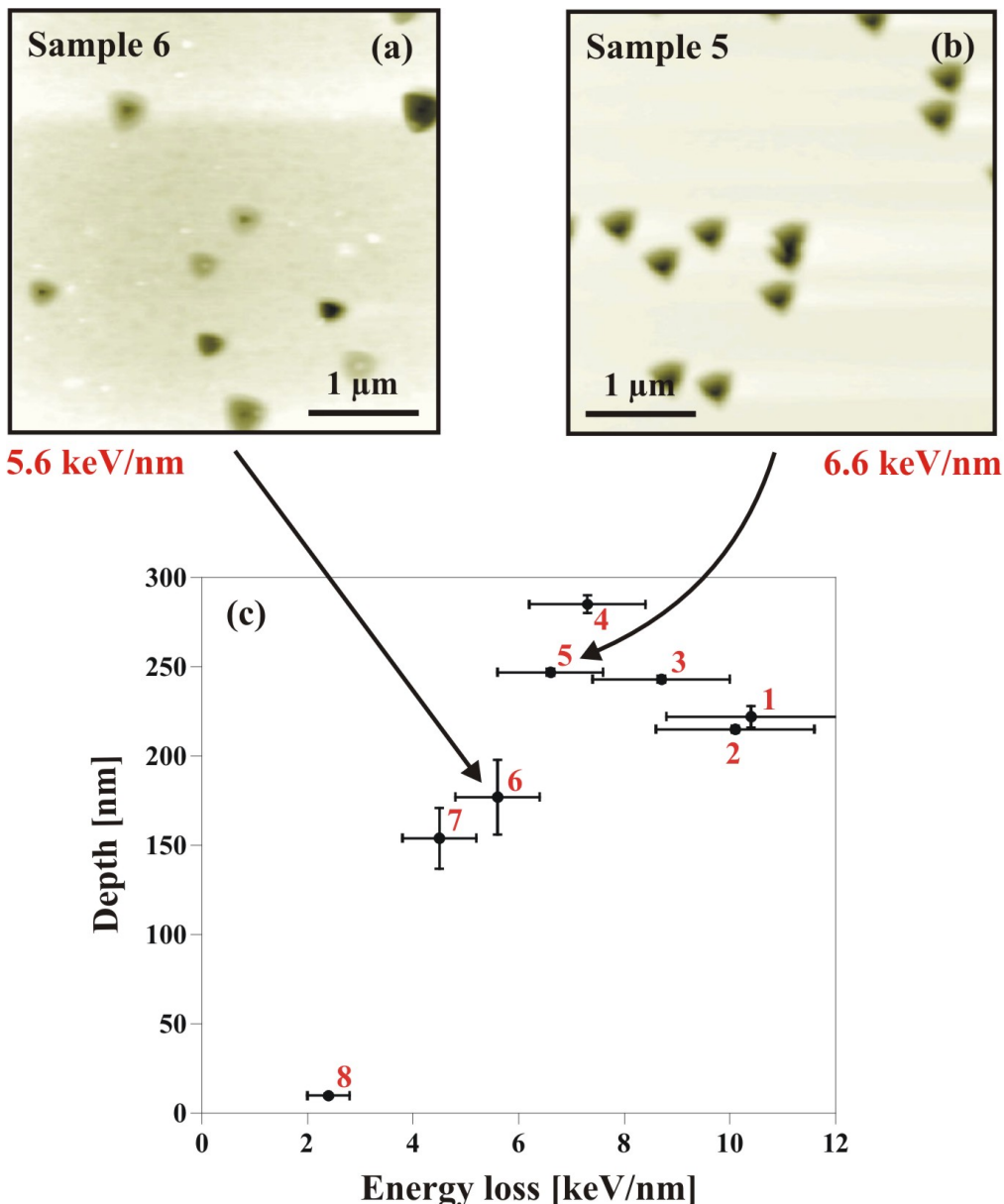


Figure 4.2.2: SFM micrographs of phlogopite samples 6 (a) and 5 (b) after 3 min etching with 4% HF, and depths of etch pits (c) for all samples 1-8 as a function of energy loss. Between the energy losses of 6.6 and 5.6 keV/nm a change from continuous to discontinuous track structure takes place. The x and y error bars represent 15% and the 1σ uncertainty of the SRIM00 code, respectively.

indicated by similar gray values, whereas the triangular pits of sample 6 (Figure 4.2.2, a) show a broader depth distribution and, furthermore, a terraced shape. Figure 4.2.2 (c) displays the etch pit depths for all samples (1-8). For high-energy-loss values, the mean depth is about the same for samples 1 to 5, with a rather small depth distribution as expressed by small error bars. From sample 6 on, towards lower dE/dx , a strong

decrease of the mean depth can be observed together with a growing width of the depth distribution. This decrease is a signature of the reduced track etch velocity indicating the beginning of the discontinuous track structure for ions having an energy loss $< 6.6 \text{ keV/nm}$. In comparison to that, M. Toulemonde et al. [TBS94] reported a similar value of $\approx 5 \text{ keV/nm}$ for muscovite mica.

For a better understanding of why and when different etch-pit shapes may occur in phlogopite mica, a SEM image of sample 1 at a higher magnification is shown (Figure 4.2.3). As mentioned earlier, the etch pit geometry is hexagonal, surrounded by a shallow triangular depression, for an energy loss of 10.4 keV/nm . Beside the micrograph, two planes of the phlogopite lattice, superposed in the paper plane, are displayed schematically. The two different planes, depicted separately in Figure 2.3.1, are the O_B -plane (part of the tetrahedral sheet) and the O_A -plane (part of the octahedral sheet). The same structure as that of the enlarged etch pit in the SEM image can be found on the atomic scale of a combination of these two neighboring planes: a hexagonal structure embedded in a triangular one, aligned in such a way that they have no parallel sides in common. It can be seen that the hexagonal structure arises from the 6 basal oxygen anions of the SiO_4 -tetrahedron, whereas the triangular structure is built up of the apical oxygen anions and the hydroxyl group of one plane of the octahedron sheet. Due to the natural hexagonal symmetry of the O_B -plane, belonging to the tetrahedral sheet, and the natural triangular symmetry of the O_A -plane, belonging to the octahedral sheet, this conclusion seems reasonable. If an ion is traveling through the phlogopite lattice, the energy transferred to the lattice disturbs the crystal and thus creates an ion track. Which of the two shapes of etch pit appears after etching, depends on the amount of this energy. If the energy is high enough, the ions destroy locally the O_B -plane of the SiO_4 -tetrahedron by breaking the strong bonds of the oxygen anions.

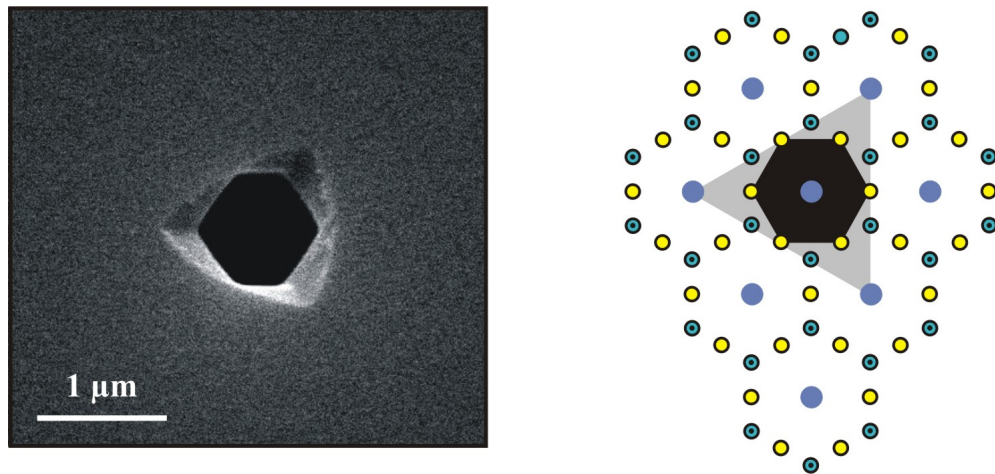


Figure 4.2.3: SEM micrograph of phlogopite sample 1 after 10 min etching with 4% HF together with apical oxygen plane (O_A -plane) and basal oxygen plane (O_B -plane) of Figure 2.3.1, both superposed in the paper plane. The hexagonal and triangular etch pits are respectively correlated with the O_B - and O_A -plane.

An appropriate etchant (in our case HF) develops this latent track and thus forms a hexagonal etch pit due to the hexagonal symmetry of this plane. For ions having a smaller energy loss, only the rather weak bonds of the apical oxygen and hydroxyl anions of the octahedral sheet can be destroyed and, with respect to the symmetry of this plane, a triangular etch pit occurs. This interpretation is supported by the fact that all continuous tracks corresponds with hexagonal etch pits, being reasonable since all SiO_4 -tetrahedron bonds must be broken along the ion trajectory in order to create a continuous track. A discontinuous track consists of a sequence of separate damage zones within an otherwise intact crystal. The mean distance between two adjacent damage zones increases with decreasing energy loss. This can be also concluded from Figure 4.2.1, as mentioned above, from a decreasing number of steps in the etch pit for the same etch conditions. Another characteristic of a discontinuous track is that the damage zones themselves are less pronounced with decreasing energy loss. This is also detectable in Figure 4.2.1, because the micrograph of sample 6 shows that in some cases the steps within a given terraced etch pit alternate between a hexagonal and a triangular form. Further, also a kind of polygonal structure is observable. Sample 7 displays only triangular forms within each terraced etch pit.

To summarize the most important points, it turned out that a shape transition of the ion-track etch pits occurs between 5.6 and 6.6 keV/nm. The change from a hexagonal to a triangular shape coincides with a transition from a continuous to a discontinuous track structure. These findings are now the base of a comparison for a high-pressure irradiation of phlogopite, presented in the next chapter.

4.2.2 High-pressure irradiations

The aim of the first high-pressure irradiation experiment with dark mica was to demonstrate, that a heavy-ion irradiation of a sample, inserted into a pressure medium and between two squeezing diamonds, is possible without pressure release and diamond damage. The fact that heavy ions reached the sample under investigation can be verified by detecting etched tracks with SFM. First results were obtained for sample P01 exposed to an uranium ion beam under 2.2 GPa. As a second step, possible effects of the parameter pressure on the ion-track formation were tested for phlogopite (P04, P05, P07, and P08). Finally, a sample was irradiated at a pressure possibly beyond the stability field of phlogopite (P06). The phlogopite experiments were completed by the high-fluence irradiation of P02 and P03 for TEM investigations on latent ion tracks. Prior to the description of the irradiations of phlogopite specimens, the results of etching of the calibration foils are briefly presented. These results are the base for further interpretations concerning track formation mechanisms at high pressure irradiations.

Fluence test with calibration foils

Figure 4.2.4 displays a typical SFM micrograph of an etched polycarbonate foil (CF01). The etch pits manifest themselves as circular regions with dark gray values.

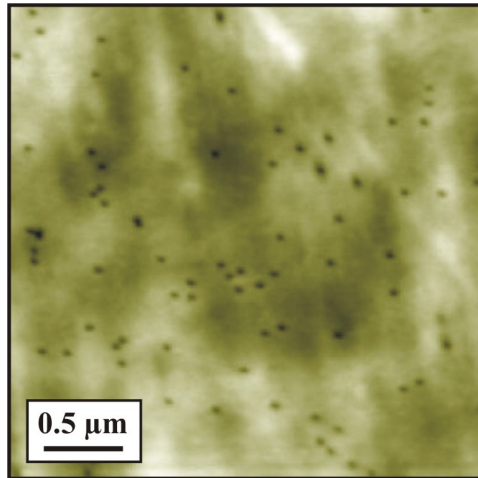


Figure 4.2.4: Micrograph of polycarbonate calibration foil after etching in 6 N NaOH at 50°C. The SFM micrograph of foil CF01 was taken after 3 min of etching. The etch pit density is about $1.4 \times 10^9 \text{ pits/cm}^2$.

The calibration foils were mounted outside the DAC, and hence the energy of the ion beam was significant larger than at the sample where the ions had completely passed one of the diamond anvils. However, even at an energy as high as 43.8 GeV, used for CF01, the etched tracks in the polycarbonate foil are homogenous in diameter and depth. By counting pits for several images, taken in a region corresponding to the sample location, the ion fluence could be extracted. Table 4.2.1 summarizes the etch results of all calibration foils. The mean etch pit densities with error bars are considered to represent the ion fluence at the sample site. Note that e.g. calibration foil CF01 corresponds to phlogopite sample P01.

Table 4.2.1: Summary of results on calibration foil investigation. The foil number corresponds to the sample number, e.g., CF01 was mounted on the DAC of phlogopite sample P01. The error of fluence represents 1σ . The ion energy at the point of the calibration foil is given by E_{Foil} .

Foil Nº	Ion	Energy E_{Foil} [GeV]	Etching time [min]	Fluence [cm ⁻²]	Foil analysis
CF01	²³⁸ U	43.8	3	$(1.4 \pm 0.6)10^9$	SFM
CF04	¹²⁴ Xe	19.6	35	$(1.6 \pm 0.4)10^7$	SEM
CF05	¹²⁴ Xe	19.6	35	$(3.2 \pm 0.1)10^6$	SEM
CF06	¹²⁴ Xe	19.6	35	$(1.5 \pm 0.2)10^7$	SEM
CF07	¹²⁴ Xe	14.9	—	—	—
CF08	¹²⁴ Xe	24.8	30	$(5.2 \pm 1.0)10^8$	SEM

In most high-pressure irradiation experiments, phlogopite samples and HOPG were irradiated in the same beamtime. Since a high fluence ($\approx 10^{11} \text{ ions/cm}^2$) was desired in the case of graphite, all irradiations in this experimental run, including the phlogopite

samples, were conducted in a focused-ion-beam mode (see chapter 2.2). In contrast to beam scanning, the ion fluence is not homogeneously distributed over the whole beam spot, but can deviate also locally on a small scale. This can be seen in Table 4.2.1 for some foils, the mean etch-pit density having a rather large error, because in these cases the numbers of etch pits were quite different for different micrographs.

In one case (foil CF01), the etch pit density of 25 different test areas was recorded with SFM, in order to receive information on the fluence distribution within the beam spot.

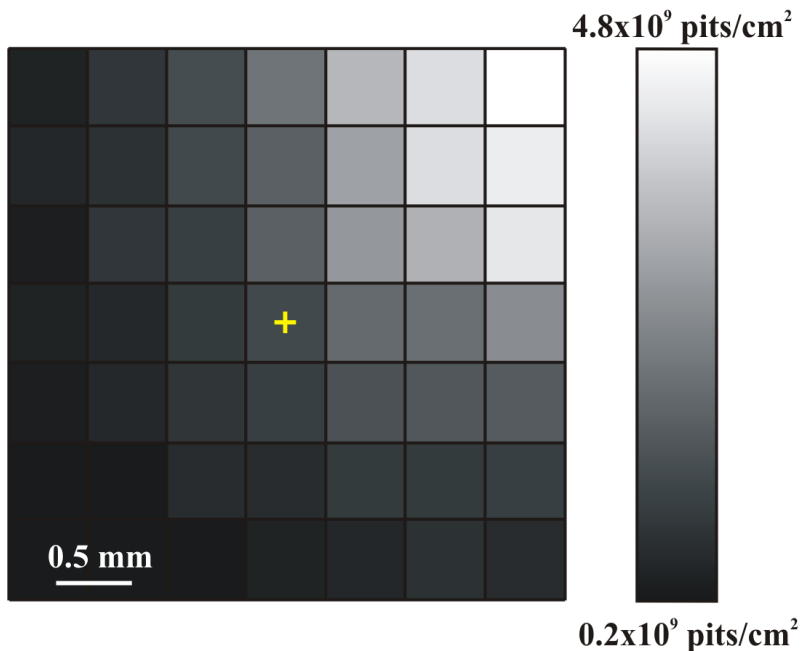


Figure 4.2.5: Scheme of results on SFM raster scan over a larger area of $3 \times 3 \text{ mm}^2$ on calibration foil CF01 after 3 minutes of etching in 6 N NaOH at 50°C . In 25 of the squares of $0.5 \times 0.5 \text{ mm}^2$, one micrograph was taken and the etch pit density was converted into a gray value and afterwards interpolated. The cross in the center represents the sample region on the foil. A strong decrease of the density can be observed from the right upper corner to the left lower corner, which means that the ion fluence was inhomogeneously distributed within the beam spot for the focused-ion-beam mode.

The results are presented in Figure 4.2.5 as a diagram in which the etch pit densities of calibration foil CP01 at different spots are represented by grey values. The maximum value of $4.8 \times 10^9 \text{ pits}/\text{cm}^2$ is located in the right upper corner of the diagram, and the fluence decreases systematically to the minimum value of $0.2 \times 10^9 \text{ pits}/\text{cm}^2$ in the lower left corner. At the sample position marked with a cross, the fluence value was intermediate resulting in $1.4 \times 10^9 \text{ pits}/\text{cm}^2$. Due to this large fluence variation within a small distance on the foil in the focused ion beam mode, a small slip of the foil during the marking process or during the foil investigation with SFM and SEM can lead to a wrong etch pit density and thus to a wrong estimation of the ion fluence on the sample. This was

especially the case for the xenon irradiations. Furthermore, a possible missalignment of the DAC itself can lead to a deviation of the fluence applied to the sample in comparison to the irradiation fluence. From this, the conclusion can be drawn that an irradiation in the scanning beam mode is preferable, because even though the ion distribution is inhomogeneous within the spot, this will be smeared out during scanning and results in an homogenous ion distribution over a larger area. However, due to the ion flux available at the SIS, very high fluences can only be reached in the focused-ion-beam mode.

First results of heavy-ion irradiation of phlogopite under high pressure

With sample P01, the first DAC was exposed to an ion beam. During the irradiation experiment, intense photoluminescence of the diamond anvils was observed. However, no indication of radiation damage was found in the diamonds after irradiation, and the pressure inside the cell after the experiment was nearly identical to the pressure before irradiation. This was also the case for all other irradiation experiments (even at the highest fluences up to $10^{11} \text{ ions/cm}^2$ in the HOPG irradiation experiments).

After dismount, P01 was etched for 1 min in 4% HF and subsequently inspected with SFM. The results are displayed in Figure 4.2.6. The etch pits imaged by SFM show clearly that the heavy-ion irradiation of a phlogopite specimen, inserted into a DAC and set under a hydrostatic pressure of 2.2 GPa , was successful. The ions penetrated one of the squeezing diamonds, the pressure medium and subsequently the phlogopite specimen. The mean etch-pit density resulting from 10 SFM micrographs amounts to $(0.7 \pm 0.1) \times 10^9 \text{ pits/cm}^2$ which is, within the error bars, in agreement with the results of calibration foil CF01 (Table 4.2.1). Obviously, all ions penetrated the diamond anvil and created an etchable damage in the sample. This is supported by the homogeneous appearance of the etch pits, which is similar to that of etch pits recorded in the preexperiment above the threshold of continuous track creation (see Figure 4.2.2). By chance, a step could be imaged, and a view along some etched tracks illustrates the homogeneity of the etching process and hence the continuity of the latent damage trail.

The SFM images demonstrate also that the etching method using a squirt was successful. Even though the etch products were not carried away during the etch process with a stirrer, only a moderate amount of residues remained on the etched surface, sometimes visible as small bright hillocks. These products are salts of the etching process in some cases grown in the shape of cubic crystals as demonstrated in Figure 4.2.7.

Pressure dependence of ion-track formation in phlogopite up to 3.2 GPa

The results of the preexperiment, described in the previous chapter, show a very sharp transition of the etch pit geometry from triangular to hexagonal symmetry, which coincides with a change from a discontinuous to a continuous track structure. We used this transition regime between 5.6 and 6.6 keV/nm as a probe for the DAC irradiations in order to test the influence of the pressure on the track formation process. One can think of three possible scenarios: Pressure (1) hinders, (2) enhances, (3) has no influence on ion track formation. If (1) holds, an irradiation of a pressurized sample, close to but

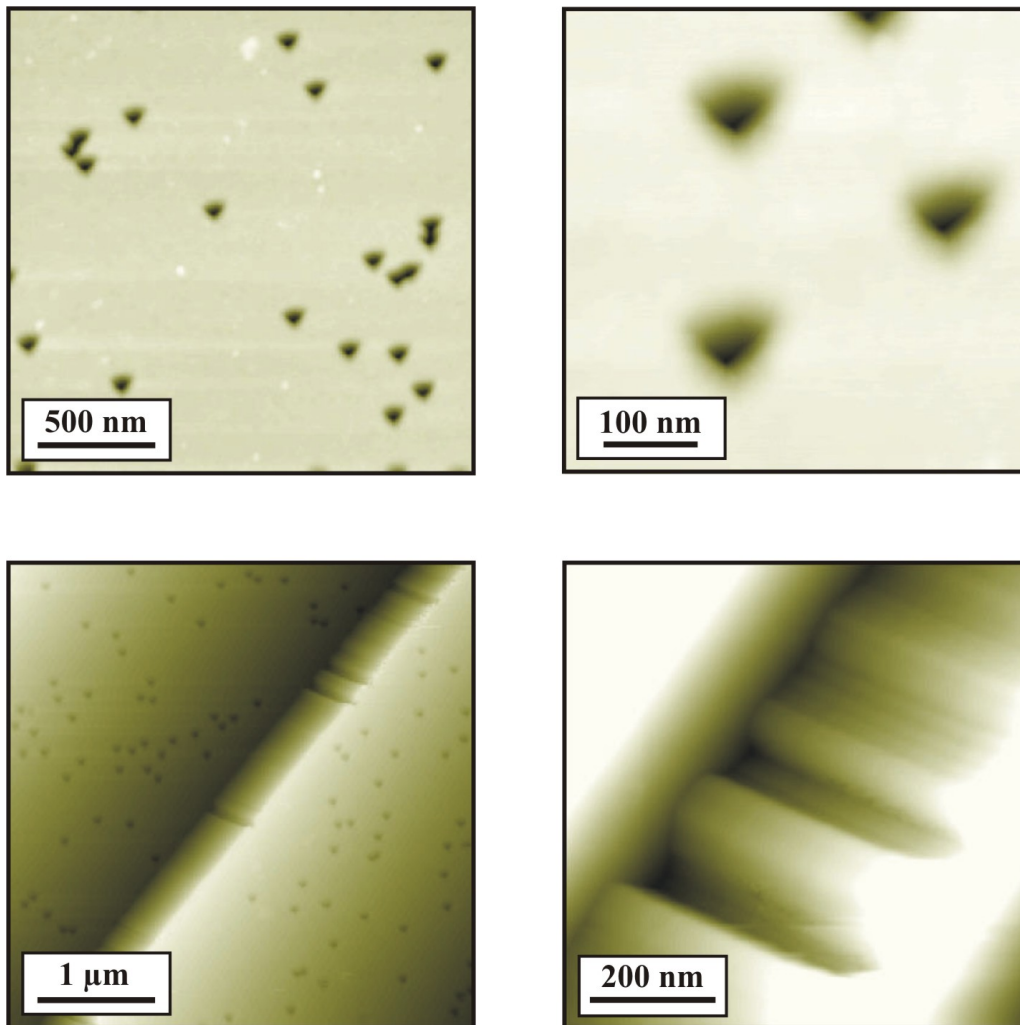


Figure 4.2.6: SFM micrographs of sample P01 after 1 minute of etching in 4% HF. The irradiation was conducted at 2.2 GPa using uranium ions of an energy loss of 16 keV/nm. The etch pits exhibit narrow depth and diameter distributions, which leads to the conclusion of a homogenous track structure. This is confirmed by the two lower images showing some etched ion tracks on a cleavage step.

above the energy loss threshold ($dE/dx > 6.6 \text{ keV}/\text{nm}$), will lead to a discontinuous instead of a continuous damage trail as expected for the sample irradiated under ambient conditions (Figure 4.2.8). This behavior would manifest itself by triangular rather than hexagonal etch pits, easily testable by SFM and SEM. Assumption (2) can be examined by irradiating a pressurized sample close to but below the critical energy loss for the shape transition ($dE/dx < 5.6 \text{ keV}/\text{nm}$).

If (2) holds, an enhanced damage creation would lead to a continuous instead of a discontinuous track, as expected for the sample irradiated under ambient conditions (Figure 4.2.8). SFM and SEM would observe hexagonal etch pits for the sample irradiated under high pressure and triangular ones after irradiation under ambient conditions. If neither

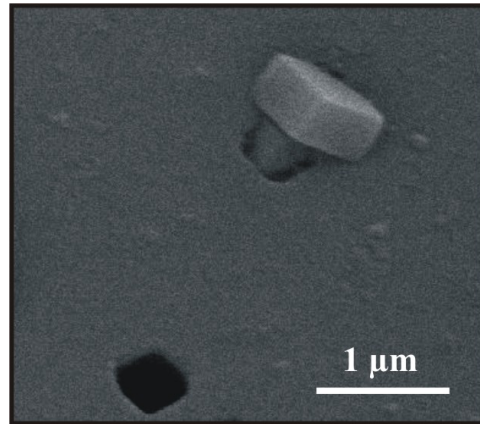


Figure 4.2.7: SEM image of a phlogopite surface after 5 minutes of etching in 4% HF at room temperature. Some salt that remained from the etching process, crystallizes with a cubic shape.

(1) nor (2) occurs, no pressure influence on the damage creation will arise, at least in the pressure regime examined by us (3).

As shown in Figure 4.2.8, two sets of samples were used for testing the influence of a pressure in the order of 3 GPa on the track formation process at energy losses close to the threshold. The samples P04 (ambient pressure) and P05 (2.6 GPa) were irradiated with xenon ions having, at the sample site, an energy loss of 8.5 keV/nm i.e. a value above the transition regime. The samples P07 (ambient pressure) and P08 (3.2 GPa) were irradiated with the same ion species of an energy loss of about 4 keV/nm , representing the irradiations below the critical threshold. The irradiation conditions can be found in Table 3.4.1. All four samples were etched for 1, 3, and 5 minutes with 4%HF at room temperature and each time inspected with SFM, the samples irradiated with ions having a higher energy loss value were additionally investigated with SEM after 5 minutes of etching. The results of the investigations on the samples P04 and P05 are illustrated in Figure 4.2.9 by two SEM micrographs.

In both cases, hexagonal etch pits are visible which are homogeneous in depth and size distribution. The mean etch pit diameter is in both cases of order $0.5\mu\text{m}$ after 5 min of etching in 4% HF. This means the pressure of 2.6 GPa applied to sample P05 does not effect changes detectable by etch pit studies. The track etch rate is hence in both samples in agreement with each other. The mean etch pit density determined from several micrographs results to $(4.3 \pm 0.5) \times 10^7\text{ pits/cm}^2$ for sample P04 and $(3.7 \pm 0.2) \times 10^7\text{ pits/cm}^2$ for sample P05. These values are significantly higher than estimated with the calibration foils CF04 and CF05 (Table 4.2.1). As mentioned above, these irradiations were conducted in the focused-ion-beam mode, where large deviations in the fluence occurred and, therefore, a small slip of the calibration foil could lead to disagreement between marked foil region and sample.

The results of SFM investigations on samples P07 and P08 after etching are displayed in Figure 4.2.10. The energy loss was about 4 keV/nm in both cases, and hence trian-

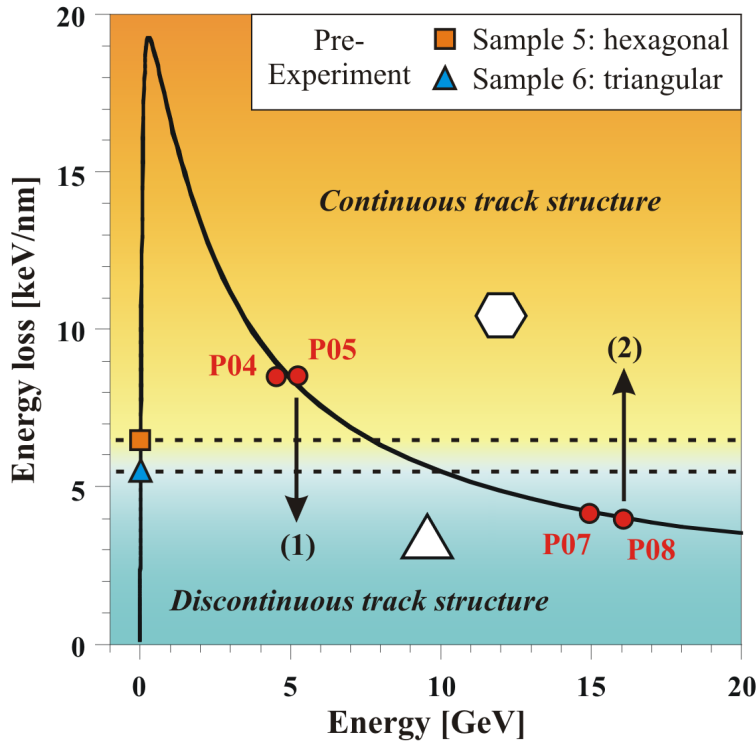


Figure 4.2.8: Energy loss of xenon ions in phlogopite as a function of the energy (solid line). The etch pits are hexagonal above 6.6 keV/nm (continuous track), and triangular below 5.6 keV/nm (discontinuous track). These borders (dashed lines) were found in the ^{58}Ni irradiation of samples 5 and 6 (preexperiment). For the high-pressure irradiations, two samples were irradiated below and two above these thresholds. A possible pressure influence on the track formation process could lead to a change of etch pit symmetry in both ways (1) and (2). More details about the samples P04, P05, P07, and P08 can be found in Table 3.4.1.

gular etch pits were expected taking into account the preexperiment. Both micrographs indicate that the etch pits are very weak and have a triangular symmetry with strongly rounded corners. It should be mentioned that in the case of the preexperiment a small energy loss value was realized by decelerating the ions to small energies with the help of degrader foils (low-energy side of the Bragg peak, solid square and triangle in Figure 4.2.8). In the case of the SIS irradiations of phlogopite specimens embedded in a DAC, it was not possible to decelerate the energetic ions, which first have to penetrate one diamond anvil completely, to such small energies at the sample site. Very small uncertainties in adjusting the ion energy could lead to complete stopping within the first diamond anvil. This could be avoided by irradiating the samples in the DAC with ions having such high energies that the energy loss value dropped to the desired value (high-energy side of the Bragg peak, solid circles in Figure 4.2.8). But due to the higher kinetic energy, the energy deposition in the solid is smeared out, and hence the radiation damage is less pronounced (velocity effect) [MBC⁺93].

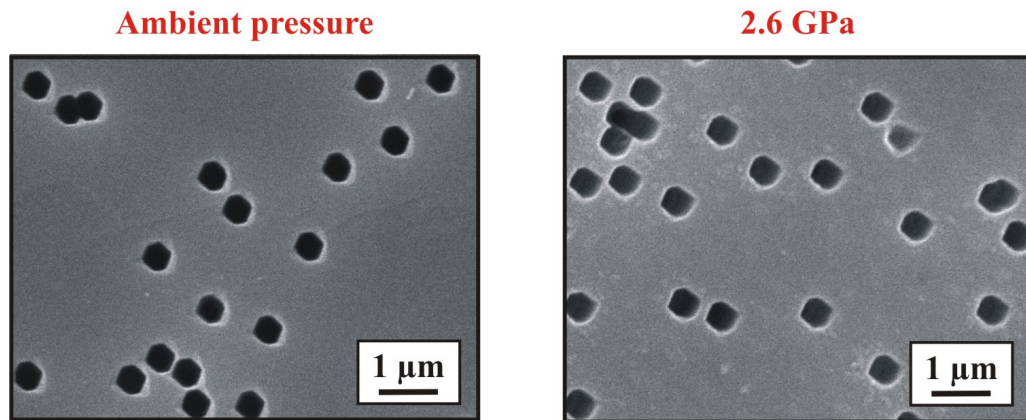


Figure 4.2.9: Two SEM micrographs of etched (5 min 4% HF) phlogopite samples displaying hexagonal etch pits. The specimens were irradiated with xenon ions of energy loss 8.5 keV/nm at ambient pressure conditions (sample P04, left picture) and 2.6 GPa (sample P05, right picture), respectively.

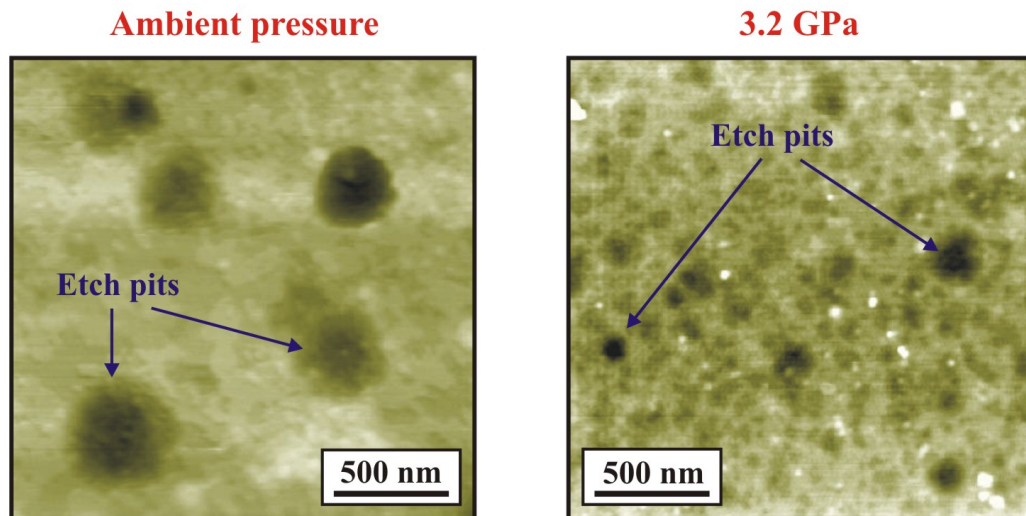


Figure 4.2.10: SFM micrographs of etched (5 min 4% HF) phlogopite samples displaying weak triangular etch pits. Both specimens were irradiated with xenon ions having an energy loss of about 4.0 keV/nm at ambient pressure conditions (sample P07, left picture) and 3.2 GPa (sample P08, right picture), respectively.

However, the appearance of the etch pits is for both samples in accordance with the preexperiment and, in particular, no hexagonal etch pits are observed in the case of P08, which was irradiated under 3.2 GPa. The etch pit density could not be reliably determined due to the weak hollows, which are hardly distinguishable from the undamaged sample surface.

To conclude this section, no influence of a pressure up to 3.2 GPa on track formation could be detected with this method.

Phlogopite irradiation at an increased pressure of 8.4 GPa

Sample P06 was set under a pressure of 8.4 GPa , the highest value of all phlogopite irradiations. The other irradiation conditions such as energy loss of the xenon ions were exactly the same as for sample P04 (ambient pressure) and P05 (2.6 GPa), as shown in Table 3.4.1. This means that P04 is also a control sample at ambient conditions for P06. A SEM micrograph of P06 after 5 minutes of etching is displayed in Figure 4.2.11. The hexagonal etch pits of P06 are very similar to those of P04 and P05 after the same etching time (see Figure 4.2.9).

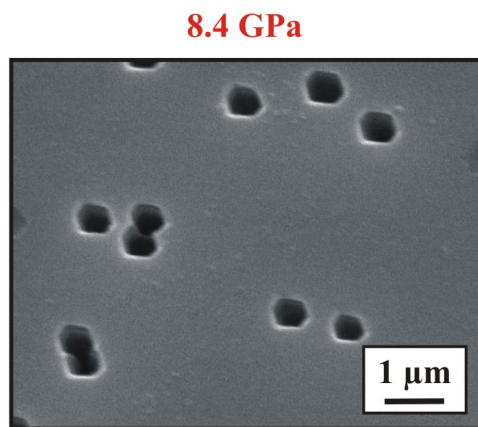


Figure 4.2.11: SEM micrograph of phlogopite sample P06 after 5 min of etching in 4% HF.

The specimen was irradiated at a pressure of 8.4 GPa with xenon ions having the same energy loss as irradiations of samples P04 and P05. No difference in etch pit appearance was found by comparing the three samples (see also Figure 4.2.9).

Again, no pressure influence can be found, even not at a value as high as 8.4 GPa . The etch pit density was determined from 6 SEM micrographs and results to $(2.5 \pm 0.6) \times 10^7 \text{ pits/cm}^2$, which is higher than expected from calibration foil CF06 (see Table 4.2.1). As for P04 and P05 the reason for this deviation being most likely the irradiation in the focused-ion-beam mode

As mentioned earlier (chapter 2.3.3), Sato and coworkers found a possible phase transition in the phlogopite system that starts at about 4.5 GPa and 1300°C [SKI97]. Figure 4.2.12 shows a simplified scheme of their phase diagram of phlogopite containing the potential phase boundary (solid line).

They report that at 8 GPa and temperatures above 1000°C there exists already a pyrope content of 30 vol.% in the phlogopite system. The trioctahedral mica used in their study had a similar chemical composition as the phlogopite used in our investigations, except a much lower titanium and iron content. Our irradiation experiment was conducted at 8.4 GPa and room temperature, and hence not in the region of the phase diagram investigated by Sato and coworkers. However, taking into account the similarity of etch pits of samples irradiated at high pressure and ambient conditions, and the strong correspondence of their shape with the crystal lattice as demonstrated in the preexperiment, the

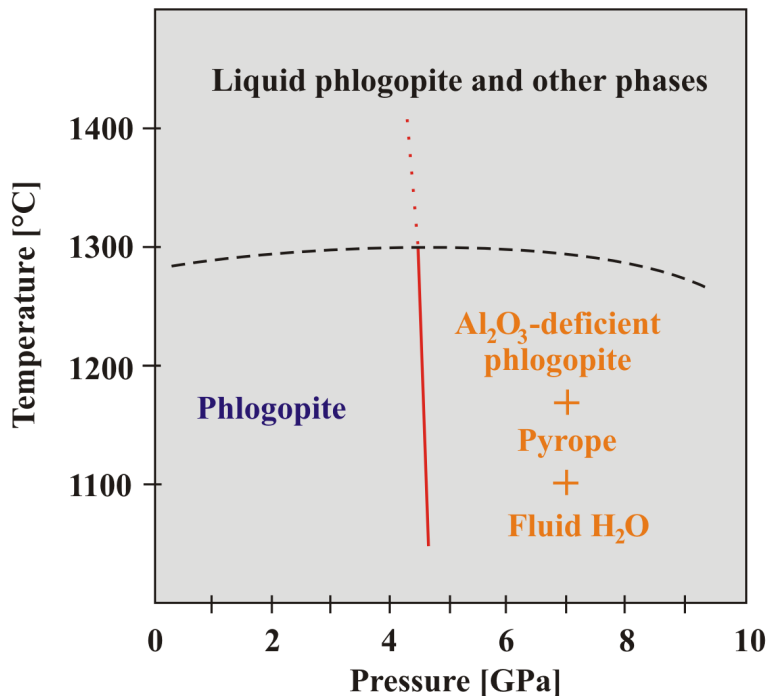


Figure 4.2.12: Simplified scheme of phase diagram of natural phlogopite after Sato et al. [SKI97]. At about 1300°C and 4.5 GPa, a phase transition occurs at which phlogopite starts to break down into pyrope $[(\text{Mg}, \text{Fe})_3\text{Al}_2\text{Si}_3\text{O}_{12}]$, Al_2O_3 -deficient phlogopite, and fluid water. Our irradiation was performed at 8.4 GPa and room temperature. No evidence of a phase transition could be observed.

conclusion can be drawn that at 8.4 GPa and room temperature phlogopite is still the dominating stable phase. A significant amount of other phases such as pyrope should have an influence on the appearance of etch pits. A possible explanation for our findings is that at ambient temperature the phase transition is thermally suppressed. But we can not exclude that due to a possible heating of the ions, pyrope was created within the ion tracks that have been etched away afterwards.

The etch experiments on phlogopite samples will be summarized by the presentation of the mean diameter and depth of the etch pits as a function of etching time and pressure. The samples P04, P05, and P06 irradiated at same energy loss but at different pressures, were used for this study. The mean diameter and depth values were determined from several SFM micrographs for each etching time (1, 3, and 5 min) as shown in Figure 4.2.13.

About 15 pits were measured in several images, and the results are summarized in Table 4.2.2 and for better illustration plotted in Figure 4.2.14. Taking into account some deviations in the etch process, the mean diameter and depth data are both comparable for a given etching time and show a similar growth rates. This means that the track etch rate, represented by the slope of the linear increase in depth and diameter as function

Table 4.2.2: Summary of etch pit investigations on samples P04, P05, and P06, which were irradiated with xenon ions having the same energy loss of 8.5 keV/nm. The mean diameter and depth of etch pits were determined from 15 pits, the error represents 1σ .

Sample N°	Pressure [GPa]	Fluence [cm^{-2}]	Etching time [min]	Diameter [nm]	Depth [nm]
P04	ambient	$(4.3 \pm 0.5)10^7$	1	(160 ± 18)	(76 ± 25)
			3	(342 ± 46)	(213 ± 55)
			5	(648 ± 55)	(331 ± 43)
P05	2.6	$(3.7 \pm 0.2)10^7$	1	(109 ± 13)	(54 ± 14)
			3	(289 ± 26)	(189 ± 40)
			5	(477 ± 56)	(378 ± 21)
P06	8.4	$(2.5 \pm 0.6)10^7$	1	(220 ± 31)	(72 ± 34)
			3	(416 ± 50)	(168 ± 29)
			5	(493 ± 40)	(295 ± 19)

of etching time, is for all three samples about the same.

TEM investigations on heavy-ion irradiated phlogopite under high pressure

The etch experiments reported in the last sections showed no influence of pressure up to 8.4 GPa on the ion track formation process in phlogopite. But it should be mentioned that the etch process, which converts the nanometer-sized latent damage into a micrometer-sized etch pit, possibly erases small effects of the pressure existing in the latent track. For this reason, TEM investigations were performed on two phlogopite specimens irradiated under exactly the same conditions, except that one sample was set under a pressure of 1.9 GPa (P03), whereas the other specimen remained under ambient conditions (P02).

During the imaging process, it turned out that phlogopite is a problematic material for TEM investigations. It exhibits the problem that the electron beam initiates the release of fluids stored between the phlogopite sheets. This made it difficult to obtain images of good contrast as visible in Figure 4.2.15. The latent ion tracks can not be clearly distinguished from the undistorted lattice. Due to that, it is not possible to compare the shape and mean size of the latent tracks for both samples. However, we note that in both cases the tracks are observable, and tracks in the sample irradiated under 1.9 GPa are rather homogenous in their appearance, supporting the assumption of continuous damage trails.

To conclude this chapter, no evidence of a pressure dependence on the ion track formation in phlogopite could be found by means of track etching. Even at the highest pressure value of 8.4 GPa, the etch pits were similar to those of the sample irradiated under ambient conditions. This is in contrast to an irradiation experiment of stressed amorphous iron-boron alloy, where the in-plane stress of the order of 2 GPa resulted in a reduced etch rate [TKT00]. We did not observe a decrease of the etch pit diameters on

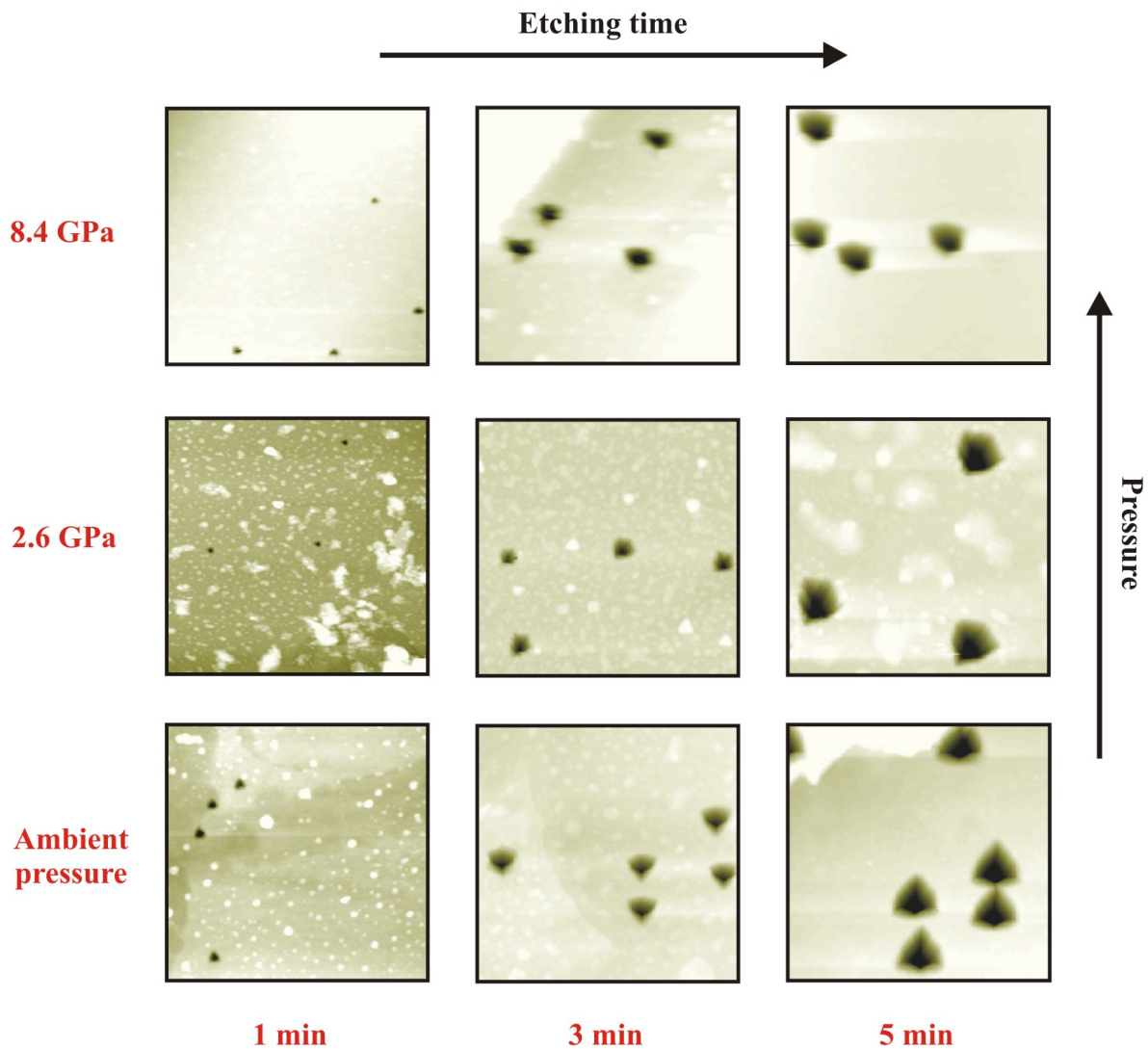


Figure 4.2.13: SFM micrographs of three phlogopite specimens irradiated with xenon ions of an energy loss of 8.5 keV/nm at ambient pressure (P04), at 2.6 GPa (P05), and at 8.4 GPa (P06). Each sample was imaged after 1, 3, and 5 minutes of etching in 4% HF. The mean etch-pit diameter and depth were determined from several such pictures, the results being displayed in Table 4.2.2 and Figure 4.2.14.

the phlogopite specimens irradiated under high pressure conditions in comparison to irradiations under ambient conditions. However, we used a crystalline material and applied a hydrostatic pressure, which means that the experimental conditions were significantly different.

Cruz presented theoretical considerations about the track formation process under high-pressure conditions [Cru04]. He predicted a significant change of the energy loss in a pressurized target during an ion irradiation, especially in the *GPa* regime. Our irra-

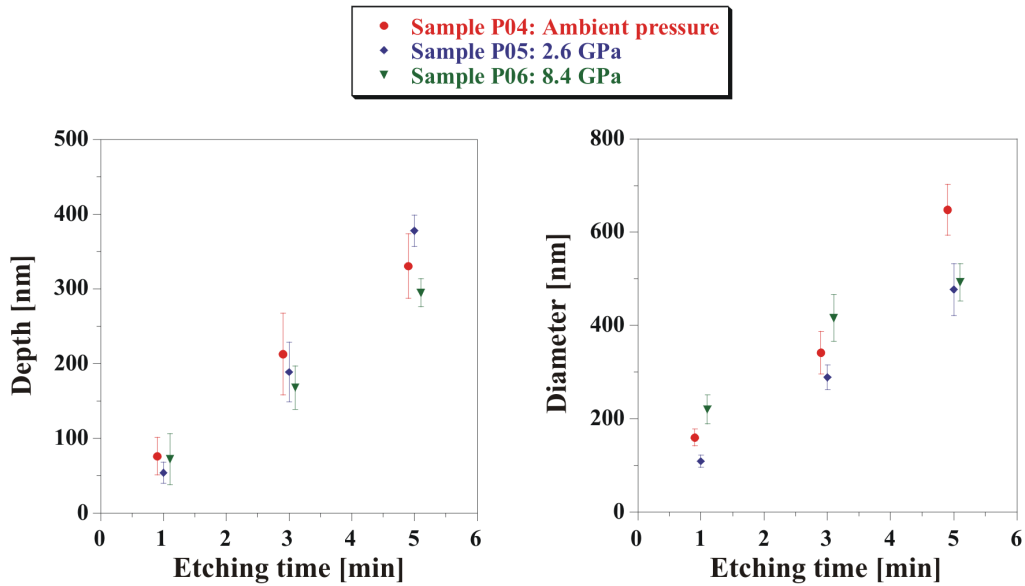


Figure 4.2.14: Mean depth and diameter of the etch pits of samples P04, P05, and P06 as a function of etching time. The mean values were determined from 15 pits, the error represents 1σ .

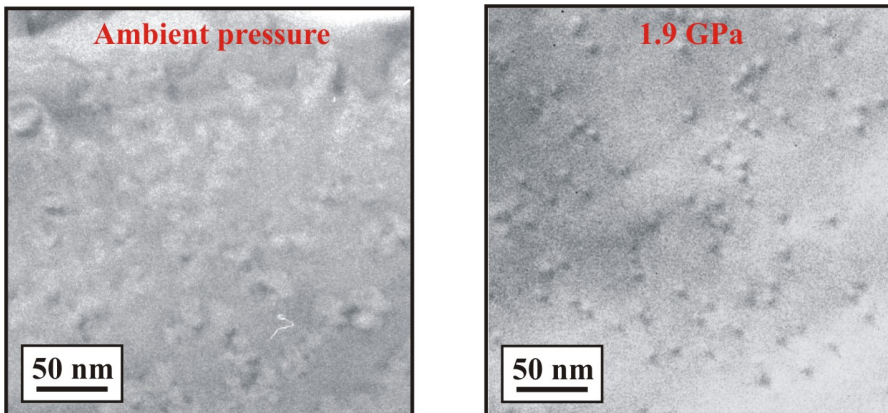


Figure 4.2.15: TEM images of phlogopite irradiated with ^{197}Au ions at ambient pressure (P02) and 1.9 GPa (P03). Ion tracks are in both cases detectable. Due to weak contrast (especially for P02), a comparison of shape and size of tracks is not possible.

diation experiments on phlogopite did not confirm this prediction, a significant change of energy loss caused by the applied pressure would have been observed in the etch pit shape.

Fission tracks in this mineral are generally used to date samples originating from areas up to 10 km below the surface corresponding to about 0.3 GPa. In regions deeper than 10 km, the temperature increase may anneal the fission tracks [GDG⁺86, WdH92]. Our experiments showed that in phlogopite the appearance of etched ion tracks is not

influenced by pressure up to 8.4 GPa for room temperature irradiations.

The layered structure of this dark mica is realized by the weak bonding of the large cations between the sheets. Exerting a high pressure to a phlogopite specimen, leads dominantly to a shortening of this interlayer thickness, whereas the lattice remains otherwise intact. We assume that this property is mainly responsible that pressure does not play a significant role for track formation. Nevertheless, we can not exclude that small variations, initiated through the pressure, occur inside the latent ion tracks.

4.3 Irradiation of graphite

Three different HOPG samples were irradiated with swift heavy ions at a pressure of 0.5 (G02), 8.4 (G03), and 12.1 GPa (G04). Figure 4.3.1 shows the phase diagram of carbon according to Bundy et al. [BBW⁺96], complemented by three dashed horizontal lines representing the three high-pressure irradiation conditions. At room temperature, the phase boundary between graphite and diamond occurs at about 2 GPa . This means that sample G02 was irradiated in the stability field of graphite (0.5 GPa). The two other experiments (G03 and G04) were conducted in the stability field of diamond. In order to have a reference sample, we additionally irradiated one sample (G01) at the beamline of X0. This specimen was directly exposed to a Au-ion beam of 2.6 GeV at ambient pressure without being enclosed in a DAC. This irradiation was therefore performed in the stability field of graphite. The irradiated samples were investigated by Raman spectroscopy and TEM, and G01 was additionally inspected by STM.

Raman spectroscopy of heavy-ion irradiated HOPG

In order to identify possible phase transformations, Raman measurements were performed on all ion-irradiated graphite samples (G01, G02, G03, and G04) as well as on pristine (non-irradiated) HOPG. The spectrum of sample G01 before and after ion irradiation is displayed in Figure 4.3.2.

At 1582 cm^{-1} , the pristine and irradiated HOPG sample exhibit the so-called G band ascribed to the crystalline graphite phase. No other bands are detectable.

Figure 4.3.3 displays the spectra of G02 and G04 irradiated at two different high-pressure conditions. Beside the graphite band, another rather broad band appears between 1300 and 1400 cm^{-1} in both spectra. Furthermore, a shoulder-like peak is observable around 1600 cm^{-1} . These bands, designated as D modes, were also found after heavy-ion irradiations at ambient conditions [LHT⁺03]. The authors report on three different defect bands at 1346 (D1), 1367 (D2), and 1622 cm^{-1} (D') appearing when the irradiation fluence surpasses a critical value that, for medium-energy-loss ions (e.g. 11 keV/nm), in the order of $10^{13} \text{ ions/cm}^2$. For high-energy-loss ions (e.g. 27 keV/nm), this so-called incubation fluence is reduced to $8 \times 10^{11} \text{ ions/cm}^2$. This explains why sample G01 irradiated with $1 \times 10^{11} \text{ ions/cm}^2$ of 27 keV/nm at ambient pressure did not exhibit any D band.

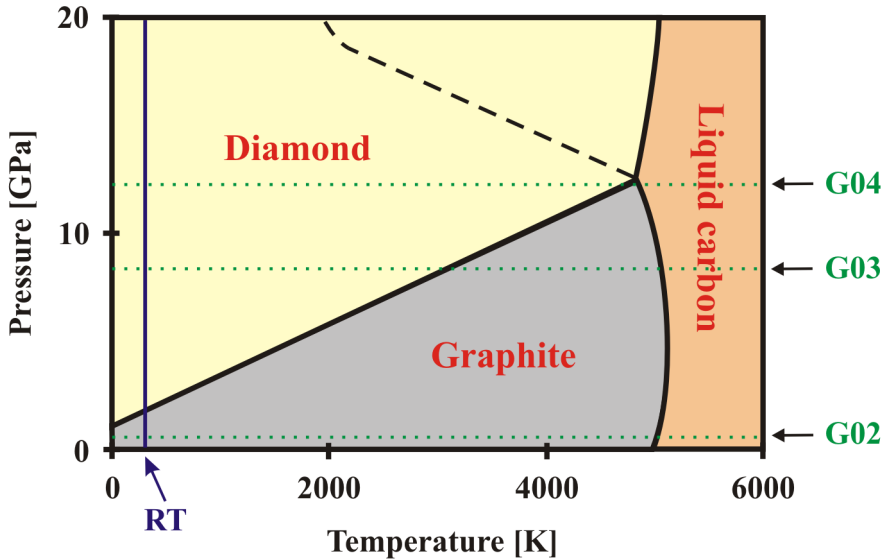


Figure 4.3.1: Phase diagram of graphite according to Bundy et al. [BBW⁺96]. The pressure conditions for all three high-pressure irradiation experiments are marked with dotted horizontal lines. At room temperature, the phase boundary of graphite and diamond is at about 2 GPa. Samples G03 and G04 were irradiated within the stability field of diamond, whereas G02 and G01 (ambient pressure, not shown) in the stability field of graphite.

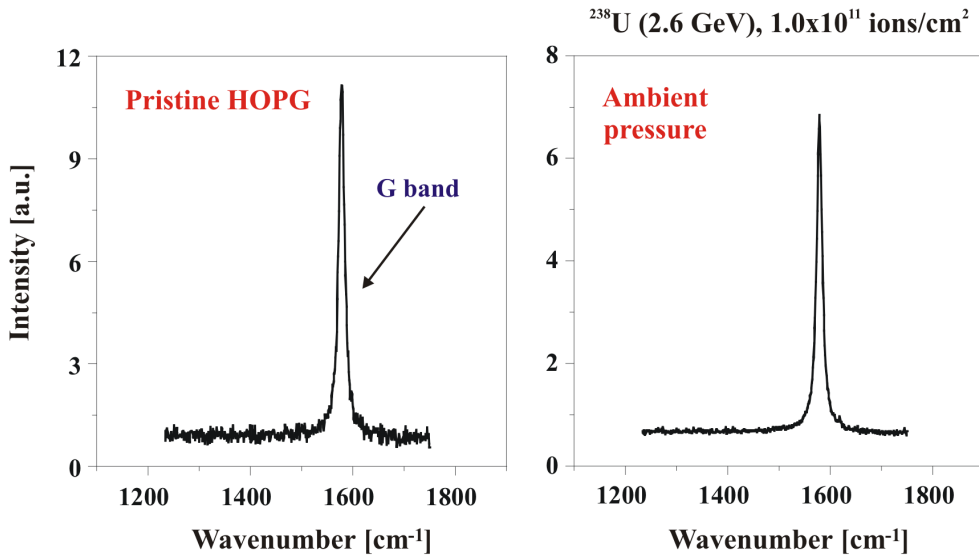


Figure 4.3.2: Raman spectrum of graphite sample G01 before (left) and after (right) irradiation with 2.6 GeV uranium ions ($1 \times 10^{11} \text{ cm}^{-2}$) at ambient pressure. No change after irradiation is observable, both spectra exhibit only the G band indicating crystalline graphite.

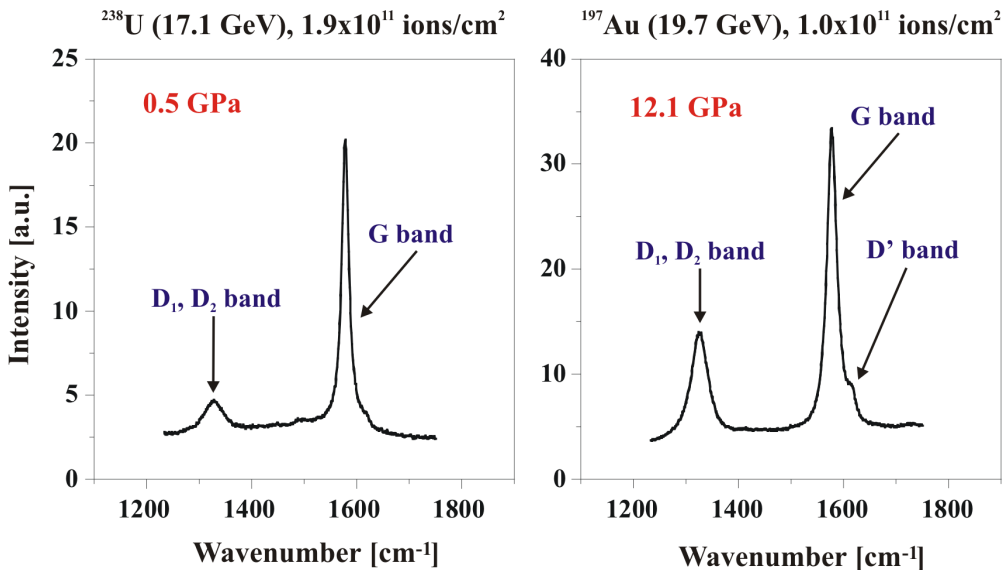


Figure 4.3.3: Raman spectrum of graphite samples G02 (left) and G04 (right) after irradiation with 1.9×10^{11} and $1.0 \times 10^{11} \text{ ions}/\text{cm}^2$, respectively. In both spectra, D bands are observable indicating the presence of disordered graphite. For the irradiation within the stability field of diamond at 12.1 GPa (right) the D bands are more pronounced in comparison to irradiations within the stability field of graphite at 0.5 GPa (left).

The D bands are an indication for disordered, non-crystalline graphite material. It is interesting to note that in the case of our high-pressure irradiations with ions of comparable medium energy loss as reported in [LHT⁺03], the defect bands appear already at a lower fluence of about $10^{11} \text{ ions}/\text{cm}^2$. The same behavior was also found for sample G03. From several Raman measurements at different sample locations, the conclusion can be drawn that disordered graphite is detectable in all samples irradiated under high pressure. It seems that the magnitude of the relative intensities of the D peaks with respect to the G peak is higher when the irradiation was performed outside the stability field of graphite as realized with G03 and G04. The intensity of the D bands varied significantly when testing different sample areas particular for G03 and G04. Obviously, the disordered graphite material is not homogeneously distributed over the whole sample. Generally, a larger amount of the non-crystalline graphite phase was found close to the sample edges. At some spots of G03, the crystalline graphite was completely converted into the non-crystalline phase, expressed in the spectrum in such a way that only the D mode was detectable and the G mode disappeared completely.

TEM investigations of heavy-ion irradiated HOPG

All HOPG samples were investigated by means of TEM. Beside imaging, also electron diffraction patterns and EELS spectra have been recorded.

As mentioned earlier, the TEM investigations were performed on wedge-shaped bound-

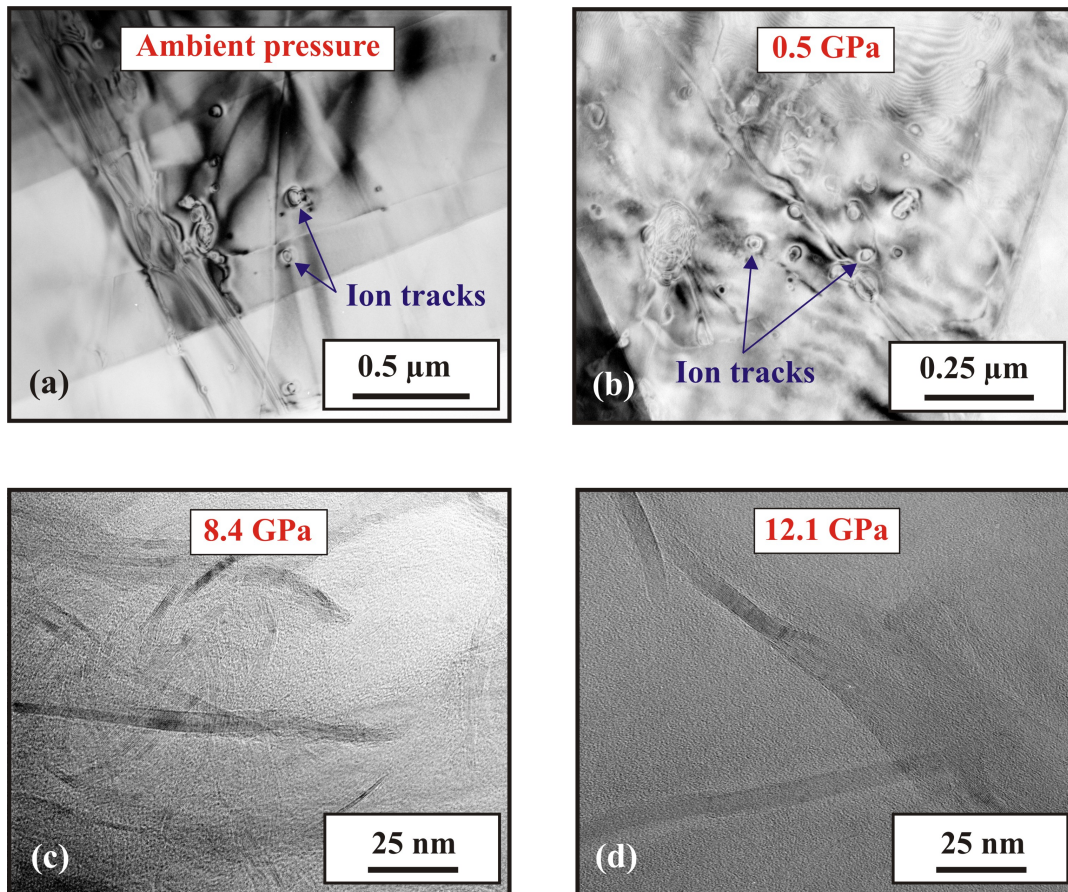


Figure 4.3.4: TEM images of HOPG samples G01 (a), G02 (b), G03 (c), and G04 (d) after heavy-ion irradiation. G01 was exposed to the ion beam at ambient pressure, whereas the other specimens were irradiated in a DAC under high-pressure conditions. Amorphous ion tracks are detectable inside the otherwise undisturbed HOPG lattice for irradiations conducted within the stability field of graphite (a,b). Large amorphous areas containing new crystals of graphite with a lattice orientation different from the original crystal are visible for irradiations performed within the stability field of diamond (c,d). All images show the (001) lattice plane of graphite, which is perpendicular to the direction of the incident ions.

ary regions of the samples where the thickness was in the order of about $50\text{-}100\text{ nm}$, which allows the complete penetration of the electron beam. Figure 4.3.4 displays a representative image of each of the four graphite samples (G01-G04). Both images of samples irradiated at ambient pressure and at 0.5 GPa (G01 and G02) show clearly defined ion tracks with an amorphous core of about 20 nm in diameter (a,b). The areal density of tracks is in both cases much lower than the fluence applied. For example, the TEM image of sample G02 irradiated under 0.5 GPa (b) shows about 20 tracks. Taking into account the fluence of $1.9 \times 10^{11}\text{ ions/cm}^2$ and the image size, about 2000 tracks should be visible if each projectile produces a track. The bulk of both samples

is perfectly crystallized and ordered. In contrast to this, graphite irradiated at 8.4 and 12.1 GPa (G03 and G04) with the same ion fluence is largely amorphous, containing some inclusions of crystalline graphite with random orientations (c,d). These graphite flakes are interconnected in the form of a turbostratic-like texture. No individual ion tracks can be detected.

Consistent results were obtained from electron diffraction patterns, two of them being depicted in Figure 4.3.5. For G01 (a) and G02 (not shown), the characteristic diffraction patterns of crystalline graphite are observable. In contrast to that, the pattern of G03 (b) and G04 (not shown) exhibit a combination of several rings and some spots being the result of diffraction on randomly oriented polycrystalline graphite crystals and the diffuse scattering background due to an amorphous matrix.

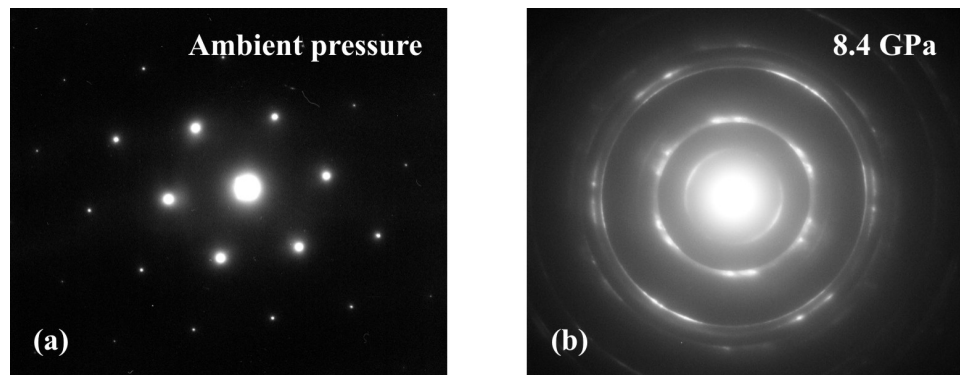


Figure 4.3.5: Electron diffraction patterns recorded on HOPG samples after heavy-ion irradiation at different pressure conditions. (a) At ambient pressure (G01), the characteristic diffraction pattern of crystalline graphite is observable. (b) The pattern of sample irradiated at 8.4 GPa (G03) displays sharp rings resulting from diffraction on randomly oriented polycrystalline graphite and a diffuse background resulting from amorphous graphite.

EELS spectra confirmed the existence of amorphous regions in the graphite samples irradiated within the stability field of diamond (G03 and G04). As an example, Figure 4.3.6 displays such spectra taken on the HOPG sample irradiated under 8.4 GPa (G03). As one can see, regions of amorphous graphite appears in the sample after irradiation (second spectrum from top). In addition to that, undamaged crystalline graphite is observable (third spectrum from top), similar to that before irradiation. No indications for diamond were found in any EELS spectrum.

While graphite is stable at ambient pressure and at 0.5 GPa , diamond is the stable room temperature phase at 8.4 and 12.1 GPa (Figure 4.3.1). Taking into account all findings mentioned above, it appears that the different behavior of graphite irradiated at different pressures is related to the stability fields of graphite and diamond. A transformation of crystalline graphite to the amorphous state occurs only when a sufficiently high pressure was adjusted in the DAC during irradiation, namely in the stability field of diamond ($P > 2 GPa$). These amorphous regions, found in TEM images and confirmed by Raman spectra, electron diffraction patterns, and EELS spectra, are not localized within

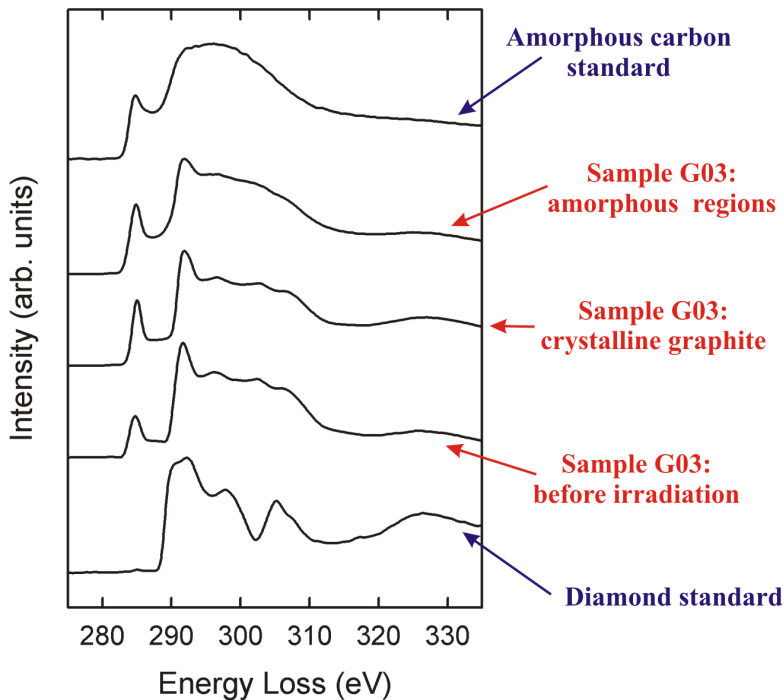


Figure 4.3.6: Electron energy-loss spectra (EELS) of graphite sample G03 before and after irradiation at 8.4 GPa together with the spectrum taken on standards of amorphous carbon and diamond. After irradiation, indications of amorphous graphite were found in the spectra beside crystalline graphite. No diamond was detectable in the sample.

the ion tracks, but distributed over a larger area. As mentioned in chapter 2.4.2, previous investigations of HOPG irradiations [LNTM01] resulted in a diameter of the amorphous track of about 3 nm . Connecting this value with a fluence of $1 \times 10^{11}\text{ cm}^{-2}$ which was used for irradiations of G03 and G04 leads to a track coverage of less than 1%. This is clearly in contrast to observations of the TEM images of Figure 4.3.4. If the irradiation is conducted outside the stability field of graphite, the ions obviously induce a structural damage of the entire matrix and are not restricted to the typical track cylinder.

A complete amorphisation of graphite was also found after ion implantation with maximum fluences of 10^{15} to 10^{16} ions/cm^2 , which is 4 to 5 orders of magnitude higher than in our irradiation experiments [DK92]. It should be noted that elastic collisions are the dominating stopping process for implanting experiments in the keV energy range and hence not comparable to irradiations with GeV ions, where the energy release is mainly based on electronic excitations.

Generally, the transformation of graphite into an amorphous phase requires a complete rearrangement of C – C bonds and is therefore probably only possible if quite high temperatures in the sample in the order of several 1000 K are reached. As mentioned earlier, the thermal-spike model predicts temperatures up to several 1000 K . However, this temperature rise is limited to the track core and thus can not explain alone the large

amorphous sample regions. Further mechanisms such as an interaction of an ion-induced shockwave with the pressurized target also may contribute.

In addition to amorphisation, also new crystallites of graphite were created in the amorphous matrix. It appears that the ions first initiated a transition from the crystalline to amorphous state, and afterwards the new graphite crystals were created within the amorphous zones. These turbostratic-like graphite flakes of a width of about 10 nm are another indication for elevated temperature conditions. A study of the recrystallization of graphite following high-fluence ion implantation experiments provided characteristic annealing temperatures associated with the graphitization process [DK92]. Turbostratic-like graphite was found for high temperatures to a maximum value of about 2000 K . Above this threshold, a second stage of graphitization is described, where a three-dimensional ordering occurs. The graphite crystals found in our experiments exhibit random orientations and a direct connection to the ion tracks is not obvious. It should be noted that graphitization temperatures found in experiments under ambient pressure might be different from those for high-pressure conditions.

Further irradiation experiments of graphite under high-pressure conditions will help to better understand the processes described above. By applying different ion energy losses, the temperature in the ion track can be altered according to the thermal-spike model. Irradiations with different ion fluences will allow us to change the mean distance between the tracks.

The fact that nucleation of diamond was not observed during the irradiation of graphite in the diamond stability field is probably related to the large nucleation barrier of diamond (see chapter 2.4.3). Beside the energy entry by means of temperature, also the time is an important parameter for the phase transition. The ions deposit their energy to the graphite sample and, according to the thermal-spike model, a heating within the track-core occurs for the duration of about 10^{-11} s . However, in future experiments, the creation of diamond may be facilitated by irradiating graphite samples above 20 GPa , where lower temperature are necessary for the creation of stable cubic diamond (Figure 2.4.2).

As mentioned earlier, several irradiation experiments have been performed at ambient pressure which produced nanocrystals of diamond [BA96, Ban97, WLB⁺97, ZB97, ZLB00, HSPD00, OPJ⁺01, DKLR01]. The beam parameters of Daulton et al. come closest to our experiments [DKLR01]. They irradiated graphite samples with 350 MeV Kr ions ($6 \times 10^{12}\text{ cm}^{-2}$) of comparable energy loss of 9 keV/nm at ambient pressure and found small crystals of diamond (mean diameter 7.5 nm) with a yield of $\approx 0.01\text{ crystals/ion}$. With the help of a proper etch solution, they dissolved the graphite and were able to find the diamonds in the residues. Therefore, also in our irradiations nanocrystals of diamonds were possibly created, but they are not detectable in the graphite samples by our methods, taking into account that the fluence was in our case even one order of magnitude lower.

In the case of irradiations at ambient pressure and 0.5 GPa (G01 and G02), the TEM images clearly showed single ion tracks as circular amorphous objects surrounded by

a strained matrix as displayed in the high-resolution image of G01 in Figure 4.3.7. TEM investigations of GeS showed similar strained regions in the vicinity of ion tracks [VSDN98]. To our knowledge, this was the first time that ion tracks are imaged in graphite. In previous TEM-studies on natural graphite and HOPG, no tracks could be found after ion irradiation which was explained by the authors by means of track annealing due to the electron beam [CFG⁺94, DJC98].

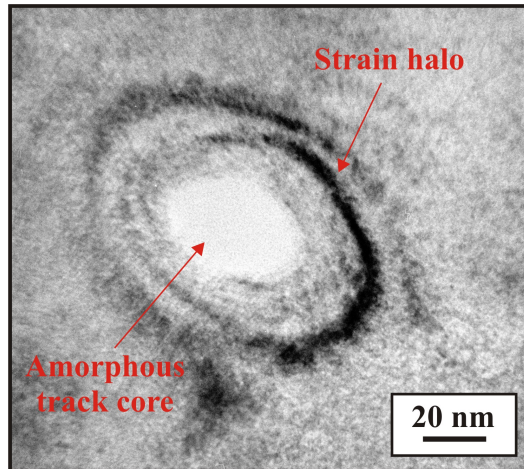


Figure 4.3.7: HRTEM image of G01 irradiated at ambient pressure. An ion track with amorphous core of about 25 nm in diameter and surrounding strained area can easily be recognized inside the otherwise undisturbed structure. The areal density of tracks is about three orders of magnitude lower than the ion fluence.

STM investigations of heavy-ion irradiated HOPG

For a comparison with TEM, sample G01 was investigated with STM. Since this sample was irradiated at ambient pressure, the size was about $0.5 \times 0.5 \text{ cm}^2$ with a thickness of about 2 mm and hence significantly larger than the other microscopic specimens enclosed in a DAC. Figure 4.3.8 showing a STM micrograph of high resolution.

Two ion tracks are visible as small irregular objects protruding from the crystalline matrix. The size of these tracks created by a 2.6-GeV uranium ion beam ($1 \times 10^{11} \text{ cm}^{-2}$) with high-energy-loss ions of 27 keV/nm is about 2-3 nm and is in full agreement with results obtained in previous investigations [LNTM01]. Furthermore, the areal density of tracks is in the same order of magnitude as the ion fluence. This means that both analyzing techniques results in different track diameters and areal track densities. Liu et al. showed by repeated cleavage and STM inspection on ion-irradiated HOPG that the size of amorphous trails in the bulk material is similar to that on the surface while the areal track density is reduced to about half by a given fluence [LNTM01]. It seems that this can not explain the discrepancy of the TEM as bulk and STM as surface method. Another explanation could be the following: STM was performed in the center of the 2 mm thick graphite specimen, whereas TEM could only be used on the wedge-shaped sample boundary. For a thickness of about 50-100 nm, the two surfaces are dominating

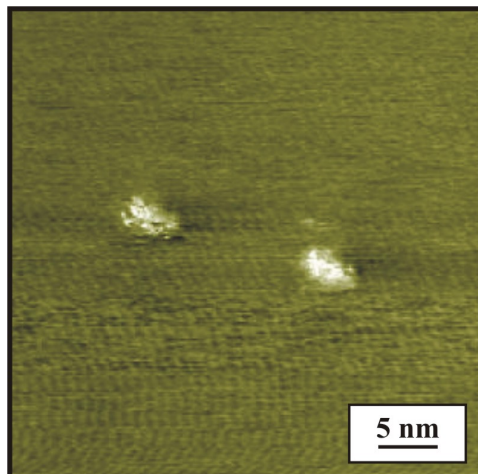


Figure 4.3.8: STM micrograph of G01 irradiated at ambient pressure. Two amorphous ion tracks of diameter 3 nm are visible. The areal track density is in accordance with the ion fluence.

and the ion track formation process is possibly different from that of bulk materials. It was not possible to perform STM measurements on the sample boundaries and, therefore, further experiments with thin HOPG samples of comparable thickness but larger surface should be performed where after ion irradiation an inspection with STM and TEM could help to understand the disagreement of track size and areal density.

As mentioned in the last section, the TEM images of G01 and G02 were similar, both of them exhibit ion tracks. G02 was pressurized in a DAC during the heavy-ion bombardment and, therefore, the sample was only about $150 \mu\text{m}$ in size (diameter). This almost microscopic specimen could not be imaged with STM because it was not possible to position the tip to such a small sample surface. Further improvements of the set-up are necessary to allow future STM measurements on samples irradiated in DACs.

4.4 Irradiation of apatite, zircon, rutile, and quartz

In a series of additional experiments, natural apatite ($\text{Ca}_5\text{F}(\text{PO}_4)_3$), quartz (SiO_2), rutile (TiO_2), and zircon (ZrSiO_4) were irradiated at various pressures. In most of these experiments, the pressure was adjusted in such a way that the respective mineral was outside its thermodynamic stability field. As mentioned earlier, these irradiations were performed as test experiments in order to find suitable materials for future high-pressure irradiation experiments. All of them were inspected by means of Raman spectroscopy and TEM investigations.

Results on apatite irradiation

Fission tracks are commonly used to date apatite. In order to simulate track formation under high-pressure and high-temperature conditions, we performed an irradiation ex-

periment under realistic Earth mantle conditions. Two apatite samples were irradiated, one at about 1 GPa and 430°C (A02), the other under ambient pressure and temperature conditions (A01). The results on energy-loss measurements in diamond (chapter 4.1) enabled us to adjust an ion-energy-loss value in the sample that corresponds to the one occurring in nature when fission fragments are slowing down in the mineral (17.5 keV/nm).

Figure 4.4.1 displays a micrograph of sample A01 irradiated at ambient pressure and temperature. The ion tracks are clearly detectable as amorphous regions embedded in the intact crystal. The track size is about 10 nm and the track density amounts to about $8 \times 10^{10} \text{ cm}^{-2}$, which is a factor 40 larger than the irradiation fluence. This deviation is probably caused by the irradiation with a focused ion beam, whose fluence can be inhomogeneously distributed within the beam spot (see Figure 4.2.5).

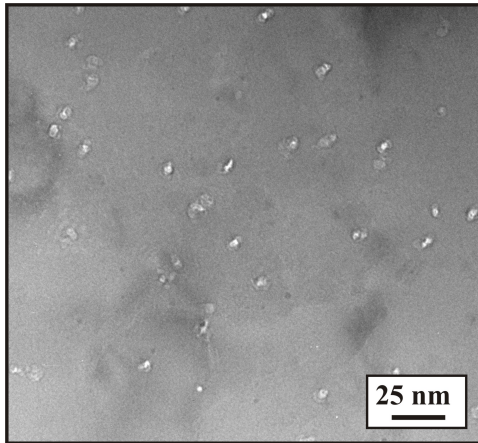


Figure 4.4.1: TEM image of apatite sample A01 irradiated at ambient pressure and temperature. Amorphous ion tracks of about 10 nm in diameter are visible as bright spots within an otherwise intact crystal.

However, the size of tracks is in good agreement with previous studies at ambient pressure conditions. Villa et al. irradiated the same kind of apatite (Durango apatite) with 157 MeV Kr ions of a comparable energy loss of 14 keV/nm [VGR⁺⁰⁰]. They found by channeling Rutherford backscattering spectrometry a track diameter of about 12 nm . One hour of annealing at 300°C after irradiation, resulted in a decrease of track diameter of about 40%.

TEM investigations on A02, irradiated at 1 GPa and 430°C did not reveal any ion tracks, even not at very high magnifications. The entire apatite sample showed a perfect crystalline lattice as displayed in Figure 4.4.2. As one can see in Table 3.4.3, sample A01 and A02 were irradiated with the same amount of ions of identical energy loss. Hence, the conclusion can be drawn that the ion tracks of sample A02 annealed during irradiation.

Since fission tracks are used in apatite to deduce the thermal history of the mineral, there is a large data set of annealing experiments [WdH92]. Green et al. annealed spontaneous

fission tracks in Durango apatite at various temperatures and time intervals [GDG⁺86]. For 1 hour at 300°C, they found after etching and electron microscopy a reduction in the track length of about 20%, whereas after 20 min at 400°C no tracks were observable.

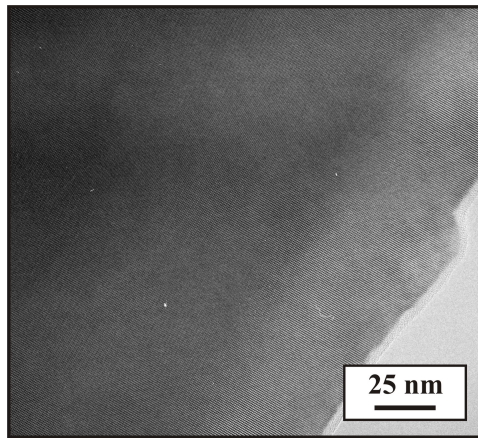


Figure 4.4.2: HRTEM image of apatite sample A02 irradiated at about 1 GPa. During the entire irradiation time of about 15 min, the sample was heated to 430°C. Otherwise the beam parameters were identical to irradiation of sample A01 (see Figure 4.4.1). Only the undamaged apatite lattice is visible and no indications for ion tracks were found.

In the case of our irradiation experiment of sample A02, the influence of the pressure on the ion-track formation can not clearly be analyzed. For irradiations at 300°C and 1 GPa, the ion tracks should have been detectable based on the experiments of Green et al. and Villa et al. [GDG⁺86, VGR⁺00], unless the pressure suppresses their creation. However, we can not rule out an exclusive thermal annealing during irradiation, because the temperature increased during irradiation to 430°C, possibly to the entire heating time of 15 min.

Future irradiation experiments of apatite at various pressure conditions and defined temperatures to a maximum of 300°C and below will help to clarify whether the fission-track formation in the Earth's crust is different to that at ambient conditions.

Results on zircon irradiation

The zircon sample was irradiated at 14.2 GPa, the highest pressure of all DAC irradiations performed by us. After irradiation and dismount, Z01 was investigated by means of Raman spectroscopy. Figure 4.4.3 displays two such spectra, recorded before and after irradiation. The irradiated zircon sample clearly shows several new bands, particularly at 810 and 840 cm^{-1} . These bands were also observed in previous Raman investigations and identified as bands of reidite, the high-pressure polymorph of ZrSiO_4 with scheelite structure [vWFH⁺04]. The presence of reidite was also confirmed by the observation of characteristic rings in electron diffraction patterns.

Additionally to that, TEM investigations have been performed on Z01. They revealed a complete conversion of the original single crystal of zircon into aggregates of zircon and

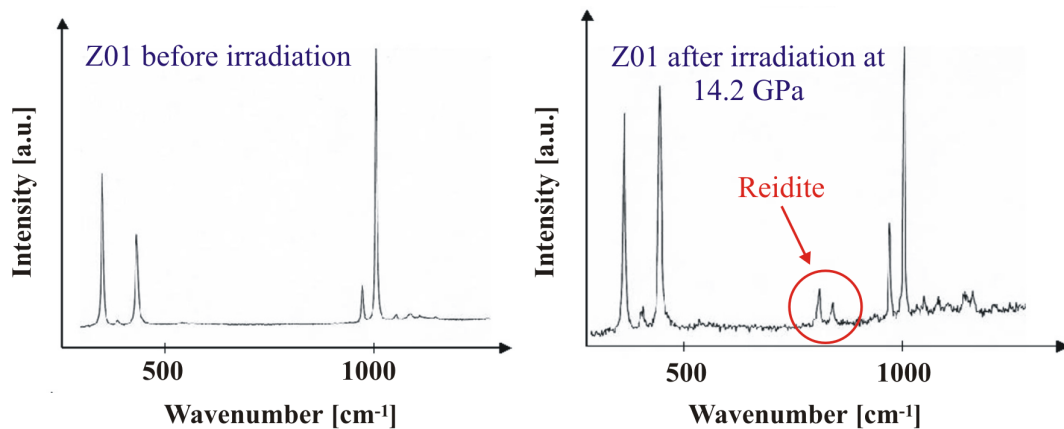


Figure 4.4.3: Raman spectrum of zircon sample Z01 before and after irradiation at 14.2 GPa.

In addition to zircon bands, several new bands of the high-pressure polymorph reidite are visible, particularly at 810 and 840 cm^{-1} .

randomly oriented irregular nanocrystals of reidite, about 10 nm in size, as shown in Figure 4.4.4. The areal density of the nanocrystals is several orders of magnitude higher than the applied fluence.

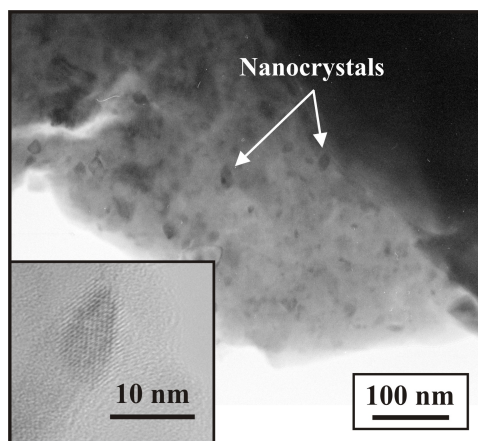


Figure 4.4.4: TEM image of zircon sample Z01 after irradiation at 14.2 GPa. The ions induced a conversion of the pressurized zircon sample into an aggregate of zircon and nanocrystals of reidite, about 10 nm in size as indicated by the inset.

Both observations imply that heavy-ion irradiation effected a substantial part of the zircon sample to convert into the stable high-pressure polymorph. There are several experiments that investigated the phase transition of zircon and reidite. Figure 4.4.5 displays the phase diagram of zircon according to Ono et al. who studied the behavior of zircon enclosed in a large-volume press at high P-T conditions [OFN⁺04]. At temperatures of 1100 K , they found reidite at pressures above 8 GPa (solid line in Figure 4.4.5). Diamond anvil cell experiments by Knittel et al. and van Westrenen et al. showed that the phase transition of zircon to reidite at room temperature occurs only at pressures

around or above 20 GPa [KW93, vWFH⁺04]. Shock experiments on zircon at room temperature by Kusaba et al. [KSKF85] resulted in reidite at pressures as high as 30 GPa . Ono et al. concluded that the temperature plays an important role in overcoming kinetic effects of the phase transitions from zircon to reidite which was supported by earlier investigations of Reid et al. [RR69]. Above 20 GPa and 1100 K , reidite dissociates into two dioxides (ZrO_2 and SiO_2) as indicated by the dashed line [TT04] and dotted line [Liu79] in Figure 4.4.5.

Our irradiation experiment was conducted at room temperature and 14.2 GPa which is indicated in Figure 4.4.5 by a filled circle.

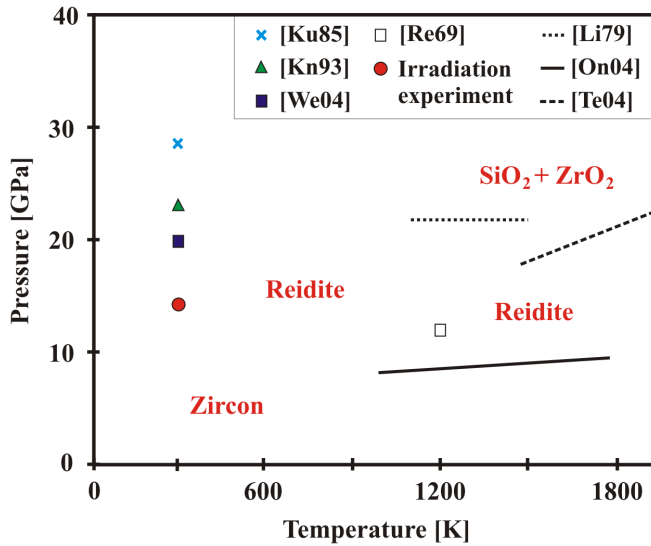


Figure 4.4.5: Simplified phase diagram of zircon according to Ono et al. [OFN⁺04]. Our irradiation experiment at 14.2 GPa (filled circle) was performed within the stability field of reidite, the high-pressure polymorph of zircon. The phase boundary of this transition was studied at high-temperature and high-pressure conditions by [RR69] and [OFN⁺04] (open square and solid line). Previous room temperature experiments using DAC [KW93, vWFH⁺04] and shock-waves [KSKF85] (filled triangle, filled square, and cross, respectively) obtained reidite for pressures of 20 GPa or higher. Reidite starts to dissociate into ZrO_2 and SiO_2 at pressure above 20 GPa and temperatures above 1100 K (dashed line [TT04] and dotted line [Liu79]).

It can be seen that the pressure during irradiation was significantly below the critical pressure found at room temperature for the zircon-reidite phase transition. Similar to the results of graphite irradiations at pressures within the stability field of diamond, the results on zircon give indications for heating effects by the ions. But taking into account the large number of reidite nanocrystals found in TEM images, it seems that the phase change occurs throughout the entire sample without evidence of individual ion tracks. These findings lead to the conclusion that the thermal-spike model alone could not explain the conversion of zircon into reidite at a pressure of 14.2 GPa .

Bursill et al. investigated heavy-ion irradiated zircon by means of TEM [BB90]. After irradiation at ambient pressure, the authors report on homogenous ion tracks of about 8 nm in diameter, a consisting value to previous investigations by Fleischer et al. [FPW75]. Additionally they observed elastically-strained regions outside the track core and conclude that the lead ions of 43 keV/nm used for the irradiations may caused a heating within the track core above 2000 K .

Results on rutile irradiation

The results on TEM investigations of R01 and a pristine rutile sample are being displayed in Figure 4.4.6. The image of the non-irradiated sample (a) shows a almost perfect crystalline lattice, as expected for a single-crystalline rutile. After irradiation the structure of the rutile lattice changed entirely (b). The ions caused a complete conversion of the rutile single crystal at 10.1 GPa to a nanocrystalline aggregate of crystals of random orientations with average crystal sizes around 10 nm , very similar to the effects observed for zircon. The areal density of nanocrystals is orders of magnitude higher than the ion fluence.

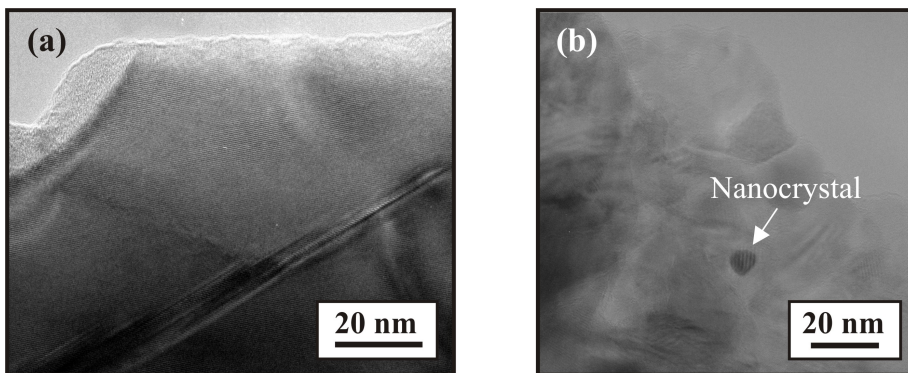


Figure 4.4.6: TEM images of rutile sample R01 before (a) and after irradiation at 10.1 GPa (b). The ions converted the pressurized single-crystalline rutile sample into a nanocrystalline aggregate of rutile crystals of random orientations with average crystal sizes around 10 nm .

A simplified phase diagram of rutile according to Withers et al. is displayed in Figure 4.4.7 [WEZ03]. The authors give a phase boundary between rutile and its high-pressure polymorph represented by a solid line. This result is deduced from several high-pressure and high-temperature experiments on rutile minerals [TE94, OGJ99, WEZ03].

High-temperature conditions could lead to the growth of new crystals of rutile. But as indicated by the filled circle in the phase diagram, the irradiation of R01 was conducted at 10.1 GPa and room temperature and hence in the stability field of the $\alpha\text{-PbO}_2$ polymorph of rutile. However, no clear evidence could be found for the presence of this high-pressure phase. If the temperature exceeds about 1600 K , rutile is stable at 10.1 GPa (open circle) and, therefore, our results could be interpreted by means of heating above 1600 K . But the number of rutile crystals is not connected to the number of ions and this is problematic when using exclusively the thermal-spike model as possible explanation.

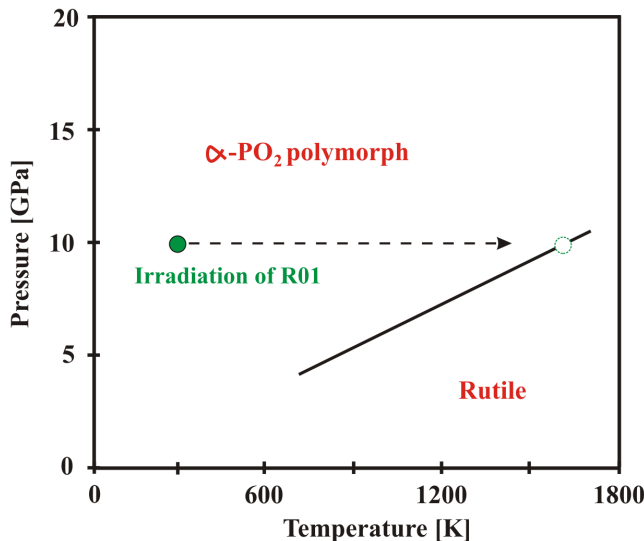


Figure 4.4.7: Simplified phase diagram of rutile according to Withers et al. [WEZ03]. The stability field of rutile and its high-pressure phase, the $\alpha\text{-PbO}_2$ polymorph, is separated by a phase boundary based on experiments of [TE94, OGJ99, WEZ03]. Sample R01 was irradiated at 10.1 GPa and room temperature (filled circle) within the stability field of the high-pressure phase and no indications for the $\alpha\text{-PbO}_2$ polymorph could be found. At a pressure of 10.1 GPa and temperatures of about 1650 K (open circle) or higher, rutile is the stable phase.

Results on quartz irradiation

The results of the quartz irradiation at 5.1 GPa are presented in Figure 4.4.8 by means of a TEM image. The ions generated amorphous tracks visible as parallel oriented cylinders of light contrast.

Their diameter is about 15 nm and thus 35% larger than track sizes obtained in previous quartz irradiation experiments at ambient pressure. Meftah et al. performed studies on track formation in this mineral by TEM and Rutherford backscattering ion channeling. For an irradiation with 62 MeV Pb ions of comparable energy loss (15 keV/nm), they obtained a track diameter of 11 nm using TEM [AMDHA⁺94]. It should be mentioned, that this irradiation was conducted with ions of much lower velocity (low-energy side of the Bragg peak in Figure 2.1.1), than in our case (high-energy side of the Bragg peak in Figure 2.1.1). Toulemonde et al. described the track creation in quartz using the thermal spike model [TCD⁺96] and obtained amorphous tracks of diameter 8–11 nm for energy loss values comparable to our irradiation experiment. The authors assume that temperatures between 2000 and 3000 K were reached during irradiation in order to create a molten liquid phase along the ion path.

Figure 4.4.9 displays a simplified phase diagram of quartz according to Bose et al. and it is obvious that the irradiation of Q01 (filled circle) was inside the stability field of the coesite polymorph [BG95]. For quartz, no conversion to the high-pressure phase coesite could be detected in TEM images and electron diffraction patterns. The bulk

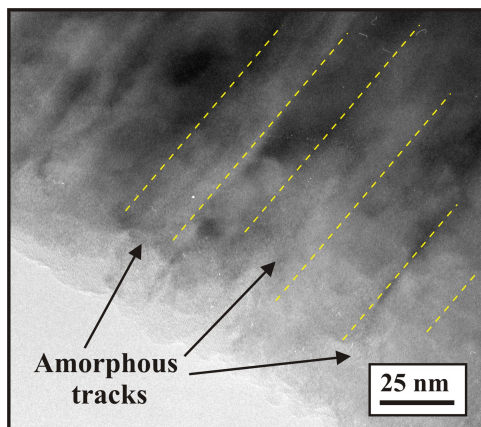


Figure 4.4.8: TEM image of quartz sample Q01 after irradiation at 5.1 GPa. Aligned amorphous tracks of about 15 nm are visible. The tracks are embedded in a matrix of single-crystalline quartz. No indication for the high-pressure phase coesite could be detected.

of the sample in the vicinity of ion tracks remained single-crystalline quartz without any indication of the formation of large amorphous or nanocrystalline areas as in the case of HOPG, zircon, and rutile. This means that the track formation process at 5.1 GPa was similar to that under ambient pressure [AMDHA⁺94] with similar track sizes. However, small deviations in the size and structure of tracks can not be excluded. Therefore, future irradiation experiments are necessary, where additionally to a high-pressure irradiation, a control sample at ambient pressure has to be irradiated with identical beam parameters.

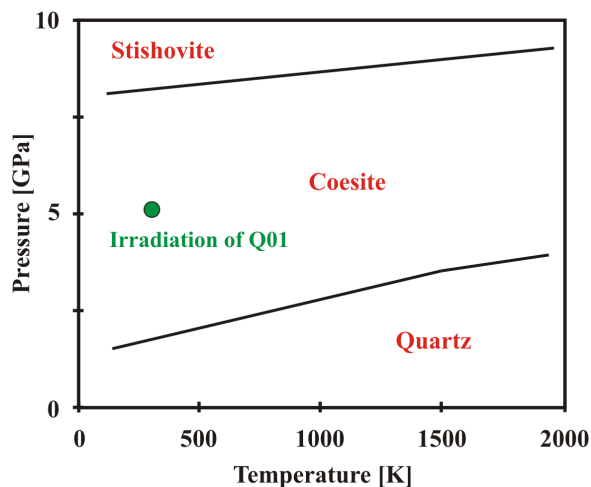


Figure 4.4.9: Simplified phase diagram of quartz according to Bose et al. [BG95]. Sample Q01 was irradiated at 5.1 GPa as indicated by the filled circle. The pressure was adjusted far into the stability field of coesite, the high-pressure phase of quartz. At pressures of about 8 GPa or higher, another stability field of stishovite starts. After irradiation, no indication for coesite could be found.

Summary

The results clearly demonstrate that heavy ions are able to cause phase transitions and pervasive changes in the microstructure of minerals, if the irradiation occurs under pressures. The different response of various minerals is probably related to the nature of potential phase transitions. The quartz to coesite phase transition is reconstructive comparable to the graphite to diamond transition. In contrast to that, the phase transitions of zircon and rutile to their high-pressure polymorphs are displacive, requiring only a relatively minor displacement of structural units. In general, reconstructive phase transitions tend to be slower and require higher activation energies than displacive transitions. It is therefore not surprising that the formation of a high-pressure phase upon irradiation was observed for zircon, but not for quartz.

In zircon and rutile, the microstructure of the samples were changed entirely by ion irradiations at high-pressure. This was also the case for the graphite irradiations conducted within the stability field of diamond. The fact that these changes are pervasive through large areas of the samples is quite surprising, considering the low ion fluences applied. Under normal circumstances, major structural changes occur only within the nm-sized cylindrical track. Assuming for rutile and zircon a track diameter of 10 nm and taking into account a fluence of $2 \times 10^9 \text{ ions/cm}^2$, the ions should affect the structures to a maximum of 0.2%. In the case of graphite irradiations within the stability field of diamond, this value amounts to 0.7%, when assuming a track diameter of 3 nm and connecting this with a fluence of $1 \times 10^{11} \text{ ions/cm}^2$. Both numbers are in clear contrast to our TEM observations, revealing phase changes throughout the entire sample without evidence of individual ion tracks. Apparently, high pressure can change significantly the efficiency of heavy-ion interaction with minerals. While the formation of individual ion tracks can be completely suppressed, heavy ions may trigger the nucleation of new phases, which then continue to grow even far outside the typical track volume at ambient pressure.

As mentioned in chapter 4.3, the conversion from HOPG to amorphous carbon may implicate that local heating by the heavy ions took place. These findings are supported by the results for rutile. If temperatures in the order of several 1000 K were indeed reached during irradiation, the conversion to the $\alpha\text{-PbO}_2$ structure can not be expected because above 1650 K , rutile is stable at 10.1 GPa . Furthermore, the presence of the zircon high-pressure polymorph after high-pressure irradiation may additionally support the assumption of local heating events caused by the ions.

Chapter 5

Conclusion and outlook

Most minerals that are important for geochronology, are placed deep below the Earth's surface during some part of their history. They are thus subjected to considerable pressure up to the GPa range. In the field of dating based on fission fragments, the effect of pressure on track formation has been discussed for many years [FPW65a], but up to now there was no direct access for experimental tests. In this thesis, it was clearly demonstrated that ion tracks can be produced in pressurized solids by using diamond anvil cells and expose them to relativistic heavy ion beams.

Several experiments irradiating the trioctahedral mica phlogopite to 8.4 GPa with 15 GeV U ions revealed that the formation of etchable tracks is independent of pressure. Similar results are obtained for the 5.1 GPa irradiation of SiO_2 quartz, where typical amorphous tracks are visualized by TEM.

For the irradiation of an apatite ($\text{Ca}_5\text{F}(\text{PO}_4)_3$) sample, we tested the simultaneous application of pressure and temperature. No tracks were found after an irradiation at 1 GPa and 430°C, and the radiation damage was possibly annealed during the irradiation by the high temperature. Previous annealing experiments found that at 400°C complete track annealing occurs for heating times similar to our irradiation experiment.

Surprising new effects of pressure were observed when exposing highly oriented pyrolytic graphite (HOPG), natural zircon (ZrSiO_4), and rutile (TiO_2) to the ion beam. For pressure adjustments outside the thermodynamic stability field, we find a complete amorphization of the entire sample (HOPG) and the generation of nm-sized aggregates of secondary crystals (HOPG, rutile). Also the nucleation of a new phase was observed (zircon). These findings indicate that the ions caused a substantial heating of the pressurized mineral. The pervasive structural changes imply that under pressure additional effects such as ion-induced shockwaves may play an important role.

In conclusion of these first results, we suggest that under geologically relevant conditions, there might exist specific mechanisms for the nucleation of new phases that have never been considered in any geophysical model. For example, during subduction olivine ($(\text{Mg}, \text{Fe})_2\text{SiO}_4$) is transported into deeper parts of the upper mantle and persists there far inside the stability field of its high-pressure phase. The sudden conversion of large volumes of this metastable olivine into ringwoodite has been linked to the origin of deep-focus earthquakes [SB76]. For such a phase change, fission fragments from the decay of ^{238}U -nuclei may play a crucial role, because in nature up to $10^4 \mu\text{g/g}$ of ^{238}U can be in-

corporated in minerals such as zircon, leading to spontaneous fission and track densities as high as 10^7 cm^{-2} over geological time intervals of Ma [WdH92]. As demonstrated in our high-pressure experiments, 10^9 tracks/cm^2 can induce a phase transition of the host mineral. This would have implications for the kinetics of phase transitions during global geodynamic processes and would imply that models for the presence of metastable phases in subduction zones have to be revised.

Future irradiation experiments should not only test the track-formation process under the influence of a hydrostatic pressure but also the one under shear stress. In nature, most rocks are exposed to shear stress which can additionally enhance the probability for phase transitions. In addition, it has to be clarified whether the alpha decay, being 10^6 times more abundant than spontaneous fission, is able to initiate or support potential phase transformations.

Beside geosciences, the irradiation of pressurized solids with heavy ions has also implications in materials science. During high-pressure experiments, new materials and compounds can be synthesized with specific unique properties (e.g. electric and magnetic features, and enhanced hardness). Solids that are stable only at high-pressure conditions have never been exposed to ion beams. It would be interesting to test their response to heavy-ion irradiation. Furthermore, pressurized materials could be nanostructured by creating ion tracks with properties different from the surrounding bulk material. Also the creation of so-called pinning centers in high-pressure superconductors of pure elements could be performed by heavy-ion irradiation under high pressure, analogous to the irradiation of superconductors at ambient pressure [WGS⁺04].

The FAIR future project of GSI will provide even more extreme irradiation conditions than tested in this thesis. It is planned to increase the beam fluxes significantly which will allow the irradiation of samples at higher fluences. Given by larger beam energies, bigger samples can be reached, that require larger pressure cells. Also the possibility of a pulsed-ion-beam irradiation could have some new aspects. Lee et al. induced shockwaves in precompressed samples by means of a laser pulse through one of the diamond anvils [Le002]. They report that a variation of the initial density makes it possible to obtain data apart from the principle Hugoniot, accessing conditions that are unreachable by either static or dynamic compression experiments alone, because they start only at normal density and ambient pressure. However, the short laser pulse allows only the use of $200\text{-}\mu\text{m}$ thin diamonds and thus the precompression is limited to about 1 GPa. With an intense pulsed ion beam, shockwaves can be created with a beam deposition power of 10 GW/g. Similar to the laser experiment, these shockwaves may be applied to samples that are precompressed to much higher pressure values than 1 GPa.

Bibliography

- [AAN⁺96] J. Ackermann, N. Angert, R. Neumann, C. Trautmann, M. Dischner, T. Hagen, and M. Sedlacek. Ion track diameters in mica studied with scanning force microscopy. *Nucl. Instr. and Meth. B*, 107:181–184, 1996.
- [AAS⁺85] D. Albrecht, P. Armbruster, R. Spohr, M. Roth, K. Schaupert, and H. Stuhrmann. Investigation of heavy ion produced defect structures in insulators by small angle scattering. *Appl. Phys. A*, 37:37–46, 1985.
- [ABJ⁺93] A. Audouard, E. Balanzat, J.C. Jousset, D. Lesueur, and L. Thomé. Atomic displacements and atomic motion induced by electronic excitation in heavy-ion-irradiated amorphous metallic alloys. *J. Phys. Condens. Matter*, 5:995–1018, 1993.
- [ABS86] D. Albrecht, E. Balanzat, and K. Schaupert. X-ray small angle scattering investigation of high energy ar-tracks in mica. *Nucl. Tracks Radiat. Meas.*, 11:93–94, 1986.
- [AD63] R.B. Aust and H.G. Drickamer. Carbon: a new crystalline phase. *Science*, 140:817–819, 1963.
- [AMDHA⁺94] J.M. Costantini A. Meftah, F. Brisard, E. Dooryhee, M. Hage-Ali, M. Hervieu, J.P. Stoquert, F. Studer, and M. Toulemonde. Track formation in SiO₂ quartz and the thermal-spike mechanism. *Phys. Rev. B*, 49:12457–12463, 1994.
- [AMNW98] J. Ackermann, A. Müller, R. Neumann, and Y. Wang. Scanning force microscopy on heavy-ion tracks in muscovite mica: track diameter versus energy loss and loading force. *Appl. Phys. A*, 66:1151–1154, 1998.
- [AS72] M. Abramowitz and I.A. Stegun. *Handbook of Mathematical Functions with Formulas, Graphs and Mathematical Tables*. New York, Dover, 1972.
- [BA96] F. Banhart and P.M. Ajayan. Carbon onions as nanoscopic pressure cells for diamond formation. *Nature*, 382:433–435, 1996.
- [Ban97] F. Banhart. The transformation of graphitic onions to diamond under electron irradiation. *J. Appl. Phys.*, 81:3440–3445, 1997.
- [Bas80] W.A. Bassett. Synchrotron radiation, an intense x-ray source for high pressure diffraction studies. *Phys. Earth Planet. Inter.*, 23:337–340, 1980.
- [BB63] W.A. Bassett and E.M. Broyd. High pressure research - applications in geophysics, 1963.

- [BB77] S. Block and P.M. Bell. High pressure research - applications in geo-physics, 1977.
- [BB90] L.A. Bursill and G. Braunhausen. Heavy-ion irradiation tracks in zircon. *Philos. Mag. A*, 62:395–420, 1990.
- [BBP73] J.D. Barnett, S. Block, and G.J Piermarini. An optical fluorescence system for quantitative pressure measurement in the diamond-anvil cell. *Rev. Sci. Instr.*, 44:1–9, 1973.
- [BBSW61] F.P. Bundy, H.P. Bovenkerk, H.M. Strong, and R.H. Wentorf Jr. Diamond-graphite equilibrium line from growth and graphitization of diamond. *J. Chem. Phys.*, 35:383–391, 1961.
- [BBW⁺96] F.P. Bundy, W.A. Bassett, M.S. Weathers, R.J. Hemley, H.K. Mao, and A.F. Goncharov. The pressure-temperature phase and transformation diagram for carbon; updated through 1994; review article. *Carbon*, 34:141–153, 1996.
- [BCPT93] S. Bouffard, J. Cousty, Y. Pennec, and F. Thibaudeau. STM and AFM observations of latent tracks. *Radiat. Eff. Def. Solids*, 126:225–228, 1993.
- [BD61] A.S. Balchan and H.G. Drickamer. High pressure electrical resistance cell, and calibration points above 100 kilobars. *Rev. Sci. Instrum.*, 32:308–313, 1961.
- [BE60] F.R. Boyd and J.L. England. Apparatus for phase-equilibrium measurements at pressures up to 50 kilobars and temperatures up to 1750°C. *J. Geophys. Res.*, 65:741–748, 1960.
- [BEM02] R. Boehler, D. Errandonea, and M. Ross. The laser-heated diamond cell: High p-t phase diagrams. In R.J. Hemley, G.L. Chiarotti, M. Bernasconi, and L. Ulivi, editors, *High Pressure Phenomena*, number CXLVII in Proc. International School of Physics 'Enrico Fermi', pages 55–72, 2002.
- [Ben03a] A. Benyagoub. Evidence of an ion-beam induced crystalline-to-crystalline phase transformation in hafnia. *Eur. Phys. J. B*, 34:395–398, 2003.
- [Ben03b] A. Benyagoub. Kinetics of the crystalline to crystalline phase transformation induced in pure zirconia by swift heavy ion irradiation. *Nucl. Instr. and Meth. B*, 206:132–138, 2003.
- [BFA61] G. Bonfiglioli, A. Ferro, and A. Mojoni. Electron microscope investigation on the nature of tracks of fission products in mica. *J. Appl. Phys.*, 32:2499–2503, 1961.
- [BFRA97] F. Banhart, T. Füller, Ph. Redlich, and P.M. Ajayan. The formation and self- compression of carbon onions. *Chem. Phys. Lett.*, 269:349–355, 1997.
- [BG95] K. Bose and J. Ganguly. Quartz-coesite transition revisited: reversed experimental determination at 500-1200°C and retrieved thermodynamic

- properties. *Am. Mineral.*, 80:231–238, 1995.
- [BGH95] L.P. Biró, J. Gyulai, and K. Havancsák. Scanning-tunneling-microscope investigation of a 215-mev ne-irradiated graphite surface. *Phy. Rev. B*, 52:2047–2053, 1995.
- [BK67] F.P. Bundy and J.S. Kasper. Hexagonal diamond-a new form of carbon. *J. Chem. Phys.*, 46:3437–3446, 1967.
- [BLRK92] A. Benyagoub, S. Löffler, M. Rammensee, and S. Klaumünzer. Plastic deformation in SiO_2 induced by heavy-ion irradiation. *Nucl. Instr. and Meth. B*, 65:228–231, 1992.
- [Boe93] R. Boehler. Temperatures in the earth’s core from melting-point measurements of iron at high static pressures. *Nature*, 363:534–536, 1993.
- [Boe96] R. Boehler. Melting of mantle and core materials at very high pressures. *Phil. Trans. R. Soc. Lond. A*, 354:1265–1278, 1996.
- [Br449] *Linear compressions to 30000 kg/cm² , including relatively incompressible substances*. Am. Arts. Sci., 1949.
- [BRGL96] W. Bolse, K. Reimann, U. Geyer, and K.P. Lieb. Surface and sub-surface defects on graphite after single ion impact studied with STM. *Nucl. Instr. and Meth. B*, 118:488–492, 1996.
- [Bri58] P.W. Bridgman. *Physics of High Pressure*. G. Bell and Sons, London, 1958.
- [Bri63] P.W. Bridgman. Solids under pressure, 1963.
- [BSB93] W.A. Bassett, A.H. Shen, and M. Buckum. A new diamond anvil cell for hydrothermal studies to 2.5 GPa and from -190°C to 1200°C. *Rev. Sci. Instrum.*, 64:2340–2345, 1993.
- [BSBC93] W.A. Bassett, A.H. Shen, M. Buckum, and I.M. Chou. Hydrothermal studies in a new diamond anvil cell up to 10 GPa and from -190°C to 1200°C. *Pure Appl. Geophys.*, 141:487–495, 1993.
- [BSM⁺81] E.M. Brody, H. Shimizu, H.K. Mao, P.M. Bell, and W.A. Bassett. Acoustic velocity and refractive index of fluid hydrogen and deuterium at high pressures. *J. Appl. Phys.*, 52:3583–3585, 1981.
- [BT65] W.A. Bassett and T. Takahashi. Silver iodide polymorphs. *Am. Mineral.*, 50:1576–1594, 1965.
- [BTS67] W.A. Bassett, T. Takahashi, and P. Stook. X-ray diffraction and optical observations on crystalline solids up to 300 kbar. *Rev. Sci. Instrum.*, 38:37–42, 1967.
- [Bun63a] F.P. Bundy. Direct conversion of graphite to diamond in static pressure apparatus. *J. Chem. Phys.*, 38:631–643, 1963.
- [Bun63b] F.P. Bundy. Melting of graphite at very high pressure. *J. Chem. Phys.*,

- 38:618–630, 1963.
- [BVEG90] P. Badziag, W.S. Verwoerd, W.P. Ellis, and N.R. Greiner. Nanometer diamonds are more stable than graphite. *Nature*, 343:244–245, 1990.
- [BXM86] P.M. Bell, J.A. Xun, and H.K. Mao. Static compression of gold and copper and calibration of the ruby pressure scale to pressures to 1.8 megabars. In Y.M. Gupta, editor, *Shock waves in condensed matter*, pages 125–130. Plenum Press, New York, 1986.
- [BYM89] Y. Bar-Yam and T.D. Moustakas. Defect-induced stabilization of diamond films. *Nature*, 342:786–787, 1989.
- [CCAB90] R. Coratger, A. Claverie, F. Ajustron, and J. Beauvillain. Scanning tunneling microscopy of defects induced by carbon bombardment on graphite surfaces. *Surf. Sci.*, 227:7–14, 1990.
- [CCC⁺92] R. Coratger, A. Claverie, A. Chahboun, V. Landry, F. Ajustron, and J. Beauvillain. Effects of ion mass and energy on the damage induced by an ion beam on graphite surfaces: a scanning tunneling microscopy study. *Surf. Sci.*, 262:208–218, 1992.
- [CDB⁺94] V. Chailley, E. Dooryhée, S. Bouffard, E. Balanzat, and M. Levalois. Observations by x-ray diffraction of structural changes in mica irradiated by swift heavy ions. *Nucl. Instr. and Meth. B*, 91:162–167, 1994.
- [CDL96] V. Chailley, E. Dooryhée, and M. Levalois. Amorphization of mica through the formation of gev heavy ion tracks. *Nucl. Instr. and Meth. B*, 107:199–203, 1996.
- [CDM⁺01] P. Comodi, M. Drábek, M. Montagnoli, M. Rieder, Z. Weiss, and P.F. Zanazzi. Pressure-induced phase transition in a new synthetic rb-mica. *FIST-Geoitalia*, 2001.
- [CFG⁺94] L.T. Chadderton, D. Fink, Y. Gamaly, H. Moeckel, L. Wang, and H. Omichi. Synthesis of buckminsterfullerene in the wake of energetic ions. *Nucl. Instr. and Meth. B*, 91:71–77, 1994.
- [CKK93] W. Choi, C. Kim, and H. Kang. Interactions of low energy (10-600 ev) noble gas ions with a graphite surface: surface penetration, trapping and self-sputtering behaviors. *Surf. Sci.*, 281:323–335, 1993.
- [CLL96] G. Chen, B. Li, and R.C. Liebermann. Selected elastic moduli of single-crystal olivines from ultrasonic experiments to mantle pressures. *Science*, 272:979–980, 1996.
- [CLW98] G. Chen, R.C. Liebermann, and D.J. Weidner. Elasticity of single-crystal mgo to 8 gigapascals and 1600 kelvin. *Science*, 280:1913–1916, 1998.
- [Coe53] L. Coes. A new dense crystalline silica. *Science*, 118:131–132, 1953.
- [CRD95] T. Cabioc'h, J.P. Riviere, and J. Delafond. A new technique for fullerene onion formation. *J. Matter. Sci.*, 30:4787–4792, 1995.

- [Cru04] S.A. Cruz. Pressure effects on the stopping and range of heavy ions. *Nucl. Instr. and Meth. B*, 222:411–420, 2004.
- [CZZ⁺99] P. Comodi, P.F. Zanazzi, Z. Weiss, M. Rieder, and M. Drábek. Cs-tetra-ferri-annite: High-pressure and high-temperature behavior of a potential nuclear waste disposal phase. *Am. Mineral.*, 84:325–332, 1999.
- [DBPT99] C. Dufour, F. Beuneu, E. Paumier, and M. Toulemonde. Experimental evidence of the irradiation temperature effect in bismuth under swift heavy-ion irradiation. *Europhys. Lett.*, 45:585–590, 1999.
- [DDLM81] E. Dartyge, J.P. Duraud, Y. Langevin, and M. Maurette. New model of nuclear particle tracks in dielectric minerals. *Phys. Rev. B.*, 23:5213–5229, 1981.
- [DEB⁺96] T.L. Daulton, D.D. Eisenhour, T.J. Bernatowicz, R.S. Lewis, and P.R. Buseck. Genesis of presolar diamonds: Comparative high-resolution transmission electron microscopy study of meteoritic and terrestrial nanodiamonds. *Geochim. Cosmochim. Acta*, 60:4853–4872, 1996.
- [Des23] F. Desauer. Über einige wirkungen von strahlen. IV. *Zs. f. Phys.*, 12:288–298, 1923.
- [DHE⁺95] D.D.N.B. Daya, A. Hallén, J. Eriksson, J. Kopniczky, R. Papaléo, C.T. Reimann, P. Håkansson, B.U.R. Sundqvist, and A. Brunelle. Radiation damage features on mica and l-valine probed by scanning force microscopy. *Nucl. Instr. and Meth. B*, 106:38–42, 1995.
- [DHH⁺95] D.D.N.B. Daya, A. Hallén, P. Håkansson, B.U.R. Sundqvist, and C.T. Reimann. Scanning force microscopy study of surface tracks induced in mica by 78.2-mev ^{127}I ions. *Nucl. Instr. and Meth. B*, 103:454–465, 1995.
- [DJC98] A. Dunlop, G. Jaskierowicz, and L.T. Chadderton. High resolution transmission electron microscopy of gev heavy ion irradiated graphite. *Nucl. Instr. and Meth. B*, 145:532–538, 1998.
- [DK92] M.S. Dresselhaus and R. Kalish. Ion implantation in diamond, graphite and related materials. volume 22. Springer, Berlin, Heidelberg, New York, London, Paris, Tokyo, 1992.
- [DKLR01] T.L. Daulton, M.A. Kirk, R.S. Lewis, and L.E. Rehn. Production of nanodiamonds by high-energy ion irradiation of graphite at room temperature. *Nucl. Instr. and Meth. B*, 175-177:12–20, 2001.
- [DLRK99] T.L. Daulton, R.S. Lewis, L.E. Rehn, and M.A. Kirk. Heavy-ion irradiation-induced diamond formation in carbonaceous materials. *Mat. Res. Soc. Symp. Proc.*, 540:189–194, 1999.
- [DM74] E. Dartyge and M. Lambert. Formation de defauts dans les échantillons de mica muscovite irradiés par des ions de grande énergie. *Radiat. Eff.*,

- 21:71–79, 1974.
- [DMM76] E. Dartyge, M. Lambert, and M. Maurette. Structure et enregistrement des traces latentes díons argon et fer dans lólivine et le mica muscovite. *J. de Phys.*, 37:939–943, 1976.
- [DO71] T.L. Daulton and M. Ozima. Radiation-induced diamond formation in uranium-rich carbonaceous materials. *Science*, 1996:1260–1263, 271.
- [DRH⁺96] D.D.N.B. Daya, C.T. Reimann, A. Hallén, B.U.R. Sundqvist, and P. Håkansson. Latent (sub-surface) tracks in mica studied by tapping mode scanning force microscopy. *Nucl. Instr. and Meth. B*, 111:87–90, 1996.
- [EDD⁺81] B.S. Elman, M.S. Dresselhaus, G. Dresselhaus, E.W. Maby, and H. Mazurek. Raman scattering from ion-implanted graphite. *Phys. Rev. B*, 24:1027–1034, 1981.
- [EGS89a] J.H. Eggert, K.A. Goettel, and I.F. Silvera. Ruby at high pressure. i. optical line shifts to 156 GPa. *Phys. Rev. B*, 40:5724–5732, 1989.
- [EGS89b] J.H. Eggert, K.A. Goettel, and I.F. Silvera. Ruby at high pressure. II. fluorescence lifetime of the r line to 130 GPa. *Phys. Rev. B*, 40:5733–5738, 1989.
- [EGS⁺00] M.I. Eremets, E. Gregoryanz, V.V. Struzhkin, H.K. Mao, R.J. Hemley, N. Mulders, and N.M. Zimmerman. Electrical conductivity of xenon at megabar pressures. *Phys. Rev. Lett.*, 85:2797–2800, 2000.
- [EME⁺89] J.H. Eggert, F. Moshry, W.J. Evans, K.A. Goettel, and I.F. Silvera. Ruby under pressure III. a pumping scheme for the r lines up to 230 GPa. *Phys. Rev. B*, 44:7202–7208, 1989.
- [Ere96] M. Eremets. *High-Pressure Experimental Methods*. Oxford University Press, New York, 1996.
- [ESD⁺82] B.S. Elman, M. Shayegan, M.S. Dresselhaus, H. Mazurek, and G. Dresselhaus. Structural characterization of ion-implanted graphite. *Phys. Rev. B*, 25:4142–4156, 1982.
- [ESMH01] M.I. Eremets, V.V. Struzhkin, H.K. Mao, and R.J. Hemley. Superconductivity in boron. *Science*, 293:272–274, 2001.
- [FJ97] N. Funamori and R. Jeanloz. High-pressure transformation of Al_2O_3 . *Science*, 278:1109–1111, 1997.
- [FK78] L.W. Finger and H.E. King. A revised method of operating of the single-crystal diamond cell and refinement of nacl at 32 kbar. *Am. Mineral.*, 63:337–342, 1978.
- [FM94] Y. Fei and H.K. Mao. In situ determination of the nias phase of feo at high pressure and temperature. *Science*, 266:1668–1680, 1994.

- [FPSM64] R.L. Fleischer, P.B. Price, E.M. Symes, and D.S. Miller. Fission track ages and track-annealing behavior of some micas. *Science*, 143:349–351, 1964.
- [FPW65a] R.L. Fleischer, P.B. Price, and R.M. Walker. Effects of temperature, pressure, and ionization on the formation and stability of fission tracks in minerals and glasses. *J. Geophys. Res.*, 70:1497–1502, 1965.
- [FPW65b] R.L. Fleischer, P.B. Price, and R.M. Walker. The ion explosion spike mechanism for formation of charged particle tracks in solids. *J. Appl. Phys.*, 36:3645–3652, 1965.
- [FPW65c] R.L. Fleischer, P.B. Price, and R.M. Walker. Solid-state track detectors: Applications to nuclear science and geophysics. *Annu. Rev. Nucl. Sci.*, 15:1–28, 1965.
- [FPW75] R.L. Fleischer, P.B. Price, and R.M. Walker. *Nuclear Tracks in Solids*. University of California Press, Berkeley, 1975.
- [FPWH64] R.L. Fleischer, P.B. Price, R.M. Walker, and E.L. Hubbard. Track registration in various solid-state nuclear track detectors. *Phys. Rev.*, 133:A1443–A1449, 1964.
- [GBC⁺96] F. Garrido, A. Benyagoub, A. Chamberod, J.-C. Dran, A. Dunlop, S. Klaumünzer, and L. Thomé. Giant deformation of solids irradiated with swift heavy ions: behavior of amorphous/crystalline multilayers. *Nucl. Instr. and Meth. B*, 115:430–439, 1996.
- [GBH⁺87] H. Gauvin, R. Bimbot, J. Herault, R. Anne, G. Bastin, and F. Hubert. Stopping powers of solids for ^{16}O ions at intermediate energies (20–95 mev/u). *Nucl. Instr. and Meth. B*, 28:191–194, 1987.
- [GDG⁺86] F. Green, I.R. Duddy, A.J.W. Gleadow, P.R. Tingate, and G.M. Laslett. Thermal annealing of fission tracks in apatite 1. a qualitative description. *Chem. Geol.*, 59:237–253, 1986.
- [GDG⁺03] A. El Goresy, L.S. Dubrovinsky, Ph. Gillet, S. Mostefaoui, G. Graup, M. Drakopoulos, A.S. Simionovici, V. Swamy, and V.L. Masaitis. A novel cubic, transparent and super-hard polymorph of carbon from the ries and popigal craters: Implications to understanding dynamic-induced natural high-pressure phase transitions in the carbon system. *Lun. Planet. Sci.*, XXXIV:1016, 2003.
- [GHMS98] A.F. Goncharov, R.J. Hemley, H.K. Mao, and J.F. Shu. New high-pressure excitations in para-hydrogen. *Phys. Rev. Lett.*, 80:101–114, 1998.
- [GKDK03] A.A. Gippius, R.A. Khmelnitsky, V.A. Dravin, and A.V. Khomich. Diamond-graphite transformation induced by light ions implantation. *Diamond and Relat. Mater.*, 12:538–541, 2003.
- [GLK⁺03] U.A. Glasmacher, M. Lang, S. Klemme, B. Moine, L. Barbero, R. Neu-

- mann, and G.A. Wagner. Alpha-recoil tracks in natural dark mica: Dating geological samples by optical and scanning force microscopy. *Nucl. Instr. and Meth. B*, 209:351–356, 2003.
- [GMCC⁺01] C. Gibert-Mougel, F. Couvreur, J.M. Costantini, S. Bouffard, F. Levesque, S. Hémon, E. Paumier, and C. Dufour. Phase transformation of polycrystalline zirconia induced by swift heavy ion irradiation. *J. Nucl. Mater.*, 295:121–125, 2001.
- [GMS89] A.F. Goncharov, I.N. Makarenko, and S.M. Stishov. Graphite at pressures up to 55 GPa: optical properties and raman scattering - amorphous carbon? *Sov. Phys. JETP*, 69:380–381, 1989.
- [Gög99] K. Gögen. Doctoral thesis, 1999.
- [GSMH99] A.F. Goncharov, V.V. Struzhkin, H.K. Mao, and R.J. Hemley. Raman spectroscopy of dense H₂O and the transition to symmetric hydrogen bonds. *Phys. Rev. Lett.*, 83:1998–2001, 1999.
- [GW00] K. Gögen and G.A. Wagner. Alpha-recoil track dating of quaternary volcanics. *Chem. Geol.*, 166:127–137, 2000.
- [HA98] R.J. Hemley and N.W. Ashcroft. The revealing role of pressure in the condensed-matter science. *Phys. Today*, 51:26–32, 1998.
- [HBL98] S. Habenicht, W. Bolse, and K.P. Lieb. A low-energy ion implanter for surface and material science. *Rev. Sci. Instr.*, 69:2120–2126, 1998.
- [HCD⁺97] S. Hémon, V. Chailley, E. Dooryhée, C. Dufour, F. Gourbilleau, F. Levesque, and E. Paumier. Phase transformation of polycrystalline Y₂O₃ under irradiation with swift heavy ions. *Nucl. Instr. and Meth. B*, 122:563–565, 1997.
- [Hem98] R.J. Hemley. *Ultrahigh-Pressure Mineralogy: Physics and Chemistry of the Earth's Deep Interior*. Mineralogical Society of America, Washington DC, 1998.
- [Hem00] R.J. Hemley. Effects of pressure on molecules. *Annu. Rev. Phys. Chem.*, 51:763–800, 2000.
- [HF78] R.M. Hazen and L.W. Finger. The crystal structures and compressibilities of layer minerals at high pressure. II. phlogopite and chloride. *Am. Mineral.*, 63:293–296, 1978.
- [HGA⁺94] T. Hagen, S. Grafström, J. Ackermann, R. Neumann, C. Trautmann, J. Vetter, and N. Angert. Friction force microscopy of heavy-ion irradiated mica. *J. Vac. Sci. Technol. B*, 12:1555–1558, 1994.
- [HH98] H.K. Mao and R.J. Hemley. New window on the earth's deep interior. In R.J. Hemley, editor, *Ultrahigh-Pressure Mineralogy: Physics and Chemistry of the Earth's Deep Interior*, volume 37 of *Rev. Mineral.*, chapter 1, pages 1–32. Mineralogical Society of America, Washington DC, 1998.

- [HI97] W.B. Holzapfel and N.S. Isaacs. *High-Pressure Techniques in Chemistry and Physics*. Oxford Univ. Press, Oxford, 1997.
- [HJM⁺88] R.J. Hemley, A.P. Jephcoat, H.K. Mao, L.C. Ming, and M.H. Manghnani. Pressure-induced amorphisation of crystalline silica. *Nature*, 334:52–54, 1988.
- [HK96] J.R. Hahn and H. Kang. STM study of Ar⁺ -induced defects produced by near-threshold energy collision. *Surf. Sci.*, 357-358:165–169, 1996.
- [HK99] J.R. Hahn and H. Kang. Vacancy and interstitial defects at graphite surfaces: Scanning tunneling microscopic study of the structure, electronic property, and yield for ion-induced defect creation. *Phys. Rev. B*, 60:6007–6017, 1999.
- [HKS90] M.D. Hou, S. Klaumünzer, and G. Schumacher. Dimensional changes of metallic glasses during bombardment with fast heavy ions: Dimensional changes of metallic glasses during bombardment with fast heavy ions. *Phys. Rev. B*, 41:1144–1157, 1990.
- [HM02] R.J. Hemley and H.K. Mao. Overview of static high pressure science. In R.J. Hemley, G.L. Chiarotti, M. Bernasconi, and L. Ulivi, editors, *High Pressure Phenomena*, number CXLVII in Proc. International School of Physics 'Enrico Fermi', pages 3–40, 2002.
- [HN98] S.R. Hashemi-Nezhad. The triangular track contours in phlogopite mica detectors and discontinuity of the etchable damage. *Nucl. Instr. and Meth. B*, 142:98–110, 1998.
- [HS89] M. Hanfland and K. Syassen. Optical reflectivity of graphite under pressure. *Phys. Rev. B*, 40:1951–1954, 1989.
- [HSHD98] H.K. Mao, G. Shen, R.J. Hemley, and T.S. Duffy. X-ray diffraction with a double hot-plate laser-heated diamond cell. In T. Yagi M.H. Manghnani, editor, *Properties of Earth and Planetary Materials at high Pressure and Temperature*, pages 27–34. Am. Geophys. Union, Washington D.C., 1998.
- [HSM91] D.L. Heinz, J.S. Sweeney, and P. Miller. A laser heating system that stabilizes and controls the temperature: Diamond anvil cell applications. *Rev. Sci. Instrum.*, 62:1568–1575, 1991.
- [HSPD00] V. Heera, W. Skorupa, B. Pécz, and L. Dobos. Ion beam synthesis of graphite and diamond in silicon carbide. *Appl. Phys. Lett.*, 76:2847–2849, 2000.
- [HSS80] T. Hashimoto, H. Sugiyama, and T. Sotobayashi. Alpha-recoil track formation on muscovite and measurement of recoil-range using ²⁵²Cf - sources. *Nucl. Tracks*, 4:263–269, 1980.
- [HTP98] R.K.W. Haselwimmer, A.W. Tyer, and E. Pugh. Millikelvin diamond anvil cell for the study of quantum critical phenomena. In M. Nakahara,

- editor, *Review of High Pressure Science and Technology*, volume 7, pages 481–483. Japan Society of High Pressure Science and Technology, Kyoto, 1998.
- [HW67] W.H. Huang and R.M. Walker. Fossil alpha-particle recoil tracks: a new method of age determination. *Science*, 155:1103–1106, 1967.
 - [IS01] N. Itoh and A.M. Stoneham. *Materials Modification by electronic Excitation*. Cambridge University Press, Cambridge, 2001.
 - [Jac54] I.S. Jacobs. Effect of pressure on f-center absorption in alkali halides. *Phys. Rev.*, 93:993–1004, 1954.
 - [Jac83] J.D. Jackson. *Klassische Elektrodynamik*. Walter de Gruyter Verlag, Berlin, 1983.
 - [Jay83] A. Jayaraman. Diamond-anvil cell and high pressure physical investigations. *Rev. Mod. Phys.*, 55:65–108, 1983.
 - [JK69] H.S. Yoder Jr. and I. Kushiro. Melting of a hydrous phase: phlogopite. *Am. J. Sci.*, 267:558–582, 1969.
 - [JKRB90] I. Jackson, S.K. Khanna, A. Revcolevschi, and J. Berthon. Elasticity, shear-mode softening and high-pressure polymorphism of wüstite (Fe_{1-x}O). *J. Geophys. Res.*, 95:21671–21685, 1990.
 - [JLBdJ00] W. Kindlein Jr., R.P. Livi, N.M. Balzaretti, and J.A.H. da Jornada. Effect of hydrogen implantation on the graphite used in high pressure diamond synthesis. *Diamond and Related Materials*, 9:22–25, 2000.
 - [JLN59] J.C. Jamieson, A.W. Lawson, and N.D. Nachtrieb. New device for obtaining x-ray diffraction patterns from substances exposed to high pressure. *Rev. Sci. Instrum.*, 30:1016–1019, 1959.
 - [KAR97] C. Koeberl, R.A Armstrong, and W.U. Reimold. A large impact structure of jurassic-cretaceous boundary age. *Geology*, 25:731–734, 1997.
 - [Kat69] S. Katcoff. Alpha-recoil tracks in mica: Registration efficiency. *Science*, 166:382–384, 1969.
 - [KBB⁺97] S. Klotz, J.M. Besson, M. Braden, K. Karch, P. Pavone, D. Strauch, and W.G. Marshall. Pressure induced frequency shifts of transverse acoustic phonons in germanium to 9.7 GPa. *Phys. Rev. Lett.*, 79:1313–1316, 1997.
 - [KCL⁺89] S. Klaumünzer, Li Changlin, S. Löffler, M. Rammensee, and G. Schumacher. Plastic flow of vitreous silica and pyrex during bombardment with fast heavy ions. *Nucl. Instr. and Meth. B*, 39:665–669, 1989.
 - [KGN⁺92] H. Kemmer, S. Grafström, M. Neitzert, M. Wörtge, R. Neumann, C. Trautmann, J. Vetter, and N. Angert. Scanning tunneling microscopy of surface modifications induced by UNILAC heavy-ion irradiation. *Ultramicroscopy*, 42-44:1345–1349, 1992.

- [KH77] R. Keller and W.B. Holzapfel. Diamond anvil device for x-ray diffraction on single crystals under pressures up to 100 kilobar. *Rev. Sci. Instrum.*, 48:517–523, 1977.
- [Kha86] H.A. Khan. Determination of charge (z) - and Z^β - threshold values for different glass and plastic track detectors. *Nucl. Tracks*, 12:337–340, 1986.
- [KHS86] S. Klaumünzer, M.D. Hou, and G. Schumacher. Coulomb explosions in a metallic glass due to the passage of fast heavy ions? *Phys. Rev. Lett.*, 57:850–853, 1986.
- [KK68] R. Katz and E.J. Kobetich. Formation of etchable tracks in dielectrics. *Phys. Rev.*, 170:401–405, 1968.
- [KK76] C.S. Kennedy and G.C. Kennedy. The equilibrium boundary between graphite. *J. Geophys. Res.*, 81:2467–2470, 1976.
- [KKR81] H.A. Khan, N.A. Khan, and R. Spohr. Scanning electron microscope analysis of etch pits obtained in a muscovite mica track detector by etching in hydrofluoric acid and aqueous solutions of naoh and KOH. *Nucl. Instr. and Meth. B*, 189:577–581, 1981.
- [KLT57] M.I. Kaganov, I.M. Lifshitz, and L.V. Tanatarov. Relaxiation between electrons and the lattice. *Sov. Phys. JETP*, 4:173–178, 1957.
- [KM71] N. Kawai and S. Mochizuki. Metallic states in the three 3d transition metal oxides, Fe_2O_3 , Cr_2O_3 and TiO_2 under static high pressures. *Phys. Lett. A*, 36:54–55, 1971.
- [KMH⁺03] Y. Koguchi, T. Meguro, A. Hida, H. Takai, K. Maeda, Y. Yamamoto, and Y. Aoyagi. Modification of highly oriented pyrolytic graphite (hopg) surfaces with highly charged ion (hci) irradiation. *Nucl. Instr. and Meth. B*, 206:202–205, 2003.
- [KS83] S. Klaumünzer and G. Schumacher. Dramatic growth of glassy $\text{Pd}_{80}\text{Si}_{20}$ during heavy-ion irradiation. *Phys. Rev. Lett.*, 51:1987–1990, 1983.
- [KSKF85] K. Kusaba, Y. Syono, M. Kikuchi, and K. Fukuoka. Shock behavior of zircon: Phase transition to scheelite structure and decompression. *Earth. Planet. Sci. Lett.*, 72:433–439, 1985.
- [KW93] E. Knittel and Q. Williams. High-pressure raman spectroscopy of ZrSiO_4 : Observation of the zircon to scheelite transition at 300 k. *Am. Mineral.*, 78:245–252, 1993.
- [KYA67] I. Kushiro, Y. Syono, and S. Akimoto. Stability of phlogopite and possible presence of phlogopite in the earth’s upper mantle. *Earth. Planet. Sci. Lett.*, 3:197–203, 1967.
- [Lan01] M. Lang. Diploma thesis, 2001.
- [LD93] D. Lesueur and A. Dunlop. Damage creation via electronic excitations in

- metallic targets part ii, a theoretical model. *Rad. Eff. Def. Sol.*, 126:163–172, 1993.
- [Le002] *Taking thin diamonds to their limit: Coupling static-compression and laser-shock techniques to generate dense water*, volume 620, 2002.
- [Ley01] L. Ley. Werkstoff mit zukunft: Diamantsynthese aus der gasphase. *Physik in unserer Zeit*, 5:212–219, 2001.
- [LGM⁺02a] M. Lang, U.A. Glasmacher, B. Moine, C. Müller, R. Neumann, and G.A. Wagner. Artificial ion tracks in volcanic dark mica simulating natural radiation damage: A scanning force microscopy study. *Nucl. Instr. and Meth. B*, 191:346–351, 2002.
- [LGM⁺02b] M. Lang, U.A. Glasmacher, B. Moine, C. Müller, R. Neumann, and G.A. Wagner. Heavy-ion induced defects in phlogopite imaged by scanning force microscopy. *Surf. Coat. Technol.*, 158-159:439–443, 2002.
- [LGNW03] M. Lang, U.A. Glasmacher, R. Neumann, and G.A. Wagner. Etching behaviour of alpha-recoil tracks in natural dark mica studied via artificial ion tracks. *Nucl. Instr. and Meth. B*, 209:357–361, 2003.
- [LHT⁺03] J. Liu, M.D. Hou, C. Trautmann, R. Neumann, C. Müller, Z.G. Wang, Q.X. Zhang, Y.M. Sun, Y.F. Jin, H.W. Liu, and H.J. Gao. STM and raman spectroscopic study of graphite irradiated by heavy ions. *Nucl. Instr. and Meth. B*, 212:303–307, 2003.
- [Liu79] L.G. Liu. High-pressure phase transformations in baddeleyite and zircon, with geophysical implications. *Earth. Planet. Sci. Lett.*, 44:390–396, 1979.
- [LKM⁺94] T. Li, B.V. King, R.J. MacDonald, G.F. Gotterill, D.J. O'Connor, and Q. Yang. STM study of the effects of the ion incident angle and energy on surface damage induced by Ar⁺ bombardment of HOPG. *Surf. Sci.*, 312:399–410, 1994.
- [Llo64] Lloyd, editor. *Specific volume measurements of crystalline solids at pressures up to 200 kilobars by x-ray diffraction*, 1964.
- [LLW98] B. Li, R.C. Liebermann, and D.J. Weidner. Elastic moduli of wadsleyite (beta – Mg₂SiO₄) to 7 gigapascal and 873 kelvin. *Science*, 281:675–677, 1998.
- [LNTM01] J. Liu, R. Neumann, C. Trautmann, and C. Müller. Tracks of swift heavy ions in graphite studied by scanning tunneling microscopy. *Phys. Rev. B*, 64:184115 1–7, 2001.
- [LSM98] F. Langenhorst, G. Shafranovsky, and V.L. Masaitis. A comparative study of impact diamonds from the popigai, ries, sudbury, and lappajarvi craters. *Meteoritics and Planet. Sciences*, 33:A90–A91, 1998.
- [MA77] M.H. Manghnani and S. Akimoto, editors. *High Pressure Research - Applications in Geophysics*, New York, 1977. Academic Press.

- [MB72] P.J. Modreski and A.L. Boettcher. The stability of phlogopite + enstatite at high pressures: A model for micas in the interior of the earth. *Am. J. Sci.*, 272:385–414, 1972.
- [MB73] P.J. Modreski and A.L. Boettcher. Phase relationships of phlogopite in the system K₂O – MgO – CaO – Al₂O₃ – SiO₂ – H₂O to 35 kilobars: A better model for micas in the interior of the earth. *Am. J. Sci.*, 272:852–869, 1973.
- [MB74a] L. Merrill and W.A. Bassett. Miniature diamond anvil pressure cell for single-crystal x-ray diffraction studies. *Rev. Sci. Instrum.*, 45:290–294, 1974.
- [MB74b] L.C. Ming and W.A. Bassett. Laser heating in the diamond anvil press up to 2000°C sustained and 3000°C pulsed at pressures up to 260 kilobars. *Rev. Sci. Instrum.*, 45:1115–1118, 1974.
- [MB75] H.K. Mao and P.M. Bell. Design of a diamond-windowed, high-pressure cell for hydrostatic pressures in the range 1 bar to 0.5 mbar. *Carnegie Inst. Washington Yearb.*, 74:402–405, 1975.
- [MB76] H.K. Mao and P.M. Bell. High-pressure physics: the 1-megabar mark on the ruby R₁ static pressure scale. *Science*, 191:851–852, 1976.
- [MB78] H.K. Mao and P.M. Bell. High-pressure physics: sustained static generation to 1.36 to 1.72 megabars. *Science*, 200:1145–1147, 1978.
- [MBB⁺95] D. Marton, H. Bu, K.J. Boyd, S.S. Todorov, A.H. Al-Bayati, and J.W. Rabalais. On the defect structure due to low energy ion bombardement of graphite. *Surf. Sci.*, 326:489–493, 1995.
- [MBC⁺93] Meftah, F. Brisard, J.M. Costantini, M. Hage-Ali, J.P. Stoquert, F. Studer, and M. Toulemonde. Swift heavy ions in magnetic insulators : A damage cross section velocity effect. *Phys. Rev. Lett. B*, 48:920–925, 1993.
- [MLBR93] D. Marton, K.J. Boyd, T. Lytle, and J.W. Rabalais. Near threshold ion induced defect production in graphite. *Phys. Rev. B*, 48:6757–6766, 1993.
- [MBSS78] H.K. Mao, P.M. Bell, J.W. Shaner, and D.J. Steinberg. Specific volume measurements of cu, mo, pd, and ag and calibration of the ruby R₁ fluorescence pressure gauge from 0.06 to 1 mbar. *J. Appl. Phys.*, 49:3276–3283, 1978.
- [McM02] P.F. McMillan. New materials from high-pressure experiments. *Nature Materials*, 1:19–25, 2002.
- [MCS93] F. Moshary, N.H. Chen, and I.F. Silvera. Remarkable high pressure phase line of orientational order in solid hydrogen deuteride. *Phys. Rev. Lett.*, 71:3814–3817, 1993.
- [MDK00] R. Miletich, R.A. David, and W.F. Kuhs. High-pressure single-crystal

- techniques. In R.T. Downs R.M. Hazen, editor, *High-Temperature and High-Pressure Crystal Chemistry*, volume 41 of *Reviews in Mineralogy and Geochemistry*, pages 445–519. Mineralogical Society of American Geochemical Society, 2000.
- [MGM⁺00] S. Merkel, A.F. Goncharov, H.K. Mao, P. Gillet, and R.J. Hemley. Raman spectroscopy of iron to 152 gigapascals: Implications for earth’s inner core. *Science*, 288:1626–1629, 2000.
- [MH96] H.K. Mao and R.J. Hemley. Energy dispersive x-ray diffraction of micro-crystals at ultrahigh pressures. *High Press. Res.*, 14:257–267, 1996.
- [MHAS⁺93] A. Meftah, M. Hage-Ali, J.P. Stoquert, F. Studer, and M. Toulemonde. Electronic stopping power threshold of damage creation in yttrium garnet. *Radiat. Eff. Def. Solids*, 126:251–254, 1993.
- [MHK⁺03] T. Meguro, A. Hida, Y. Koguchi, S. Miyamoto, Y. Yamamoto, H. Takai, K. Maeda, and Y. Aoyagi. Nanoscale transformation of sp² to sp³ of graphite by slow highly charged ion irradiation. *Nucl. Instr. and Meth. B*, 209:170–174, 2003.
- [MIO75] H. Maeta, T. Iwata, and S. Okuda. c-axis spacing changes in pyrolytic graphite after neutron irradiation at 5K. *J. Phys. Soc. Jpn.*, 39:1558–1565, 1975.
- [Mit95] R.H. Mitchell. Melting experiments on a sanidine phlogopite lamproite at 4–7 GPa and their bearing on the source of lamproitic magmas. *J. Petrol.*, 36:1455–1474, 1995.
- [MKK83] V.K. Milinchuk, E.R. Klinshpont, and V.P. Kiryukhin. Effect of high pressure on the formation and reactions of free radicals in the radiolysis of polymers. *Radiat. Phys. Chem.*, 21:519–526, 1983.
- [MKK86] V.K. Milinchuk, E.R. Klinshpont, and V.P. Kiryukhin. Radiation effects in polymers at high pressure. *Radiat. Phys. Chem.*, 28:331–334, 1986.
- [MLMH70] M.Lambert, A.-M. Levelut, M. Maurette, and H. Heckman. Small angle x-ray scattering study of muscovite mica irradiated by argon ions. *Radiat. Eff.*, 3:155–160, 1970.
- [MMB87] L.C. Ming, M.H. Manghnani, and J. Balogh. Resistive heating in the diamond-anvil cell under vacuum conditions. In M.H. Manghnani and Y. Syono, editors, *High-Pressure Research in Mineral Physics*, pages 69–74. Am. Geophys. Union, Washington D.C., 1987.
- [MME⁺03] W.L. Mao, H.K. Mao, P.J. Eng, T.P. Trainor, M. Newville, C.C. Kao, D.L. Heinz, J. Shu, Y. Meng, and R.J. Hemley. Bonding changes in compressed superhard graphite. *Science*, 302:425–427, 2003.
- [MNB97] E.D. Miller, D.C. Nesting, and J.V. Badding. Quenchable transparent phase of carbon. *Chem. Mat.*, 9:18–22, 1997.

- [MSF⁺96] T. Matsukawa, S. Suzuki, T. Fukai, T. Tanaka, and I. Ohdomari. STM observation of craters on graphite surface induced by single ion implantation. *Appl. Surf. Sci.*, 107:227–232, 1996.
- [MWC⁺90] H.K. Mao, Y. Wu, L.C. Chen, J.F. Shu, and A.P. Jephcoat. Static compression of iron to 300 GPa and Fe_{0.8}Ni_{0.2} alloy to 260 GPa: Implications for composition of the core. *J. Geophys. Res.*, 95:21737–21742, 1990.
- [MXB86] H.K. Mao, J.A. Xu, and P.M. Bell. Calibration of the ruby gauge to 800 kbar under quasihydrostatic conditions. *J. Geophys. Res. B*, 91:4673–4676, 1986.
- [NAA⁺96] R. Neumann, J. Ackermann, N. Angert, C. Trautmann, M. Dischner, T. Hagen, and M. Sedlacek. Ion tracks in mica studied with scanning force microscopy using force modulation. *Nucl. Instr. and Meth. B*, 116:492–495, 1996.
- [Nel02] W.J. Nellis. Dynamic experiments: An overview. In R.J. Hemley, G.L. Chiarotti, M. Bernasconi, and L. Ulivi, editors, *High Pressure Phenomena*, number CXLVII in Proc. International School of Physics 'Enrico Fermi', pages 109–126, 2002.
- [NM94] R.J. Nelmes and M.I. McMahon. High-pressure powder diffraction on synchrotron sources. *J. Synchrotron Rad.*, 1:69–73, 1994.
- [NMH⁺92] R.J. Nelmes, M.I. McMahon, P.D. Hatton, R.O. Piltz, J. Crain, R.J. Cernik, and G. Bushnell-Wye. Angle-dispersive powder diffraction at high pressure using an image-plate area detector. *High Pressure Res.*, 8:677–684, 1992.
- [OFN⁺04] S. Ono, K. Funakoshi, Y. Nakajima, Y. Tange, and T. Katsura. Phase transition of zircon at high p-t conditions. *Contrib. Mineral. Petrol.*, 147:505–509, 2004.
- [OGJ99] J.S. Olsen, L. Gerward, and J.Z. Jiang. On the rutile/ α – pb₂ -type phase boundary of TiO₂. *J. Phys. Chem. Solids*, 60:229–233, 1999.
- [OPJ⁺01] J.O. Orwa, S. Prawer, D.N. Jamieson, J.L. Peng, J.C. McCallum, K.W. Nugent, Y.J. Li, and L.A. Bursill. Diamond nanocrystals formed by direct implantation of fused silica with carbon. *J. Appl. Phys.*, 90:3007–3018, 2001.
- [PBB75] G.J. Piermarini, S. Block, and J.D. Barnett. Calibration of the R₁ ruby fluorescence line to 195 kbar. *J. Appl. Phys.*, 46:2774–2780, 1975.
- [PdVP91] L. Porte, C.H. de Villeneuve, and M. Phaner. Scanning tunneling microscopy observation of local damages induced on graphite surface by ion implantation. *Vac. Sci. B*, 9:1064–1067, 1991.
- [Pea30] T.J. Pearsall. On the effects of electricity upon minerals which are phosphorescent by heat. *J. Royal Inst.*, 1:77, 1830.

- [PPdV⁺89] L. Porte, M. Phaner, C.H. de Villeneuve, N. Moncoffre, and J. Tousset. Scanning tunneling microscopy study of single-ion impacts on graphite surface. *Nucl. Instr. and Meth. B*, 44:116–119, 1989.
- [Prz56] K. Przibram. *Irradiation colors and luminescence*. Pergamon Press, London, 1956.
- [PVWJ01] J.R. Patterson, Y.K. Vohra, S.T. Weir, and J. Akella. Single-wall carbon nanotubes under high pressures to 62 GPa studied using designer diamond anvils. *J. Nanosci. Nanotechnol.*, 1:143–147, 2001.
- [PW62] P.B. Price and R.M. Walker. Electron microscope observation of etched tracks from spallation recoils in mica. *Phys. Rev. Lett.*, 8:217–219, 1962.
- [PW63] P.B. Price and R.M. Walker. Fossil tracks of charged particles in mica and the age of the mineral. *J. Geophys. Res.*, 68:4847–4862, 1963.
- [RBGL95] K.P. Reimann, W. Bolse, U. Geyer, and K.P. Lieb. Atomically resolved imaging of the defect structure on graphite after oblique single-ion impact. *Europhys. Lett.*, 30:463–468, 1995.
- [RBLA98] Ph. Redlich, F. Banhart, Y. Lyutovich, and P.M. Ajayan. EELS study of the irradiation-induced compression of carbon onions and their transformation to diamond. *Carbon*, 36:561–563, 1998.
- [RC82] R.H. Ritchie and C. Claussen. A core plasma model of charged particle track formation in insulators. *Nucl. Instr. and Meth. B*, 198:133–138, 1982.
- [RG99] R. L. Russell and S. Guggenheim. Crystal structures of near-end-member phlogopite at high temperature and heat treated fe-rich phlogopite: the influence of the o,oh,f site. *Can. Mineral.*, 37:711–720, 1999.
- [RR69] A.F. Reid and A.E. Ringwood. Newly observed high pressure transformations in Mn_3O_4 , $CaAl_2O_4$ and $ZrSiO_4$. *Earth. Planet. Sci. Lett.*, 6:205–208, 1969.
- [SAS89] R. Spohr, P. Armbruster, and K. Schaupert. Structure and diffusion properties of latent ion tracks. *Radiat. Eff. Def. Solids*, 110:27–31, 1989.
- [SB59] E.C.H. Silk and R.S. Barnes. Examination of fission fragment tracks with an electron microscope. *Philos. Mag.*, 7:970–972, 1959.
- [SB76] C. Sung and R.G. Burns. Kinetics of the olivine to spinel transition: Implications to deep-focus earthquake genesis. *Earth Planet. Sci. Lett.*, 32:165–170, 1976.
- [SB94] P. Stampfli and K.H. Bennemann. Time dependence of the laser-induced femtosecond lattice instability of si and gaas: Role of longitudinal optical distortions. *Phys. Rev. B*, 49:7299–7305, 1994.
- [SBC92] A.H. Shen, W.A. Bassett, and I.M. Chou. Hydrothermal studies in a diamond anvil cell: pressure determination using the equation of state. In

- Y. Syono and M.H. Manghnani, editors, *High-pressure research: application to earth and planetary sciences*, pages 61–68. American Geophysical Union, 1992.
- [SBL⁺01] S.R.S. Soares, N.M. Balzaretti, R.L. Livi, A.S. Pereira, and J.A.H. da Jornada. High pressure annealing of defects induced by ion implantation on graphite. *Nucl. Instr. and Meth. B*, 175-177:474–478, 2001.
- [Sch94] C. Scheidenberger. Doctoral thesis, 1994.
- [SCN⁺98] Y.D. Sinelnikov, G. Chen, D.R. Neuville, M.T. Vaughan, and R.C. Liebermann. Ultrasonic shear wave velocities of MgSiO₃ perovskite at 8 GPa and 800 k and lower mantle composition. *Science*, 281:677–679, 1998.
- [SFY90] S. Saito, O. Fukunaga, and M. Yoshikawa, editors. *Science and Technology of New Diamond*, Tokyo, 1990. KTK Scientific Publishers/ Terra Scientific Publishing Company.
- [SGM⁺00] V.V. Struzhkin, A.F. Goncharov, H.K. Mao, R.J. Hemley, S.W. Moore, J.M. Graybeal, J. Sarrao, and Z.Fisk. Coupled magnon-phonon excitations in Sr₂CuCl₂O₂ at high pressure. *Phys. Rev. B*, 62:3895–3899, 2000.
- [Sha77] S.K. Sharma. Laser-raman spectroscopy. *Carnegie Inst. Wash. Yrbk*, pages 902–904, 1977.
- [She84] W.F. Sherman. Infrared and raman spectroscopy at high pressures. *J. Molec. Struct.*, 113:101–116, 1984.
- [SIC95] D.P. Snowden-Ifft and M.K.Y. Chan. A new track etch model for mica. *Nucl. Instr. and Meth. B*, 101:247–251, 1995.
- [Sim65] J.H.W. Simmons. *Radiation damage in Graphite*. Pergamon, Oxford, 1965.
- [SjBVD88] G. Shi-jun, R. Brandt, P. Vater, and R. Dersch. Study of size distribution and elemental composition of environmental aerosols with nuclear track microfilters, electron microscope and electron microprobe. *Nucl. Tracks and Radiat. Meas.*, 15:751, 1988.
- [SKF⁺01] K. Shimizu, T. Kimura, S. Furomoto, K. Takeda, K. Kontani, Y. Onuki, and K. Amaya. Superconductivity in the non-magnetic state of iron under pressure. *Nature*, 412:316–318, 2001.
- [SKI97] K. Sato, T. Katsura, and E. Ito. Phase relations of natural phlogopite with and without enstatite up to 8 GPa: implication for mantle metasomatism. *Earth Planet. Sci. Lett.*, 146:511–526, 1997.
- [SKT⁺97] T. Seki, T. Kaneko, D. Takeuchi, T. Aoki, J. Matsuo, Z. Insepov, and I. Yamada. STM observation of HOPG surfaces irradiated with ar cluster ions. *Nucl. Instr. and Meth. B*, 121:498–502, 1997.

- [SLXG01] G. Schiwietz, E. Luderer, G. Xiao, and P.L. Grande. Energy dissipation of fast heavy ions in matter. *Nucl. Instr. and Meth. B*, 175-177:1–11, 2001.
- [Spo80] R. Spohr. Nuclear tracks irradiated at GSI. *Nucl. Tracks*, 4:101–104, 1980.
- [SRWS00] G. Shen, M.L. Rivers, Y. Wang, and S.R. Sutton. Laser heated diamond cell system at the advanced photon source for in situ x-ray measurements at high pressure and temperature. *Rev. Sci. Instrum.*, 72:1273–1282, 2000.
- [SS95] A.P. Sharma S.K. Sharma, S. Kumar. Stopping power of heavy ions in solids: A comparative study. *Appl. Radiat. Isot.*, 46:39–52, 1995.
- [ST90] A. Sudo and Y. Tatsumi. Phlogopite and k-amphibole in the upper mantle: Implication for magma genesis in the subduction zones. *Geophys. Res. Lett.*, 17:29–32, 1990.
- [Sta96] P. Stampfli. Electronic excitation and structural stability of solids. *Nucl. Instr. and Meth. B*, 107:138–145, 1996.
- [STF⁺92] O. Shimomura, K. Takemura, H. Fujihisa, Y. Fujii, Y. Ohishi, T. Kikegawa, Y. Amemiya, and T. Matsushita. Application of an imaging plate to high-pressure x-ray study with a diamond anvil cell. *Rev. Sci. Instrum.*, 63:967–973, 1992.
- [STK00] J.P. Singh, A. Tripathi, and D. Kanjilal. In situ STM studies of HOPG surface after 200 mev Au⁺¹³ ionirradiation. *Vacuum*, 57:319–325, 2000.
- [STN03] K. Schwartz, C. Trautmann, and R. Neumann. Electronic excitations and heavy-ion-induced processes in ionic crystals. *Nucl. Instr. and Meth. B*, 209:73–84, 2003.
- [Sun76] C.M. Sung. New modification of the diamond anvil press: A versatile apparatus for research at high pressure and high temperature. *Rev. Sci. Instrum.*, 47:1343–1346, 1976.
- [Sun00] J. Sung. Graphite to diamond transition under high pressure: A kinetics approach. *J. Mater. Sci.*, 35:6041–6054, 2000.
- [SWCP95] E. Snoeks, T. Weber, A. Cacciato, and A. Polman. Mev ion irradiation-induced creation and relaxation of mechanical stress in silica. *J. Appl. Phys.*, 78:4723–4732, 1995.
- [Sze96] G. Szenes. Thermal spike model of amorphous track formation in insulators irradiated by swift heavy ions. *Nucl. Instr. and Meth. B*, 116:141–144, 1996.
- [TBS94] M. Toulemonde, S. Bouffard, and F. Studer. Swift heavy ions in insulating and conducting oxides: tracks and physical properties. *Nucl. Instr. and Meth. B*, 91:108–123, 1994.

- [TCBB91] F. Thibaudau, J. Cousty, E. Balanzat, and S. Bouffard. Atomic-force-microscopy observations of tracks induced by swift kr ions in mica. *Phys. Rev. Lett.*, 67:1582–1585, 1991.
- [TCCL78] R.P. Tripathi, U. Chandra, R. Chandra, and S. Lokanathan. A mössbauer study of the effects of heating biotite, phlogopite and vermiculite. *J. Inorg. Nucl. Chem.*, 40:1293–1298, 1978.
- [TCD⁺96] M. Toulemonde, J.M. Costantini, C. Dufour, A. Meftah, E. Paumier, and F. Studer. Track creation in SiO_2 and $\text{BaFe}_{12}\text{O}_{19}$ by swift heavy ions: a thermal spike description. *Nucl. Instr. and Meth. B*, 116:37–42, 1996.
- [TCM⁺97] C. Trautmann, J.M. Costantini, A. Meftah, K. Schwartz, J.P Stoquert, and M. Toulemonde. Swelling of SiO_2 induced by energetic heavy ions. In *Atomistic Mechanisms in Beam Synthesis and Irradiation of Materials*, pages 123–128. Materials Research Society, Warrendale, Pennsylvania, 1997.
- [TDMP00] M. Toulemonde, C. Dufour, A. Meftah, and E. Paumier. Transient thermal processes in heavy ion irradiation of crystalline inorganic insulators. *Nucl. Instr. and Meth. B*, 166-167:903–912, 2000.
- [TDN00] F. Tutti, L.S. Dubrovinski, and M. Nygren. High-temperature study and thermal expansion of phlogopite. *Phys. Chem. Minerals.*, 27:599–603, 2000.
- [TDWP96] M. Toulemonde, Ch. Dufour, Z.G. Wang, and E. Paumier. Atomic and cluster ion bombardment in the electronic stopping power regime: A thermal spike description. *Nucl. Instr. and Meth. B*, 112:26–29, 1996.
- [TE94] J. Tang and S. Endo. X-ray study of the transitions among the rutile, $\alpha - \text{pbo}_2$ and baddeleyite phases of TiO_2 at high pressure and high temperature. In *High-pressure science and technology*, pages 367–370. American Institute of Physics, 1994.
- [TE01] T. Turowski and W. Enge. Ionizing particles may create shockwaves. *Radiat. Meas.*, 34:27–30, 2001.
- [TKT00] C. Trautmann, S. Klaumünzer, and H. Trinkaus. Effect of stress on track formation in amorphous iron boron alloy: Ion tracks as elastic inclusions. *Phys. Rev. Lett.*, 85:3648–3651, 2000.
- [TM75] H. Takeda and B. Morosin. Comparison of observed and predicted structural parameters of mica at high temperature. *Acta. Crystallogr.*, B31:2444–2452, 1975.
- [TR95] H. Trinkaus and A.I. Ryazanov. Viscoelastic model for the plastic flow of amorphous solids under energetic ion bombardment. *Phys. Rev. Lett.*, 74:5072–5075, 1995.
- [TRE⁺96] K. Tinschert, D. M. Rück, H. Emig, K. Leible, and N. Angert. Ion

- irradiation facility for materials research at the 1.4 mev/u high-charge state injector of GSI. *Nucl. Instr. and Meth. B*, 113:59–63, 1996.
- [Tri95] H. Trinkaus. Local stress relaxation in thermal spikes as a possible cause for creep and macroscopic stress relaxation of amorphous solids under irradiation. *J. Nucl. Mater.*, 223:196–201, 1995.
- [Tri96] H. Trinkaus. Anisotropic creep and growth of amorphous solids under swift heavy ion bombardment: An asymptotic thermal spike approach. *Nucl. Instr. and Meth. B*, 107:155–159, 1996.
- [Tri98] H. Trinkaus. Dynamics of viscoelastic flow in ion tracks: origin of plastic deformation of amorphous materials. *Nucl. Instr. and Meth. B*, 146:204–216, 1998.
- [TSH⁺02] Y.A. Timofeev, V.V. Struzhkin, R.J. Hemley, H.K. Mao, and E.A. Gregoryanz. Improved techniques for measurement of superconductivity in diamond anvil cells by magnetic susceptibility. *Rev. Sci. Instrum.*, 73:371–377, 2002.
- [TT04] Y. Tange and E. Takahashi. Stability of zircon at high-pressure and temperature. *Review of High Pressure Science and Technology*, 12:50, 2004.
- [TTS86] R.G. Tronnes, E. Takahashi, and C.M. Scarfe. Stability of k-richterite and phlogopite to 14 GPa. *EOS Trans. AGU*, 69:1510–1511, 1986.
- [Uga92] D. Ugarte. Curling and closure of graphitic networks under electron beam irradiation. *Nature*, 359:707–708, 1992.
- [UY91] W. Utsumi and T. Yagi. Light-transparent phase formed by room-temperature compression of graphite. *Science*, 252:1542–1544, 1991.
- [VB96] A.E. Volkov and V.A. Borodin. The rate of the electron-ion heat transfer in swift heavy particle tracks in metals. *Nucl. Instr. and Meth. B*, 107:172–174, 1996.
- [VDBR88] Y.K. Vohra, S.J. Duclos, K.E. Brister, and A.L. Ruoff. Static pressure of 255 GPa (2.55 mbar) by x-ray diffraction: comparison with extrapolation of the ruby pressure scale. *Phys. Rev. Lett.*, 61:574–577, 1988.
- [vG00] N. von Grabczewski. Diploma thesis, 2000.
- [VGR⁺00] F. Villa, M. Grivet, M. Rebetez, C. Dubois, A. Chambaudet, N. Chevarier, G. Blondiaux, T. Sauvage, and M. Toulemonde. Damage morphology of kr ion tracks in apatite: Dependence on thermal annealing. *Nucl. Instr. and Meth. B*, 168:72–77, 2000.
- [VSDN98] J. Vetter, R. Scholz, D. Dobrev, and L. Nistor. HREM investigations of latent tracks in ges and mica induced by high energy ions. *Nucl. Instr. and Meth. B*, 141:747–752, 1998.
- [VW02] Y.K. Vohra and S.T Weir. Designer diamond anvils in high pressure re-

- search: Recent results and future opportunities. In R.J. Hemley, G.L. Chiarotti, M. Bernasconi, and L. Ulivi, editors, *High Pressure Phenomena*, number CXLVII in Proc. International School of Physics 'Enrico Fermi', pages 87–105, 2002.
- [vWFH⁺04] W. van Westrenen, M. R. Frank, J. M. Hanchar, Y. Fei, R. J. Finch, and C.-S. Zha. In situ determination of the compressibility of synthetic pure zircon (ZrSiO_4) and the onset of the zircon-reidite phase transition. *Am. Mineral.*, 89:197–203, 2004.
- [WAAR⁺00] S.T. Weir, J. Akella, C. Aracne-Ruddle, Y.K. Vohra, and S.A. Catledge. Epitaxial diamond encapsulation of metal microprobes for high pressure experiments. *Appl. Phys. Lett.*, 77:3400–3402, 2000.
- [WdH92] G.A. Wagner and P. Van den Haute. *Fission-track dating*. Ferdinand Enke Verlag, Stuttgart, 1992.
- [WDPT94] Z.G. Wang, Ch. Dufour, E. Paumier, and M. Toulemonde. The S_e sensitivity of metals under swift-heavy-ion irradiation: a transient thermal process. *J. Phys. Condens. Matter*, 6:6733–6750, 1994.
- [WE80] R.F. Wendlandt and D.H. Eggler. The origins of potassic magmas: stability of phlogopite in natural spinel iherzolite and in the system $\text{KAlSiO}_4 - \text{MgO} - \text{SiO}_2 - \text{H}_2\text{O} - \text{CO}_2$ at high pressures and high temperatures. *Am. J. Sci.*, 280:421–458, 1980.
- [Wei01] H. Weick. Doctoral thesis, 2001.
- [WEZ03] A.C. Withers, E.J. Essene, and Y. Zhang. Rutile/ TiO_2 ii phase equilibria. *Contrib. Mineral. Petrol.*, 145:199–204, 2003.
- [WGS⁺04] R. Weinstein, A. Gandini, R.-P. Sawh, B. Mayes, and D. Parks. Experimental test of the postulate that continuous columnar pinning centers produce the highest J_c ., *Phys. Lett.*, page in print, 2004.
- [Win02] R. Winter. High pressure effects in molecular biophysics. In R.J. Hemley, G.L. Chiarotti, M. Bernasconi, and L. Ulivi, editors, *High Pressure Phenomena*, number CXLVII in Proc. International School of Physics 'Enrico Fermi', pages 413–453, 2002.
- [WLB⁺97] P. Wesolowski, Y. Lyutovich, F. Banhart, H.D. Carstanjen, and H. Kronmuller. Formation of diamond in carbon onions under mev ion irradiation. *Appl. Phys. Lett.*, 71:1948–1950, 1997.
- [WLVB59] C.E. Weir, E.R. Lippincott, A. van Valkenburg, and E.N. Bunting. Infrared studies in the 1-to 15-micron region to 30,000 atmospheres. *J. Res. Natl. Bur. Stand. (U.S.)*, 63A:55–62, 1959.
- [WT85] C.C. Watson and T.A. Tombrello. A modified lattice potential model of electronically mediated sputtering. *Radiat. Eff.*, 89:263–283, 1985.
- [WVC02] A.S. Wendt, O. Vidal, and L.T. Chadderton. Experimental evidence

- for the pressure dependence of fission track annealing in apatite. *Earth Planet. Sci. Lett.*, 201:593–607, 2002.
- [WWE00] S.X. Wang, L.M. Wang, and R.C. Ewing. Irradiation-induced amorphization: Effects of temperature, ion mass, cascade size, and dose rate. *Phys. Rev. B*, 63:024105, 2000.
- [WWM98] Y. Wang, D.J. Weidner, and Y. Meng. Advances in equation-of-state measurements in sam-85. In M.H. Manghnani and T. Yagi, editors, *Properties of Earth and Planetary Materials at High Pressure and Temperature*, pages 365–372. AGU, Washington, D.C., 1998.
- [YLB⁺94] J. Yan, Z. Li, C. Bai, W.S. Yang, Y. Wang, W. Zhao, Y. Kang, F.C. Yu, P. Zhai, and X. Tang. Scanning tunneling microscopy investigation of graphite surface damage induced by gold-ion bombardment. *J. Appl. Phys.*, 75:1390–1395, 1994.
- [YTS03] K. Yamada, T. Tagami, and N. Shimobayashi. Experimental study on hydrothermal annealing of fission tracks in zircon. *Chem. Geol.*, 201:351–357, 2003.
- [YUY⁺92] T. Yagi, W. Utsumi, M. Yamakata, T. Kikegawa, and O. Shimomura. High-pressure in situ x-ray-diffraction study of the phase transformation from graphite to hexagonal diamond at room temperature. *Phys. Rev. B*, 46:6031–6039, 1992.
- [ZB97] M. Zaiser and F. Banhart. Radiation-induced transformation of graphite to diamond. *Phys. Rev. Lett.*, 79:3680–3683, 1997.
- [ZB99a] J.F. Ziegler and J.P. Biersack. *The stopping and the Range of Ions in Matter-SRIM-2000.39*, 1999.
- [ZB99b] J.F. Ziegler and J.P. Biersack. *The stopping and the Range of Ions in Matter-SRIM-2003.20*, 1999.
- [ZBS96] M.S. Zwanger, F. Banhart, and A. Seeger. The formation and decay of concentric-shell carbon clusters. *J. Crystal Growth*, 163:445–454, 1996.
- [ZLB00] M. Zaiser, Y. Lyutovich, and F. Banhart. Irradiation-induced transformation of graphite to diamond: A quantitative study. *Phys. Rev. B*, 62:3058–3064, 2000.
- [ZS89] Y. Zhao and I. L. Spain. X-ray diffraction data for graphite to 20 GPa. *Phys. Rev. B*, 40:993–997, 1989.
- [ZZC94] Y. Zhang, F. Zhang, and G. Chen. A study of phase transformation between diamond and graphite in p-t diagram of carbon. *Carbon*, 32:1415–1418, 1994.

Acknowledgement

First of all, I want to thank Prof. R. Neumann, the supervisor of my doctoral work. He gave me the opportunity to perform this interesting research in his group and made it possible for me to attend courses and conferences. During many discussions, I learnt much from him, not only in physics. He supported me throughout the practical work such as beam times, spent much time for the corrections of papers, and helped me to improve the English of this dissertation.

I would like to express my sincere thanks also to all the other people who have contributed to this work. I am indebted to (in alphabetical order)...

...Dr. J. Baier and Dr. A. Audetat for teaching me the DAC-filling procedure and for their support during my own fillings.

...B. Binder and A. Dorn for the Raman measurements.

...Dr. sc. D. Dobrev for the help with the REM and many discussions.

...PD Dr. U.A. Glasmacher for strongly supporting me during my doctoral work by many motivating discussions and by practical help during beam times. He also gave me the opportunity to travel to interesting conferences. Furthermore, he corrected my thesis draft and supported me with the preparation of a manuscript that was helpful to me when writing the thesis.

...Prof. O. Greulich for intensive discussions about the scientific work of a physicist in general, the discussions about the Palatinate, and his encouraging words.

...Prof. H. Keppler for providing us with diamond anvil cells for irradiations. He prepared most of the high-pressure cells and gave me the opportunity to visit his institute in Tübingen in order to introduce me into the procedure of DAC-filling. Additionally, most of the Raman investigations have been performed by his group members. Furthermore, he prepared a manuscript from which I benefitted for the text of the thesis.

...PD Dr. Langenhorst for the TEM measurements. I appreciated the fruitful discussions during his stays in Heidelberg and for looking through the thesis draft.

...Prof. R. Miletich for interesting discussions and for the corrections he proposed for the dissertation from a mineralogist's point of view.

...Dipl.-Ing. T. Schäfer for doing the hard job of converting my thesis manuscript from Microsoft-Word© to L^AT_EX.

...Dr. D. Schardt for the irradiations of all DACs. He was the supervisor of cave A and helped us during all beam times even at midnight or on Sundays. He spent a lot of time in preparing the set-up for DAC-irradiations. Furthermore, he intensively corrected a paper and prepared calculations and figures for it, and looked through also my dissertation draft.

...E. Schubert for the technical support during my doctoral work, for his valuable ideas, and for rapidly realizing urgently necessary constructions.

...Prof. K. Schwartz for his friendly help during the last years. I benefited a lot from the

numerous discussions with him. He aroused my interest in reading by providing me with various books and magazines. His advices helped me enormously during the doctoral work, and not only my scientific thinking was educated by him.

...Dr. C. Trautmann for the great help within the work of our group. She arranged most of the beam times and supported me during all of them with her practical help. She took a lot of time for fruitful discussions and helped me with the preparation of a paper. I gratefully acknowledge her intensive corrections of this thesis.

...Dr. M. Toulemonde for his hospitality in Caen, for discussions, and for the great dinner on the sea.

...Prof. G.A. Wagner for introducing me into the GSI Department of Materials Research in the year 2000. He was the project leader of a BMBF-grant, which supported me with equipment for the practical work and for traveling to interesting conferences. Furthermore, I acknowledge his corrections of the thesis manuscript and for the refereeing.

...all present and former members of the GSI Materials Research Department for the agreeable and friendly atmosphere, for their help concerning computers and for many, many discussions (Dr. C. Müller, Dr. sc. Z. Siwy, Dr. M. Heiß, Dipl.-Phys. K.-O. Voss, Dipl.-Phys. T. Cornelius, Dipl.-Phys. B. Schiedt, Dipl.-Phys. B. Zielbauer, Dr. A. El-Said, Dr. E. Toimil, Dipl.-Phys. D. Baur, Dr. B. Fischer, PD Dr. R. Spohr, Dr. J. Liu, Dr. N. Chtanko, Dr. M. Cholewa, Dr. I. Enculesco, Dr. C. Zet).

...all people from the "Schnitzel-Bank" for the diversion during my writing procedure and many nice discussions (Don, Harro, Pfrimel, Herbert, Adrian, Brigitte, Paul, Pio, and the rest)

last but not least, I would like to say thanks to my whole family and all of my friends!

THANK YOU ALL !!!